

MEASUREMENT AND COMPUTER SIMULATION OF THE  
FARFIELD PATTERNS FOR TURNING-MIRROR  
SURFACE-EMITTING DIODE LASERS

Vibhavari Apte  
B.Tech., Indian Institute of Technology, Bombay, India, 1986

A thesis submitted to the faculty  
of the Oregon Graduate Center  
in partial fulfillment of the  
requirements for the degree  
Master of Science  
in  
Electrical Engineering

August, 1988

The thesis "Measurement and Computer Simulation of the Farfield Patterns for Turning-Mirror Surface-Emitting Diode Lasers" by Vibhavari Apte has been examined and approved by the following Examination Committee:

---

Richard K. DeFreez, Thesis ~~Research~~ Advisor  
Senior Scientist  
Department of Applied Physics and Electrical Engineering  
Oregon Graduate Center

---

Richard A. Elliott  
Professor  
Department of Applied Physics and Electrical Engineering  
Oregon Graduate Center

---

V. S. Rao Gudimétra  
Assistant Professor  
Department of Applied Physics and Electrical Engineering  
Oregon Graduate Center

---

Jean F. Delord  
Professor  
Department of Physics  
Reed College

## ACKNOWLEDGMENTS

I am indebted to the following people for their contributions to this thesis. Foremost is my advisor, Dr. Richard K. DeFreez whose invaluable guidance and support helped me see this thesis to completion. I would also like to thank Dr. Richard A. Elliott for his helpful suggestions and financial support along the way. I am grateful to Joe Puretz and Geoff Crow for micromachining the turning mirrors, Jeff Irland for mounting the laser diodes, Geoff Wilson for numerous useful suggestions and Nu Yu for his help to write this thesis.

I am also thankful to Drs. V. S. Rao Gudimetla and Jean Delord for their participation on my thesis examination committee and their very careful examination of this thesis. I sincerely thank Dr. J. N. Walpole for some very useful suggestions and for the experimental data for the farfield patterns of surface-emitting diode lasers with parabolic turning mirrors.

Finally, I am most indebted to my parents and my husband for their love, support and encouragement.

To my parents and my husband for their love and encouragement.

## Table of Contents

ACKNOWLEDGEMENTS .....	iii
DEDICATION .....	iv
LIST OF FIGURES .....	viii
ABSTRACT .....	xi
1. INTRODUCTION .....	1
2. SEMICONDUCTOR LASERS .....	4
2.1 Criterion For Lasing .....	4
2.2 Quantum Well Heterostructure Lasers .....	7
2.3 Need For Multiple Stripe Lasers .....	10
3. SURFACE EMITTING LASER DIODES .....	14
3.1 Surface Emitting Geometries .....	14
3.1.1 Vertical Cavity .....	15
3.1.2 Horizontal Cavity .....	17
3.2 Monolithic two-dimensional arrays .....	21
4. COMPUTER SIMULATION OF FARFIELD PATTERN .....	23
4.1 Optical Waveguides .....	23
4.1.1 Waveguide Modes .....	26
4.1.2 Waveguide Equations .....	26

4.2	Waveguide Structures .....	28
4.2.1	Dielectric Slab Waveguide .....	28
4.2.2	Stripe Geometry Waveguide .....	31
4.3	Formulation of the problem .....	33
4.3.1	Waveguide Model For Computer Simulation .....	42
4.4	Theoretical Formulation .....	44
4.5	Farfield Pattern .....	47
5.	EXPERIMENT .....	53
5.1	Focused Ion Beam Micromachining .....	53
5.1.1	Micromachining System .....	54
5.1.2	Micromachining Procedure .....	56
5.2	Experimental Setup For Measuring Farfield Patterns .....	57
5.3	Specifications Of The Laser Diodes .....	62
6.	RESULTS .....	66
6.1	Results For A Surface-Emitter With A Parabolic Turning Mirror .....	69
6.2	Results For A Surface-Emitter With A 45° Turning Mirror .....	71
7.	CONCLUSIONS .....	79
	REFERENCES .....	81
	APPENDIX A .....	87

A1.1	Equations For Bound and Radiation Mode Fields .....	87
A1.2	Equations For Coefficients $R$ and $g(\gamma)$ .....	88
APPENDIX B	.....	92
B1.1	Simplifications for Evaluating Equation (4.28) .....	92
B2.2	Calculating The Farfield Pattern .....	93
APPENDIX C	.....	95
BIBLIOGRAPHICAL NOTE	.....	116

## List of Figures

2.1 Schematic of conventional laser versus quantum-well laser .....	8
2.2 Schematic of phase-locked laser array with evanescent wave coupling .....	12
3.1 Structure of a surface-emitting <i>GaAlAs/GaAs</i> injection laser with circular mirror. ....	16
3.2 Schematic view of surface-emitting <i>GaInAsP/InP</i> laser with parabolic turning mirror .....	18
3.3 Cross-section of the output coupling section of surface-emitting device with grating .....	20
4.1 Structure of conventional single emitter diode laser .....	24
4.2 Schematic cross section of a three-layer optical waveguide .....	29
4.3 Electric field distribution of various modes in a three-layer waveguide .....	32
4.4 Schematic of surface-emitting diode laser with 45° turning mirror .....	34
4.5a Theoretical farfield pattern using scalar diffraction theory and a Gaussian beam of spot size 2 $\mu m$ .....	35
4.5b Theoretical farfield pattern using scalar diffraction theory and a Gaussian beam of spot size 5 $\mu m$ .....	36

4.6a	Experimentally measured farfield pattern for a surface-emitter with a 45° turning mirror .....	38
4.6b	Experimentally measured pattern from an edge-emitter. ....	39
4.7a	Theoretical farfield pattern using integral equation of Helmholtz and Kirchoff and a Gaussian beam of spot size 0.2 $\mu m$ .....	40
4.7b	Theoretical farfield pattern using integral equation of Helmholtz and Kirchoff and a Gaussian beam of spot size 0.8 $\mu m$ .....	41
4.8	Schematic of waveguide model to calculate field at the plane $z = 0$ .....	43
4.9	Field amplitude at the waveguide-air interface calculated using equation 4.24 .....	48
4.10	Schematic of the laser diode used to calculate the farfield pattern from field at interface <i>AOC</i> .....	50
5.1	Schematic of optical column and control system .....	55
5.2	Schematic of radiation pattern of laser diode .....	58
5.3a	Schematic of the setup to measure the farfield pattern of a laser diode .....	60
5.3b	Schematic of the setup to transfer frame grabbed data to micro-vax .....	61
5.4a	SEM picture of parabolic turning mirror cross-section .....	64
5.4b	Parabolic turning mirror used to model farfield pattern .....	65
6.1a	Theoretical electric field pattern at the waveguide-air interface	

using Davies and Walpole's theory .....	67
6.1b Theoretical electric field pattern at waveguide-air interface illustrated in Davies and Walpole's paper. ....	68
6.2 Computer simulated farfield pattern from a surface-emitter with 45° turning mirror .....	70
6.3a Measured farfield pattern from surface emitter with parabolic turning mirror (wafer 685) (courtesy Dr. Walpole) .....	72
6.3b Measured farfield pattern from surface emitter with parabolic turning mirror (wafer 792) (courtesy Dr. Walpole) .....	73
6.4 Farfield pattern with a parabolic turning mirror excluding the contribution of light bypassing the mirror .....	74
6.5 Computer simulated farfield pattern for a surface-emitter with a 45° turning mirror .....	75
6.6a Measured farfield pattern for a surface-emitter with a 45° turning mirror (SEPADL-20) .....	76
6.6b Measured farfield pattern for a surface-emitter with a 45° turning mirror (SEPADL-22) .....	77

ABSTRACT

MEASUREMENT AND COMPUTER SIMULATION OF THE  
FARFIELD PATTERNS FOR TURNING-MIRROR  
SURFACE-EMITTING DIODE LASERS

Vibhavari Apte, M.S  
Oregon Graduate Center, 1988

Supervising Professor: Dr. Richard K. DeFreez

Surface-emitting laser diodes are of interest for various applications such as monolithic two-dimensional arrays and optical interconnects for integrated optics. Therefore, it is essential to characterize these lasers. The farfield radiation pattern is one of the important characteristics of a laser diode. In this thesis the farfield of a surface-emitting laser diode with a turning mirror is modeled and measured. The computer simulation uses a rigorous theoretical expression for the field at the output mirror laser-air interface derived by Davies and Walpole and then using a modified form of the Kirchoff diffraction integral to generate the farfield. The computer modeling is done for both flat  $45^\circ$  and parabolic turning mirrors. Experimental data were also obtained for a surface-emitter with a  $45^\circ$  straight turning mirror. This mirror was fabricated using the focussed ion beam micromachining technique developed at OGC. In the case of the parabolic turning mirror, the experimental results published by Liau and Walpole were used. A comparison of theoretical and experimental results for the two shapes of mirrors is also presented.

## 1. INTRODUCTION

A considerable amount of effort is being directed towards the development of semiconductor diode laser arrays for applications having power requirements that exceed the output power level attainable with individual devices. For example, a monolithic linear array emitting total output power of 38W cw with total power conversion efficiency of 30% has recently been reported<sup>1</sup>. But, there is also a need for two-dimensional arrays to meet the power and area requirements for such applications as the pumping of large solid-state lasers. Two-dimensional arrays can be fabricated by stacking and joining separate linear arrays of edge-emitting diode lasers. Recently a 2-D array formed using this technique was reported to produce 175W at 26A, ie. a power density of  $2.1Kw/cm^2$ .<sup>2</sup> Several types of surface-emitting *GaAs/GaAlAs* and *GaInAsP/InP* diode lasers have also been reported that could be used for this purpose. These include lasers with the resonant cavity normal to the wafer surface<sup>3</sup> and others for which emission normal to the surface is achieved by second order gratings<sup>4,5</sup> or are etched by using ion beam assisted etching<sup>6</sup> or by turning mirrors which are chemically etched<sup>7</sup> or are focussed ion beam micromachined<sup>8,9</sup>.

The work done in this thesis to model and experimentally verify the farfield pattern of a surface-emitting diode laser using a turning mirror was prompted in part by a comment by Walpole<sup>10</sup> that simple diffraction theory with a Gaussian beam approximation is not appropriate to model the farfield

pattern of a surface-emitting diode laser with a turning mirror. Hence, the major part of the work presented here deals with computer simulation of the farfield by solving for the field at the waveguide-air boundary using the theory developed by Davies and Walpole<sup>11</sup>. This field was then used to calculate the farfield of a surface-emitting diode laser with a turning mirror. The work was also supported by experimental data from a surface-emitter with a 45 degree turning mirror which was focussed ion beam micromachined at OGC. An attempt was also made to duplicate the results presented by Liao and Walpole<sup>7</sup> for a parabolic turning mirror.

This thesis is organized as follows. Chapter 2 presents an overview of semiconductor lasers. It starts with section 2.1 which outlines the lasing criterion for a laser in general, continues with section 2.2 describing a quantum well heterostructure laser and ends with section 2.3 which presents the need for multiple stripe lasers and phase-locked laser arrays.

A detailed description of surface-emitting laser diodes is the subject matter of chapter 3. Section 3.1 presents the details of different surface-emitting geometries and section 3.2 concerns monolithic two-dimensional arrays of surface-emitting diode lasers.

Chapter 4 gives a complete outline of the theoretical formulation of the problem of calculating the electric field intensity at the waveguide-air interface and using this field to calculate the farfield patterns for turning-mirror surface-emitting diode lasers. Section 4.1 gives a general description of the theory of optical waveguides. Section 4.2 describes the dielectric slab and stripe geometry waveguide structures. Formulation of the problem of calculating the farfield

pattern is given in section 4.3. It starts by illustrating the results of the simulation of farfield patterns from two different approaches tried at the beginning. Next, it describes the waveguide model which was finally used to solve the boundary value problem at the waveguide-air interface. Section 4.4 presents the theory as given by Davies and Walpole<sup>11</sup>. Section 4.5 describes the method of calculating the farfield pattern from the field at the waveguide termination. The details of theoretical formulation and computer code are presented in Appendices 1, 2 and 3.

Chapter 5 presents the experimental part of this work. Section 5.1 explains the focussed ion beam micromachining technique used to machine the 45 degree turning mirror. Section 5.2 is a short description of the experimental setup employed to measure the farfield pattern. The last section, section 5.3, gives the specifications of the laser diodes used for modeling the farfield patterns.

Chapter 6 presents the results obtained from experiment and computer simulation and also presents a comparison of the two.

Conclusions are presented in chapter 7.

## 2. SEMICONDUCTOR LASERS

In a semiconductor one can obtain stimulated emission by minority carrier injection using a p-n junction. When the forward bias on a p-n junction is sufficiently large to allow the propagation of electrons throughout the conduction band beyond the barrier at the p-n junction (or holes throughout the valence band), the current assumes the injection mode. In the injection mode, direct band to band photo-recombination becomes possible in a direct-gap semiconductor. The injection current and the corresponding emission increases rapidly with bias voltage, and can result in lasing action. This chapter discusses the principle of operation of laser diodes in general, presents a short discussion of quantum well heterostructure lasers, and briefly describes phase-locked laser arrays.

### 2.1 Criterion For Lasing

A photon with energy  $h\nu$  traversing a semiconductor can stimulate a transition between two levels  $E_1$  and  $E_2$  whose energy difference is  $E_1 - E_2 = h\nu$ . There can also be spontaneous transition. A stimulated recombination generates a photon which has the same frequency, direction of propagation, and phase as the stimulating photon. A spontaneous recombination generates photons propagating in random directions and random phases. Sufficient carrier population

inversion assures that stimulated emission exceeds spontaneous emission.

In order to use the stimulated recombination process in a laser, two conditions must be met

- (1) the gain is equal to the losses,
- (2) and the radiation is coherent.

Coherence can be achieved by placing the source of radiation in a cavity which will favor the amplification at a cavity oscillation frequency. This selective amplification is the result of positive feedback for those electromagnetic waves which form a standing pattern in the cavity. Now, if one considers a point in the center of this cavity emitting an intensity  $L_0$  towards one of the walls, then when the gain equals the sum of all losses, the intensity of radiation at the center of the cavity remains unchanged after traveling a distance of  $2l$ , where  $l$  is the cavity length. This condition is given by the equation<sup>12</sup>

$$gl - \alpha l - \frac{1}{2} \ln \left\{ \frac{1}{R_1 R_2} \right\} = 0 \quad (2.1)$$

where

$g$  = gain per unit length

$\alpha$  = distributed losses per unit length

$R_1, R_2$  = Reflectances of cavity mirrors

$l$  = length of laser cavity

The gain is given by the following expression<sup>12</sup>

$$g = c^2 j \frac{\eta}{8\pi q n^2 \nu^2 \Delta \nu d} \quad (2.2)$$

$j$  = current density

$\eta$  = radiative recombination efficiency

$n$  = index of refraction

$\nu$  = frequency of photons emitted in spontaneous spectral halfwidth  $\Delta\nu$

$d$  = thickness of the active region

$c$  = speed of light in vacuum

$q$  = electron charge

The threshold current for the laser can be derived if one writes  $g = \beta j$ , where  $\beta$  is called the gain factor.  $\beta$  is directly dependent on the temperature. Making this substitution in equation 2.2 one has,

$$\beta j_{th} = \alpha + \frac{1}{2l} \ln \frac{1}{R_1 R_2}. \quad (2.3)$$

where  $j_{th}$  is the threshold current density. Now, by writing  $R_1 R_2 = R^2$  one has the following relation for current density.

$$j_{th} = \frac{\alpha}{\beta} + \frac{1}{\beta l} \ln \frac{1}{R} \quad (2.4)$$

The losses, the threshold current and efficiency all are temperature dependent. The temperature dependence around room temperature of the threshold current, is approximately given by<sup>12</sup>,

$$J_{th} = J_0 \exp \left( \frac{T}{T_0} \right) \quad (2.5)$$

where  $T_0 \geq 120K$  near room temperatures for *AlGaAs* lasers. The external efficiency below threshold also has exponential temperature dependence due to the exponential temperature dependence of absorption losses.

## 2.2 Quantum Well Heterostructure Lasers

When the n-type and p-type regions on either side of the junction consist of a different semiconductor from that of the active region, the transition is called a heterojunction. One purpose of resorting to heterojunctions is to obtain high injection efficiency of minority carriers into the lower band-gap semiconductor which forms the active region. The addition of one or more heterojunctions to laser diodes has resulted in major improvements in their performance, flexibility and emission wavelength range. In particular threshold current densities have been reduced by an order of magnitude.

When the thickness  $L_z$  of a semiconductor layer, for example, the active layer of a double heterostructure (DH) laser, is reduced to the order of carrier de Broglie wavelength ( $\lambda = \frac{h}{p} \sim L_z$ ), effects not typical of bulk material known as quantum size effects occur. Size quantization results in a series of discrete energy levels given by the bound state energies of a finite square well. Electrons or holes in the active layer are then restricted to this finite potential well. Figure 2.1 shows a schematic diagram of conventional versus quantum well laser. The band diagram in this figure shows clearly that the active layer thickness in the quantum well laser is about ten times smaller than in a conventional laser. The narrow restricted active region causes one dimensional behaviour of electrons and holes normal to the layer and two-dimensional behaviour in the plane of the layers, instead of the usual three degrees of freedom. A detailed discussion of quantum well lasers can be found in the paper by Holonyak<sup>13</sup> and a book edited by R. Dingle<sup>14</sup>.

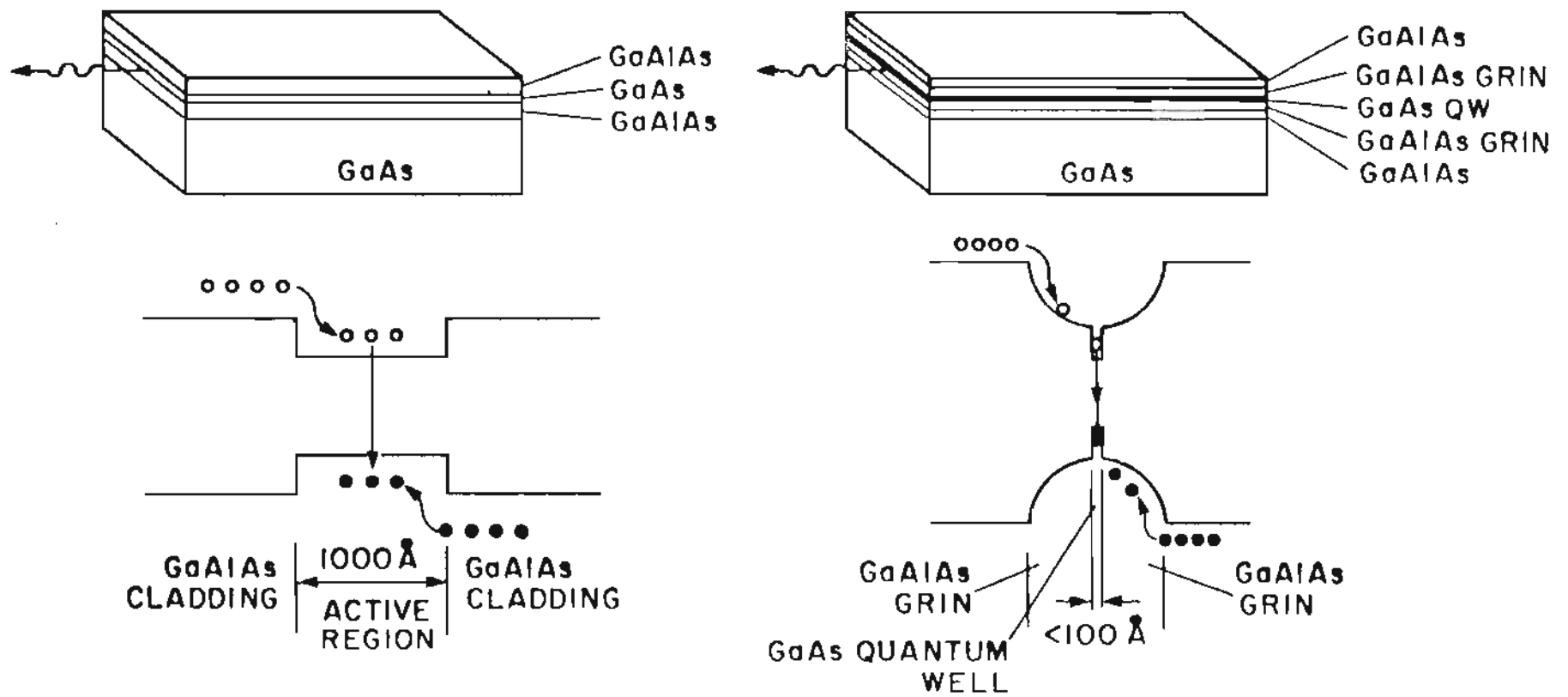


Figure 2.1 Schematic of conventional lasers versus quantum-well lasers

The conduction band density-of-states function in a conventional double heterostructure laser is parabolic and is expressed as<sup>14</sup>,

$$\rho_c = \frac{\left(2m_e^*/\hbar^2\right)^{\frac{3}{2}} E^{\frac{1}{2}}}{4\pi^2} \quad (2.6)$$

where

$m_e^*$  = electron effective mass

$E$  = energy measured from conduction band edge  $E_c$

$\hbar$  = Planck's constant/ $2\pi$

$\rho_c$  = parabolic density-of-state function in three dimensions

But for a two dimensional quantum well heterostructure laser, then density-of-state function is a step function given by<sup>14</sup>,

$$\rho_c = \sum_n \frac{m_e^*}{\pi \hbar^2 L_z} H(E - E_{nz}^e) \quad (2.7)$$

where  $H(E)$  is a unit step function with  $H(E \geq E_{nz}^e) = 1$  and  $H(E \leq E_{nz}^e) = 0$ .  $E_{nz}^e$  denotes the quantized energy levels with quantum number  $n$ . Devices which have a single low bandgap active layer are known as single quantum well lasers, and those with the active layer consisting of many alternating layers of low and high bandgap materials forming a superlattice type structure are called multiple quantum well lasers<sup>15</sup>. The two dimensional nature of electron motion in quantum well heterostructures produces several unique and important features in semiconductor lasers. In the *GaAs/AlGaAs* material system, the most important improvements which have been demonstrated are<sup>16</sup>

- 1) reduction of laser threshold current density ( $J_{th} = 250-400 A/cm^2$ ),
- 2) a less pronounced temperature sensitivity of the laser threshold current

density( $T_0 \geq 250$ ),

3) a higher relaxation oscillation frequency due to higher differential gain  $\delta g / \delta n(E)$ , where  $g$  is the gain and  $n(E)$  is electron density, and

4) a higher polarization stability due to the large difference of optical gain for TE and TM modes.

### 2.3 Need For Multiple Stripe Lasers

The heterolayers in semiconductor lasers confine light and injected carriers in the direction perpendicular to the plane of the structure due to the refractive index step between center and cladding layers and due to potential barriers created on either sides of the active region. Whenever there is carrier confinement in the plane of the junction, such a laser is called as a stripe laser. Several types of stripe lasers are obtained depending upon the type of optical confinement employed. For example, a buried heterostructure stripe laser is obtained when a filament of narrow bandgap material is entirely embedded in a wider bandgap material. In a rib stripe laser, optical confinement is obtained by locally stepping up the thickness of the active layer.

Semiconductor lasers with wide stripe or broad-area contacts are capable of generating high-power optical pulses by virtue of their large emitting area. However, in contrast to narrow-stripe fundamental transverse mode lasers, wide-stripe lasers either operate in one or more higher order lateral modes or in several relatively independent filaments due to self-focusing of filament. In the former case, the beam divergence in the plane of p-n junction is substantially

greater than that theoretically available from a wide emitter, whereas the light emitted in the latter situation exhibits little or no spatial coherence. Hence, the farfield radiation pattern is generally broad and may fluctuate with time or drive current. One approach to overcoming this disadvantageous attribute (thereby obtaining a high-power low-divergence beam) is to operate a multiple-stripe laser in a phase locked state<sup>17,18</sup>.

High-power monolithic laser arrays which emit up to 38 W CW with a total power conversion efficiency of up to 30% have been reported<sup>1</sup>. Recent examples of gain-guided phase-locked arrays include coupled multiple stripe quantum well laser arrays<sup>19</sup>, offset stripe laser arrays<sup>20</sup> and chirped arrays<sup>21</sup>. Index guided laser arrays have also been fabricated and CW and pulsed operations to high powers have been achieved<sup>22-24</sup>. Gaussian shaped picosecond pulses as short as 62ps have been observed for an array of 10 phase-coupled multiple quantum well GaAs lasers<sup>25</sup>. Also, high-power high-efficiency 2-D laser arrays emitting 175 W at 26A have been recently reported<sup>2</sup>.

Figure 2.2 <sup>26</sup> shows the schematic diagram of a representative gain-guided phase-locked laser array. The device consists of conventional double-heterostructure layers with conducting stripe contacts on the p-side. The metallization is Au/Cr and the proton implant serves to destroy the conductivity of unmasked areas. The optical coupling of adjacent stripes in such a laser array is provided by the penetration of the optical field of one laser stripe into the active region of the other. Locked oscillation, ie. simultaneous coherent operation of adjacent lasers at the same optical frequency occurs as a result of the stimulated emission induced by either field in the other cavity and the

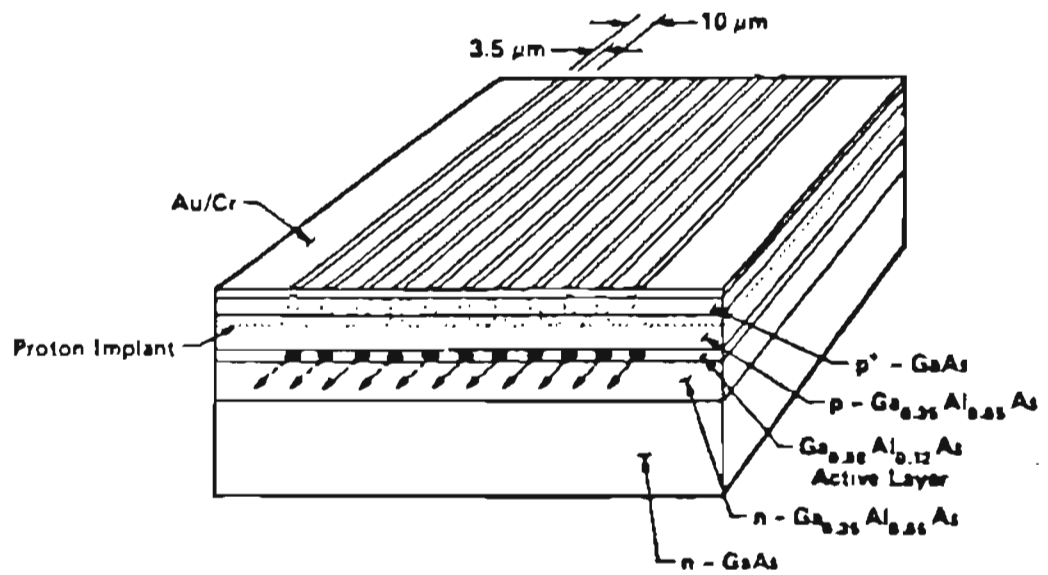


Figure 2.2 Schematic of phase-locked laser array with evanescent wave coupling. [26]

mutual interaction of fields in the region between the cavities<sup>27</sup>. Coupled mode analysis of phase-locked injection laser arrays has been developed by J. K. Butler et al<sup>28</sup> and Kapon et al<sup>29</sup>. Using coupled mode analysis one can solve for allowed modes and splitting of oscillation frequencies of the individual emitters that result from interaction between the emitters. This thorough analysis gives farfield lobe widths which match the experimentally observed farfield lobe widths better than those obtained by using simple diffraction theory which provides no method for describing the allowed oscillating modes of arrays of coupled emitters.

Traditionally, diode lasers have been edge emitters with cleaved facets for oscillation mirrors. Although these are capable of giving very high output powers, surface-emitting devices for optoelectronic integrated circuits have been of much interest lately. Phase-locked laser arrays can be made to emit light from the top surface rather than the sides. These are called the surface emitting diode lasers and will be discussed in the next chapter.

### 3. SURFACE EMITTING LASER DIODES

Surface-emitting (SE) semiconductor diode lasers emit radiation perpendicular to the surface of the wafer on which they are fabricated. This characteristic is very attractive since first, such devices are necessary building blocks for monolithic two-dimensional arrays of diode lasers and second, they are also of interest as transmitters in optical interconnections between electronic integrated circuits. Conventional diode lasers emit into the plane of the wafer, which must be cleaved so that the emitting edge is exposed. Surface emitters can be fabricated and operated without cleaving or dicing the wafer. This may prove useful in the manufacture and on-wafer testing of diode lasers. Some surface emitters provide laser output over areas which are large compared to their optical wavelength, resulting in beam divergence that is considerably less than that of conventional diode lasers. Narrow beams are highly desirable in most applications and particularly in optical fiber systems, where laser to fiber coupling can be significantly enhanced.

#### 3.1 Surface Emitting Geometries

There are two basic configurations of optical cavity used for surface emitters. In one configuration, the optical cavity is formed by mirrors, for example at the top and bottom surfaces of the wafer and may have distributed

feedback (DFB) or distributed Bragg reflector (DBR) sections<sup>30</sup>. These are called the vertical cavity lasers. In the other configuration, the horizontal cavity, the axis of optical cavity lies in the plane of the active layer.

### 3.1.1 Vertical Cavity

A model of an SE laser with a vertical cavity is shown in Figure 3.1<sup>31</sup>. The mirror on the n-side was formed by first etching off the Au/Sn metal and then the *GaAs* substrate and *GaAs* buffer layer. The etching was stopped by the etch stop layer of n-*Ga<sub>0.5</sub>Al<sub>0.5</sub>As*. The mirror on the p-side was formed by sputtering the *SiO<sub>2</sub>* to open circular windows of 20  $\mu\text{m}$  diameter. Hence a vertical cavity is formed between these two mirrors and surface emission is obtained as shown in the figure. The electrodes are annular rings so that they do not interfere with the mirrors. The cavity length has to be compromised by taking into account threshold current density and mode spacing. Since the cavity length is small, gain is low and hence losses have to be kept low (Refer to Equation 2.1). Hence mirrors are fabricated with reflectivity greater than 95 percent. A slightly different configuration called the ring electrode laser is obtained when p-electrode is formed in a ring shape instead of a circular shape<sup>32</sup>. The ring electrode is introduced in order to increase reflectivity.

It is possible to obtain very low thresholds in these lasers. CW operation at 77K and a low threshold current of 6mA has been obtained from a surface-emitting circular buried heterostructure laser<sup>33</sup>.

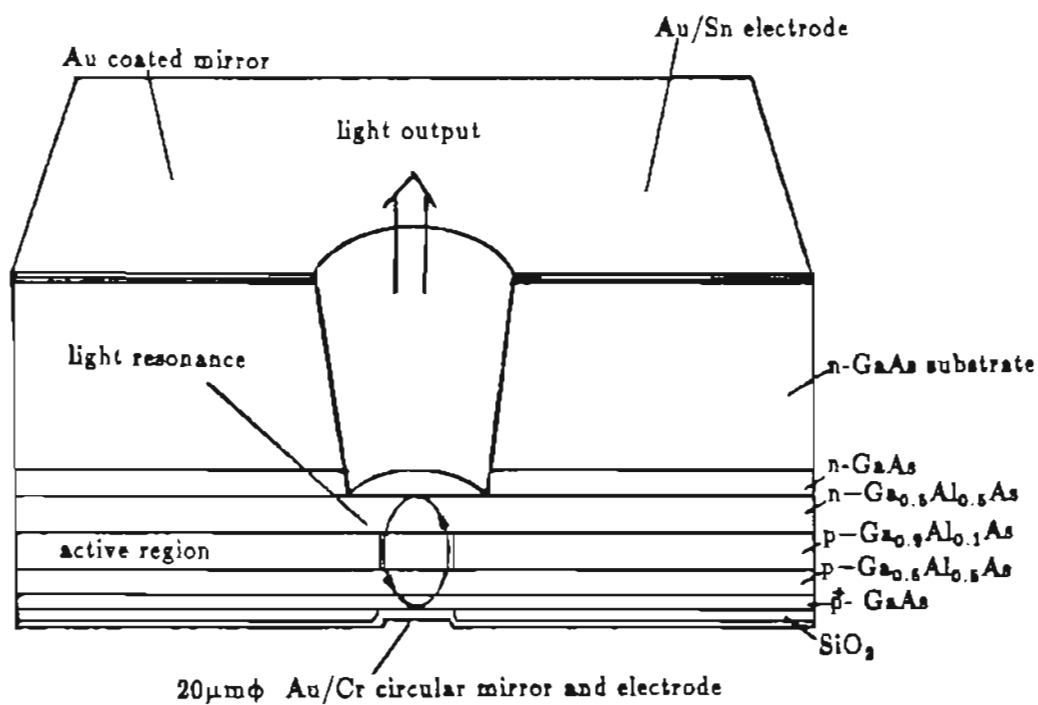


Figure 3.1 Structure of a surface-emitting GaAlAs/GaAs injection laser with circular mirror.[31]

### 3.1.2 Horizontal Cavity

A horizontal cavity is standard for laser diodes. In this configuration high gain can be achieved since gain lengths of 100 to 400 $\mu m$  are typical. Surface emission is obtained by deflecting a part of light in the direction perpendicular to the axis of the cavity. This deflection can be achieved using beam deflectors at the end of the device or by using a grating of appropriate design.

**Beam Deflectors:** Here the laser cavity has the same geometry as an edge emitter except for a monolithically integrated beam deflector. Several versions of this type of device have been reported in both *GaInAsP* and *AlGaAs* double heterostructure systems.

Chemical etching with subsequent mass transport has been used to fabricate *GaInAsP/InP* surface-emitting lasers<sup>7</sup>. These devices were operated at a threshold current as low as 12mA, differential quantum efficiency as high as 47% and farfield pattern with a main lobe as narrow as 12°. Figure 3.2 shows schematic of this structure. First, a mesa was formed as seen on the right. Then selective chemical etching procedure was used to produce a stair-structure on one side and nearly vertical wall on the other. Next, the wafer was loaded in a furnace for mass transport in order to form a parabolic mirror as seen in the figure. The farfield pattern from this surface-emitting laser has been computer simulated and is shown in Chapter 5.

Ion milling has been used to fabricate dry etched mirrors on *GaAlAs/GaAs* laser and has demonstrated low threshold and high efficiency. Output power of up to 15mW was observed<sup>34</sup>.

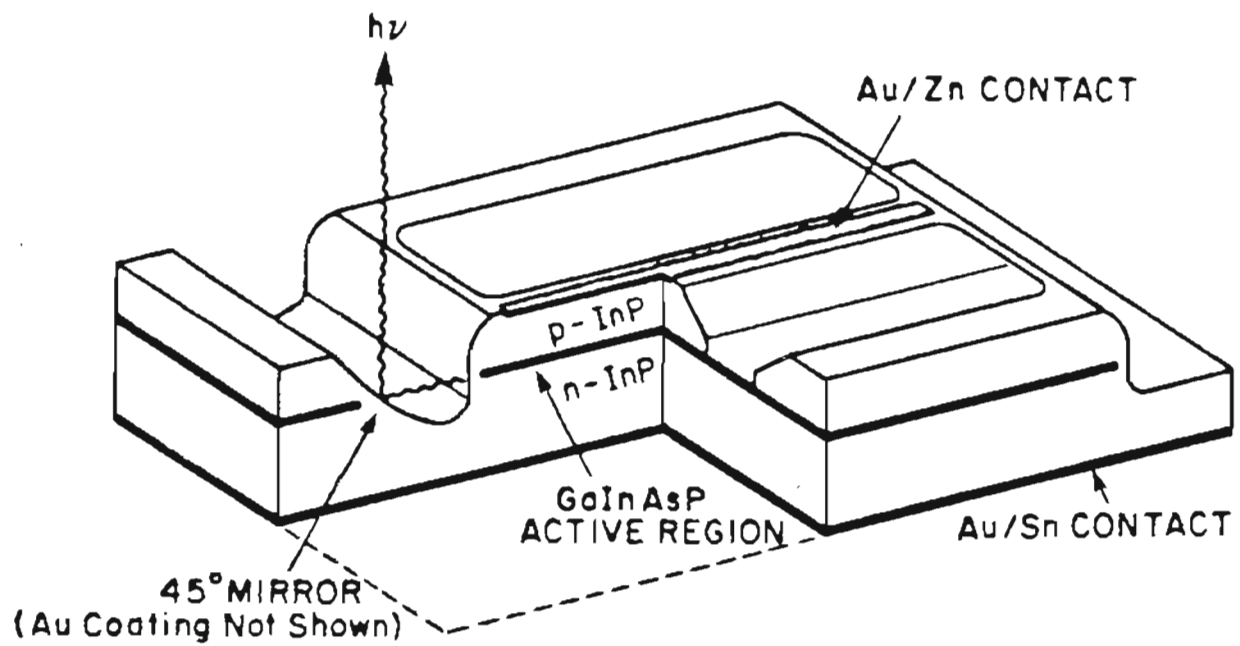


Figure 3.2 Schematic cut-away view of a surface-emitter GaInAsP/InP laser with 45° turning mirror made by chemical etching followed by mass transport.[7]

By using ion beam assisted etching, light emission normal to the surface of a *GaAs/AlGaAs* wafer has also been obtained by fabricating edge-emitting double-heterostructure diode laser with a monolithic 45° deflector adjacent to one of the laser facets<sup>6</sup>.

Focussed ion beam micromachining techniques have been used to fabricate a 45° turning mirror to form a surface emitting, ten element, phase-locked array giving 330mW optical power under pulsed operation<sup>8,9</sup>. Another technique called reactive ion beam etching was recently used to obtain surface-emitting multiquantum well lasers with optical bistability<sup>35</sup>.

**Grating:** A schematic cross section of the output coupling section of grating-coupled, surface-emitting device is shown in Figure 3.3. <sup>36</sup> Electrodes (not shown) are formed on the top and bottom surface. In addition to the active layer, another layer named as the 'second layer' is shown in which, the grating is ruled with the periodicity of the optical wavelength in the laser. In general, the grating couples light into both the vertical directions (up and down) by first order diffraction. It will also couple light to the left and right of the figure by second order diffraction. This coupling is used for feedback, either as a distributed feedback (DFB) laser<sup>37,38</sup> as shown in Figure 3.3, or as a distributed bragg reflector (DBR) laser where feedback is obtained by bragg reflector sections on the right and left ends<sup>39</sup>. For efficient operation the design should provide a means for eliminating one of the vertical outputs. A coherent surface-emitting diode laser array consisting of distributed Bragg reflector sections with farfield pattern as narrow as 0.012° emitting 250 mW has been reported<sup>4</sup>.

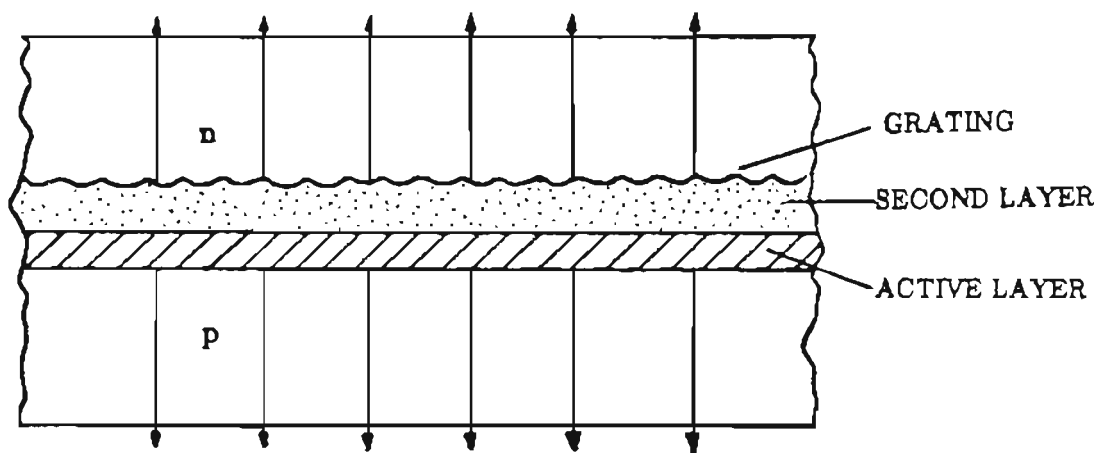


Figure 3.3 Cross-section of the output coupling section of surface-emitting device with grating. [36]

### 3.2 Monolithic two-dimensional arrays

Semiconductor lasers have very large overall efficiencies (optical output power/electric pumping power). Devices fabricated with single quantum well active regions have exhibited total power conversion efficiencies greater than 50%<sup>40,41</sup>. Hence, arrays of lasers offer the possibility of high efficiency and large total power. Linear one-dimensional diode laser arrays are being developed for efficient, high power sources of pump radiation for solid state lasers. A coherent combination of the outputs of the elements of the array can be used directly as a high power high efficiency bright laser. Surface-emitters make possible the extension of these applications to two-dimensional arrays. A 16 laser two-dimensional array which has a low threshold of about 11-14 mA per element and high cw power of 270 mW at room temperature has been reported<sup>42,43</sup>.

The fabrication of gratings, mirrors, beam deflectors, and other such optical components with micrometer and submicrometer dimensions and smoothness and flatness less than a wavelength is difficult. The registering of patterns and the machining of structures require high technology. Advanced lithography, reactive ion etching, ion beam assisted etching, and focussed ion beam micromachining are some technologies used to make surface-emitters. Wet chemical etching followed by the mass-transport process for smoothing surfaces has been used to fabricate GaInAsP system lasers successfully. But unfortunately this process cannot be adapted easily for shorter wavelength lasers because of the reactivity of Al compounds.<sup>36</sup> Hence, research is being done to

find a technology to make good deflector mirrors for *GaAs/GaAlAs* systems. The surface-emitting laser with a  $45^\circ$  deflector mirror in a *GaAs/GaAlAs* system which was used for the experimental work for this thesis, was fabricated using focussed ion beam micromachining at the Oregon Graduate Center.

Before using a device in any application, it is necessary to know its characteristics. One of the most important characteristics of a laser diode is its farfield pattern. The next chapter describes the theory and computer simulation technique used to model the farfield pattern of a surface-emitting laser diode with a turning or deflector mirror.

#### 4. COMPUTER SIMULATION OF FARFIELD PATTERN

Within the past few years *GaAs/GaAlAs* injection lasers have developed to a point where they may be considered for many applications. For this reason, but also because a full understanding of these devices is not yet available, both manufacturers and users of lasers must have the capability of systematically and accurately characterizing the laser output radiation. Among the important measurements are: output power versus pumping current, near-field and far-field radiation patterns, and the laser oscillation spectrum. The combination of near-field and far-field radiation patterns together with the models of internal device behavior enables one to calculate modal phase dependence at the facet and thereby improve the design of external optical systems<sup>44</sup>.

The computer simulation of the far-field pattern of a surface-emitting diode laser with a turning mirror, is the major topic of this research. This chapter starts with theory of optical waveguides and then describes in detail the formulation and solution of the problem of evaluating the farfield pattern for such a surface-emitter.

##### 4.1 Optical Waveguides

A common laser structure is shown in Figure 4.1. The figure shows the layers of a conventional stripe laser. The stripe width is denoted by  $s$  and

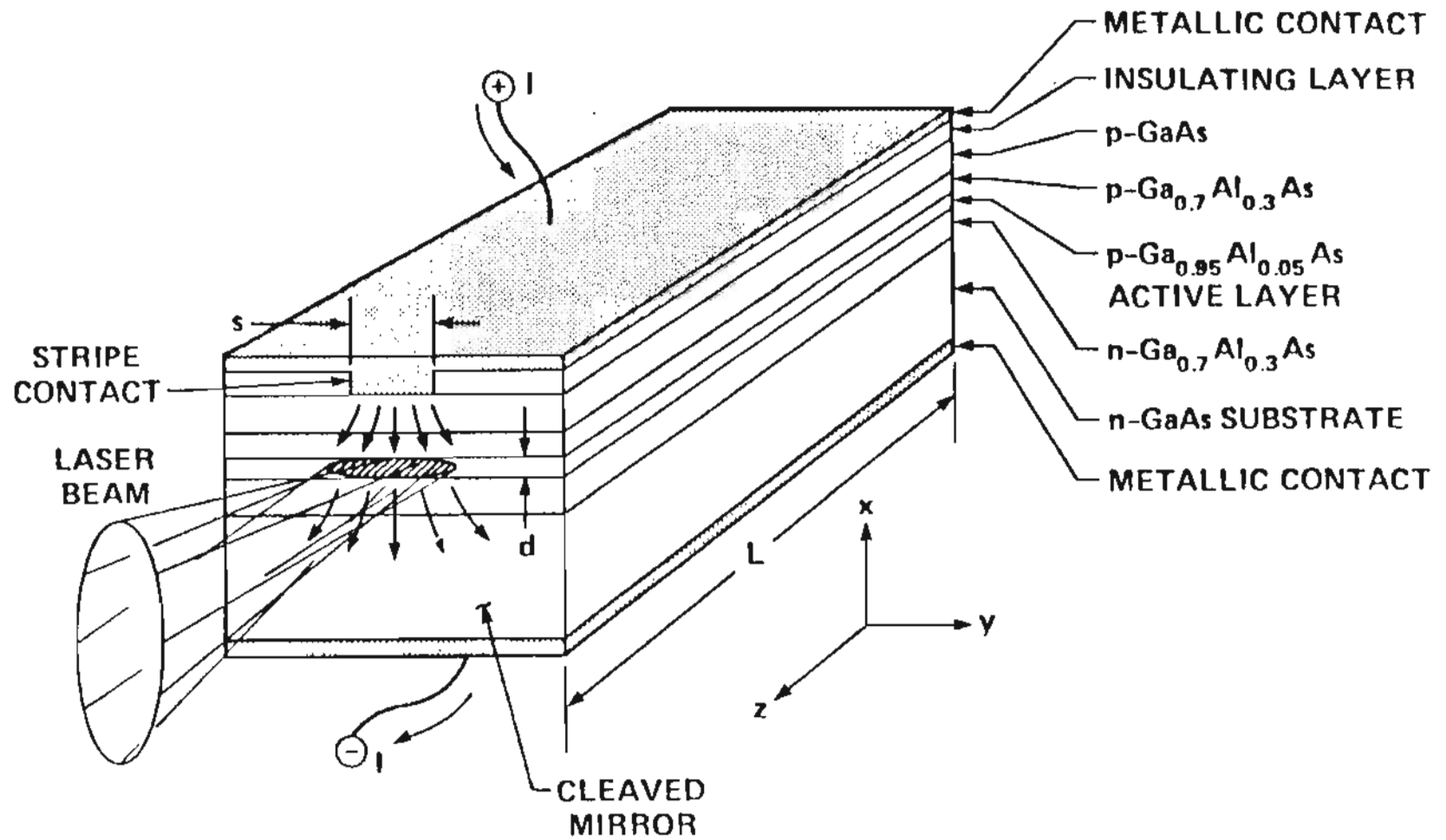


Figure 4.1 Structure of a conventional single emitter diode laser.

usually supports only one mode. The thickness of the active region is  $d$ . The arrows on the front facet indicates the current direction and the laser beam spot shows the spread of the laser beam in the parallel and perpendicular direction to the junction plane. In general a Fabry-Perot resonator is formed by cleaving two parallel facets which produces a resonant condition for optical lasing along the cavity axis. A highly reflecting film is commonly placed on one facet to improve the useful output at the opposite one. In the vertical direction, a diode laser requires an active region in which an electron-hole pair recombination generates the optical flux and a mode confinement region which overlaps the active region. Generally the mode confinement region extends beyond the active volume. The optical confinement is controlled by steps or gradients in refractive index. The extent of the recombination region is limited either by the minority carrier diffusion length or a potential barrier to the minority carriers. In heterostructure lasers the potential barrier at the interface is several  $kT$  high, and leads to good electrical confinement.

In the horizontal direction, waves propagating at large angles to the optic axis must be suppressed by introduction of high losses or index steps. For broad area contacts, sawing the side-walls or introducing lossy regions between broad stripe and side-walls achieves this. In some stripe contact diode lasers, a filament of narrow bandgap material is entirely embedded in wider bandgap material. This filament produces both a strongly guiding dielectric waveguide and also a region in which injected carriers are confined by potential barriers on all four sides. These are called buried heterostructure lasers. There are several other types of stripe lasers namely, p-n confinement stripe laser, rib stripe laser,

double stripe laser etc<sup>45</sup>.

#### 4.1.1 Waveguide Modes

The cavity modes of a injection laser can be approximated by two independent sets of TE (transverse electric) and TM (transverse magnetic) modes. The modes of each set can be further classified into,

- a.) longitudinal modes (axial modes) which determine the principal structure in the frequency spectrum and are related to cavity length L, its index of refraction and its dispersion as seen by the propagating wave,
- b.) lateral modes (in the plane of the junction) which give the lateral profile of the laser beam and are dependent on preparation of sidewalls and the diode width and index-step if any,
- c.) transverse modes (perpendicular to junction plane) which depend on the dielectric variation perpendicular to the junction.

#### 4.1.2 Waveguide Equations

The electromagnetic fields in a waveguide have the following functional dependence<sup>46</sup>

$$e = E(x,y)exp(i\omega t - \gamma z) \tag{4.1}$$

$$h = H(x,y)exp(i\omega t - \gamma z) \tag{4.2}$$

where  $\gamma = \alpha/2 + i\beta$  is the complex propagation constant. For purely propagating waves  $\alpha = 0$ , and for purely attenuating waves  $\beta = 0$ . The value of the propagation constant  $\gamma$  can be determined only after the geometry of the

waveguide structure is specified.

The above two equations when substituted in Maxwell's curl equations give rise to a set of equations

$$\partial E_z / \partial y + \gamma E_y = -i\omega\mu H_x \quad (4.3a)$$

$$-\gamma E_x - \partial E_z / \partial x = -i\omega\mu H_y \quad (4.3b)$$

$$\partial E_y / \partial x - \partial E_z / \partial y = -i\omega\mu H_z \quad (4.3c)$$

and

$$\partial H_x / \partial y + \gamma H_y = i\omega\epsilon E_x \quad (4.4a)$$

$$-\gamma H_x - \partial H_z / \partial x = i\omega\epsilon E_y \quad (4.4b)$$

$$\partial H_y / \partial x - \partial H_z / \partial y = i\omega\epsilon H_z \quad (4.4c)$$

These can be solved to give  $E_x$ ,  $E_y$ ,  $H_x$ , and  $H_y$  in terms of  $E_z$  and  $H_z$ . The four equations are as follows<sup>46</sup>

$$E_x = -(\gamma^2 + k^2)^{-1} \left[ \gamma \frac{\partial E_z}{\partial x} + i\omega\mu \frac{\partial H_z}{\partial y} \right] \quad (4.5a)$$

$$E_y = (\gamma^2 + k^2)^{-1} \left[ -\gamma \frac{\partial E_z}{\partial y} + i\omega\mu \frac{\partial H_z}{\partial x} \right] \quad (4.5b)$$

$$H_x = (\gamma^2 + k^2)^{-1} \left[ i\omega\epsilon \frac{\partial E_z}{\partial y} - \gamma \frac{\partial H_z}{\partial x} \right] \quad (4.5c)$$

$$H_y = -(\gamma^2 + k^2)^{-1} \left[ i\omega\epsilon \frac{\partial E_z}{\partial x} + \gamma \frac{\partial H_z}{\partial y} \right] \quad (4.5d)$$

All the components of the field obey the wave equation<sup>46</sup>

$$\nabla_{xy}^2 (E/H) + (k^2 + \gamma^2)(E/H) = 0 \quad (4.6a)$$

where

$$\nabla^2 = \nabla_{xy}^2 + \gamma^2. \quad (4.6b)$$

## 4.2 Waveguide Structures

Two forms of optical waveguide must be considered in the treatment of gain-guided heterostructure lasers. The first is the dielectric slab waveguide that is formed by three layers of dielectric material with the central layer having the largest index of refraction. The electromagnetic field is confined predominantly by total internal reflection in this region and the field escaping the high refractive index region dies down exponentially in the surrounding region. The second optical waveguide which is perpendicular to the first is in the plane of the layers and is the guide formed by surrounding a region of optical gain with a region of optical loss. This produces the 'gain-guiding' condition which is an important means of confining light in the junction plane of stripe lasers. The optical behavior in such a guide can be analysed by an extension of the treatment used for a dielectric waveguide, in which complex rather than real values of refractive index are used<sup>45</sup>.

### 4.2.1 Dielectric Slab Waveguide

Figure 4.2 <sup>46</sup> shows a three layer slab waveguide. The three layer slab waveguide is formed by three layers of dielectric with the center layer having the largest index of refraction. The types of modes associated with slab waveguides are

i) trapped or bound modes whose field energy is located in the neighbourhood of

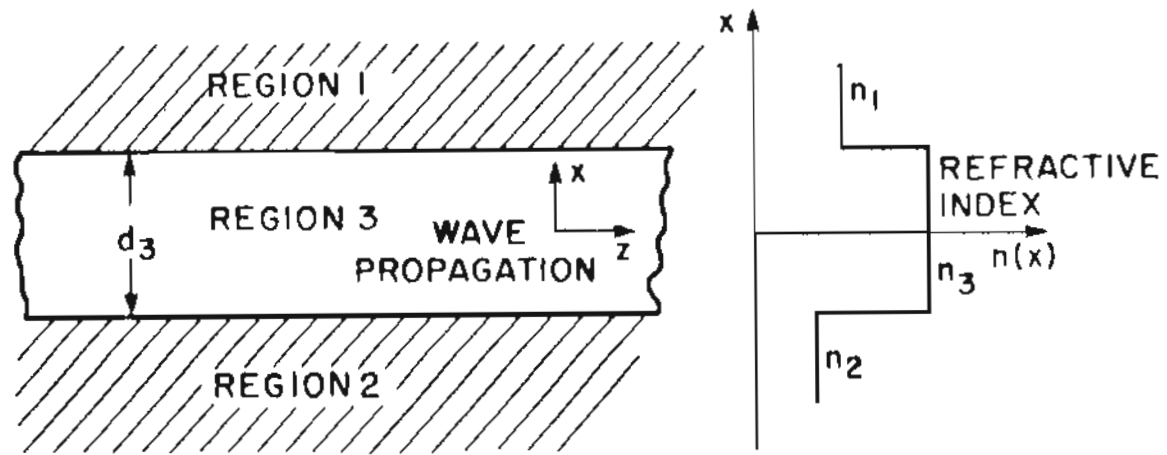


Figure 4.2 Schematic cross section of a three-layer optical waveguide. (a) The wave propagation along  $z$  direction, and (b) the refractive index as a function of  $x$  coordinate. [46]

the waveguide or center slab,

ii) radiation modes whose field intensity does not vanish at large distances from the slab.

The waveguide modes can be determined by using Maxwell's equations discussed in section 4.1.2. For fundamental mode propagation through an ordinary DH injection laser the TE mode has lower mirror losses and propagation losses for a thin active layer<sup>47</sup>. Since only the TE mode is important for the thickness of the waveguides considered in this work, TM modes will not be discussed further.

The TE mode has only three components:  $E_y$ ,  $H_x$ ,  $H_z$ . Since  $E_z=0$ , and all transverse field components are independent of  $y$  for the dielectric slab waveguide shown in Figure 4.2,  $E_x=H_y=0$ . The component  $E_y$  satisfies equation 4.6. This leads to<sup>46</sup>

$$\frac{d^2 E_y}{dx^2} + (k^2 + \gamma^2) E_y = 0 \quad (4.7)$$

The remaining components follow from equations 4.4c, 4.5b and 4.5c and are given by

$$H_x = \frac{i\gamma}{\omega\mu} E_y \quad (4.8)$$

$$H_z = \frac{i}{\omega\mu} \frac{\partial E_y}{\partial x} \quad (4.9)$$

The solution for  $E_y$  can be divided into three different cases:

- 1) the mode is completely trapped,
- 2) the mode decays exponentially in one direction and radiates in the other,

3) the mode radiates to infinity on both sides.

The first case is the guided mode and the second and third are called the radiation modes. Figure 4.3<sup>48</sup> illustrates the three cases.

#### 4.2.2 Stripe Geometry Waveguide

Waveguiding in stripe geometry lasers in the plane perpendicular to the laser junction is due to the abrupt and relatively strong waveguide created by the heterostructure. Waveguiding in the lateral direction, ie. along the junction and transverse to the direction of propagation, is affected by various mechanisms. Lateral variations in gain<sup>48</sup>, represented as changes in the imaginary part of the refractive index, gives rise to gain-guiding. The decrease in real refractive index proportional to gain<sup>49</sup>, or the increase in real refractive index with temperature<sup>50</sup>, ie. in general the variation in real part of refractive index gives rise to index-guiding. If the imaginary and/or real spatial dependence of the refractive index is parabolic, the lateral mode functions are Gaussian-Hermite. Experimental evidence that waveguiding in narrow stripe lasers results primarily from lateral variations in gain was given by T.L. Paoli<sup>51</sup>. Another theoretical analysis of waveguiding in very narrow stripe lasers can be found in the paper by Streifer et al<sup>52</sup>.

For determining the field at the waveguide-air interface, a simple dielectric waveguide structure is used in this work. The details of the solution of this problem are discussed in the next few sections.

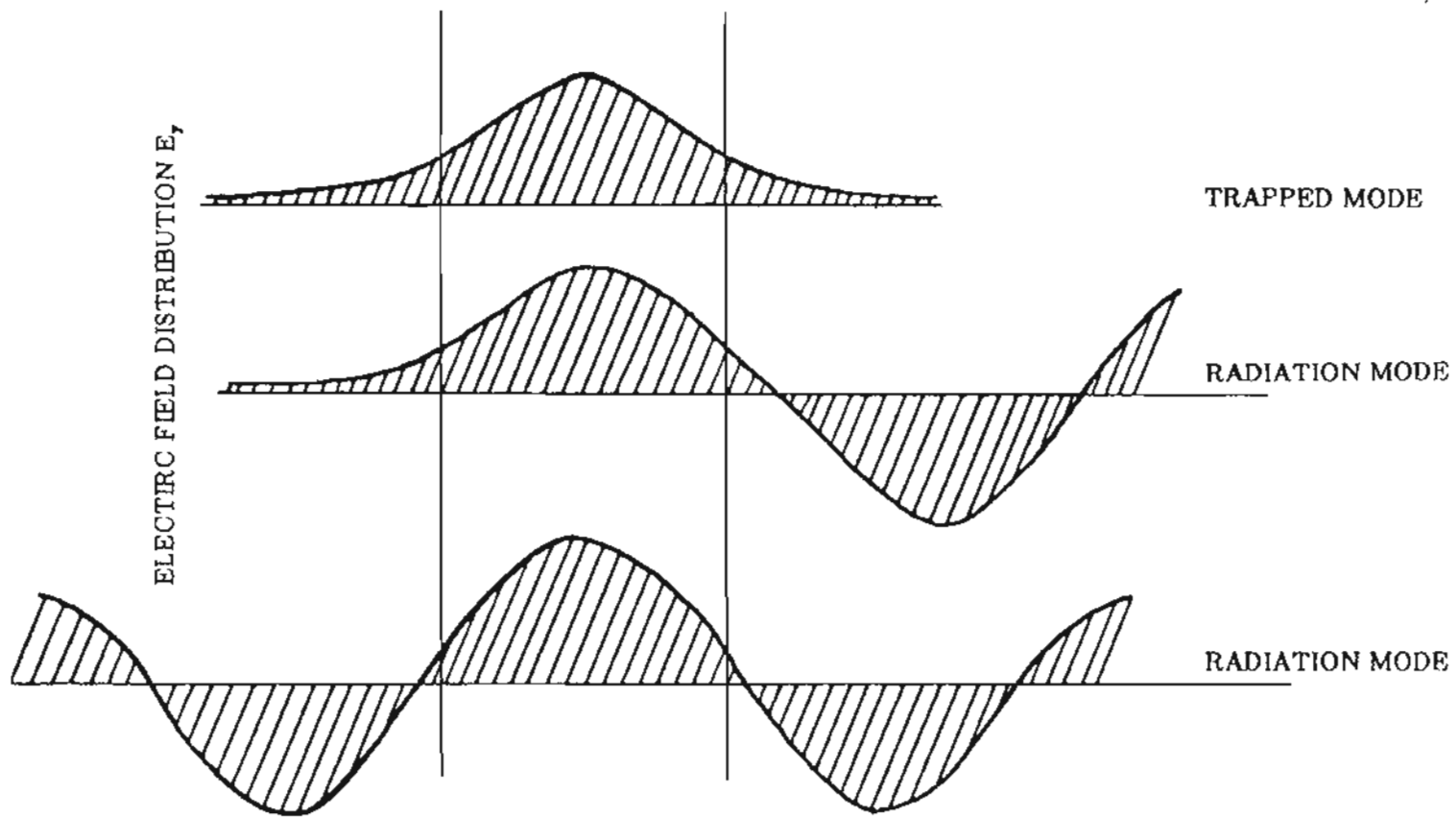


Figure 4.3 Electric field distribution of various modes supported by a lossless three-layer waveguide in the transverse direction.[46]

### 4.3 Formulation of the problem

A schematic of the laser diode and its external turning mirror used to simulate the farfield pattern is shown in Figure 4.4. The width of the active region is  $2d$ ,  $h$  is the depth of center of the active region from the surface of the laser and  $t$  is the distance of the turning mirror from center of the active region. The figure shows a  $45^\circ$  turning mirror, which was the nominal shape of the mirror used for the experimental part of this work. But the computer simulation can be used for determining the farfield pattern for other shapes of the turning mirror as well. The mirror reflects the light perpendicular to the surface and the farfield pattern is observed at the plane P. To determine the intensity distribution at P, the intensity distribution at the laser facet and at the turning mirror must be determined first.

The first attempt to solve the problem was made by using scalar diffraction theory. This states that <sup>53</sup>

$$U_2(P_2) = \frac{i}{\lambda} \iint U_1(P_1) \exp \frac{(-ikr)}{r} \cos(n, r) ds \quad (4.11)$$

where  $U_2(P_2)$  is the complex amplitude of the field at the observation point,  $U_1(P_1)$  is the complex field at the turning mirror,  $n$  is the outward normal unit vector to the aperture plane and the integral is over the mirror surface.  $U_1(P_1)$  was assumed to be a Gaussian. The results for the farfield pattern obtained using this approach, for a Gaussian with spot-sizes  $2\mu m$  and  $5\mu m$  at the laser output mirror are shown in Figures 4.5a and 4.5b. Comparing this with the experimental result obtained earlier<sup>9</sup> for a surface-emitter with a  $45^\circ$  turning

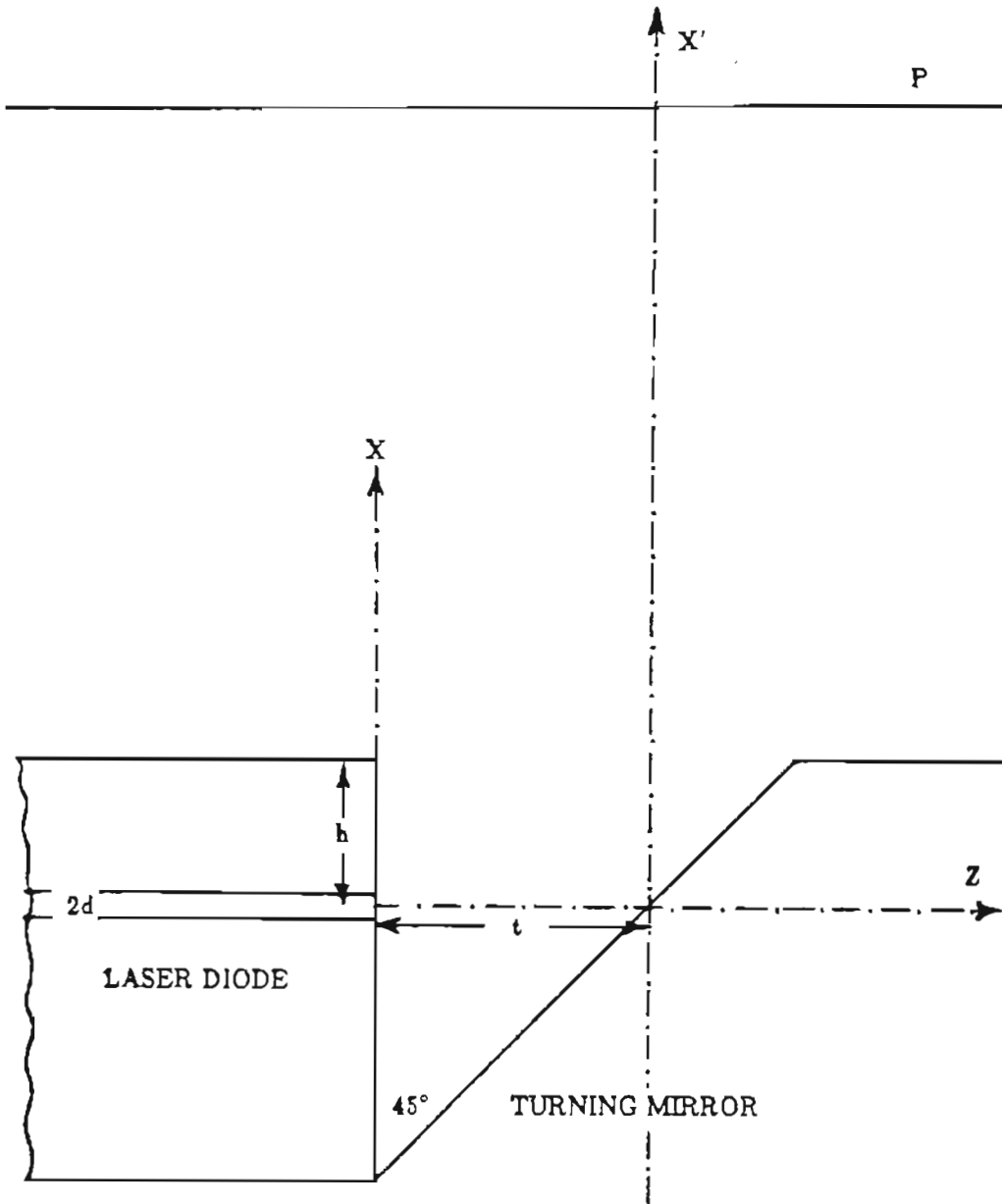


Figure 4.4 Schematic of a surface-emitting laser with a  $45^\circ$  turning mirror used for modeling farfield pattern.

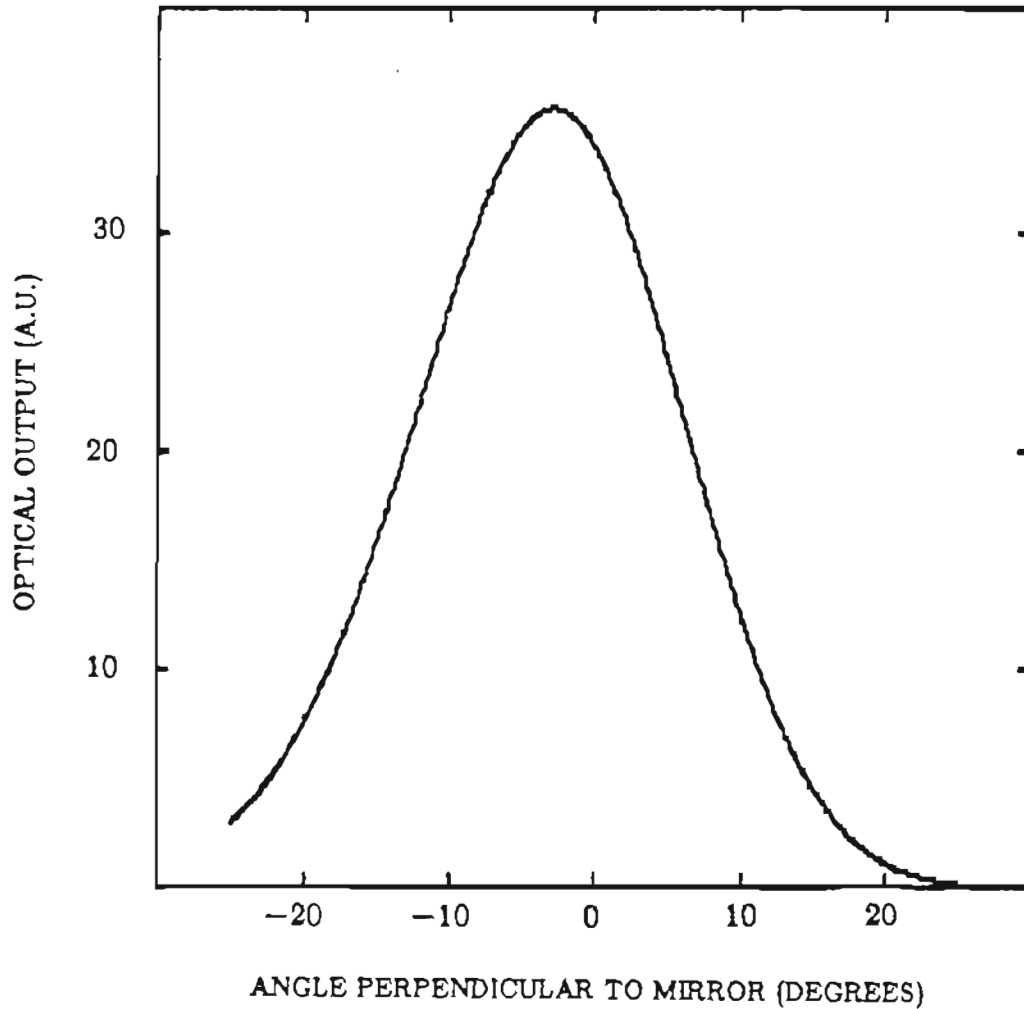


Figure 4.5a Theoretical farfield pattern for a surface-emitter with a  $45^\circ$  turning mirror due to a Gaussian of spot-size  $2 \mu m$  at the laser output mirror. The pattern was obtained using scalar diffraction theory given by equation 4.11.

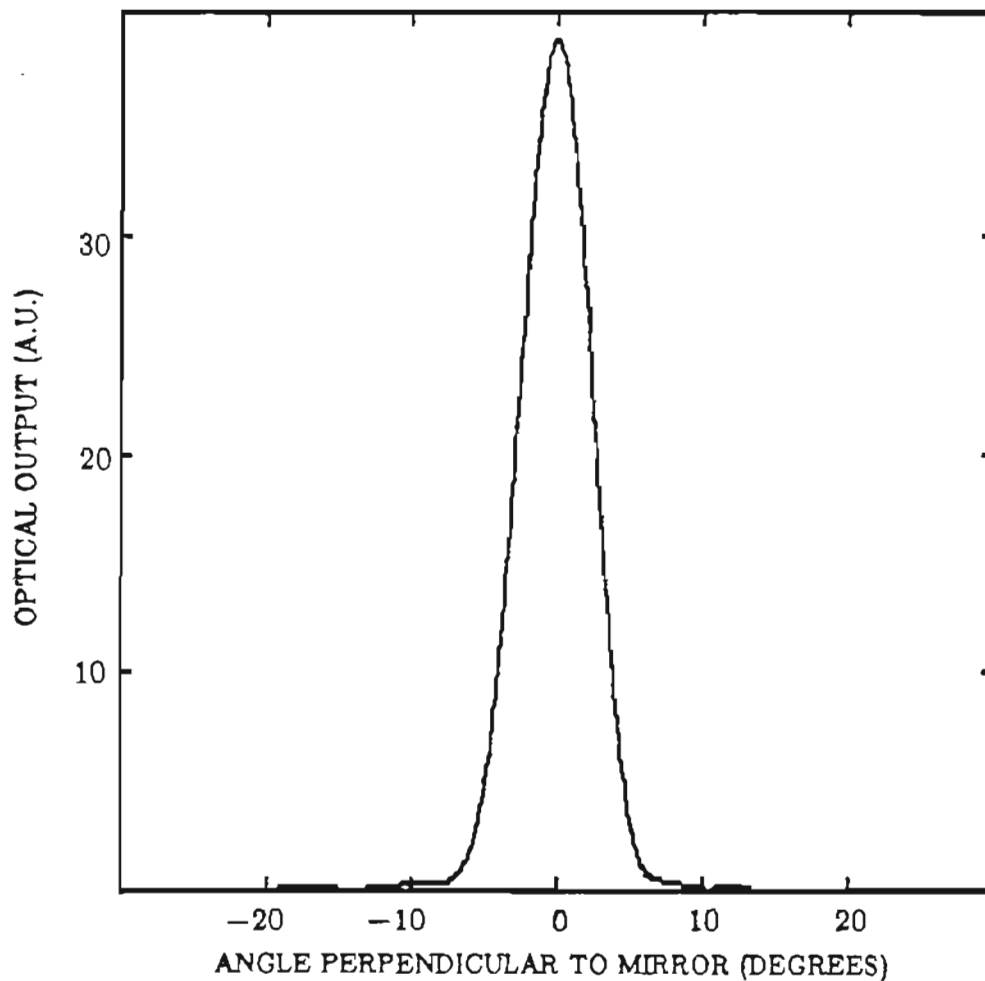


Figure 4.5b Theoretical farfield pattern for a surface-emitter with a  $45^\circ$  turning mirror due to a Gaussian of spot-size  $5 \mu m$  at the laser output mirror. The pattern was obtained using scalar diffraction theory given by equation 4.11.

mirror, shown in Figure 4.6a, it is obvious that there is no match. From Figure 4.6b, which represents the farfield from an edge emitter laser of the same material as the surface-emitter, the correct spot size was calculated using the formula  $\omega_0 = \frac{\lambda}{\pi\theta}$ , where  $\omega_0$  is the spot size,  $\lambda$  is the free-space wavelength and  $\theta$  is the half width at  $1/e^2$  intensity. The spot size was calculated to be  $0.79\mu m$ . Since this approach failed to give satisfactory results, the integral theorem of Helmholtz and Kirchoff was used. This states that<sup>54</sup>,

$$U(P) = \frac{1}{4\pi} \iint_S \left\{ U \frac{\delta}{\delta n} \frac{e^{ikr}}{r} - \frac{e^{ikr}}{r} \frac{\delta U}{\delta n} \right\} ds \quad (4.12)$$

where  $U$  was assumed to be a Gaussian and the integration was carried out over the surface  $S$  of the turning mirror. Figures 4.7a and 4.7b give the results obtained for two different spot sizes at the interface. It is seen that as one approaches the calculated spot size of  $0.79\mu m$ , the pattern diverges away from the experimentally observed output of Figure 4.6a.

Hence, it is obvious that the the beam in the gap between the waveguide termination and turning mirror is not a Gaussian and that solution to this problem requires a more complete treatment of the boundary conditions at the waveguide-air interface than is usually necessary. An exact formulation of the problem can be obtained by including the mode coupling at the mirror into the continuum of unguided radiation modes to the right of the interface. A rigorous theory using variational treatment of the diffraction at the facet of the laser diode has been developed by T. E. Rozzi and G. H. int' Veld<sup>55,56</sup>. Another thorough treatment of the problem of finding the field at the output

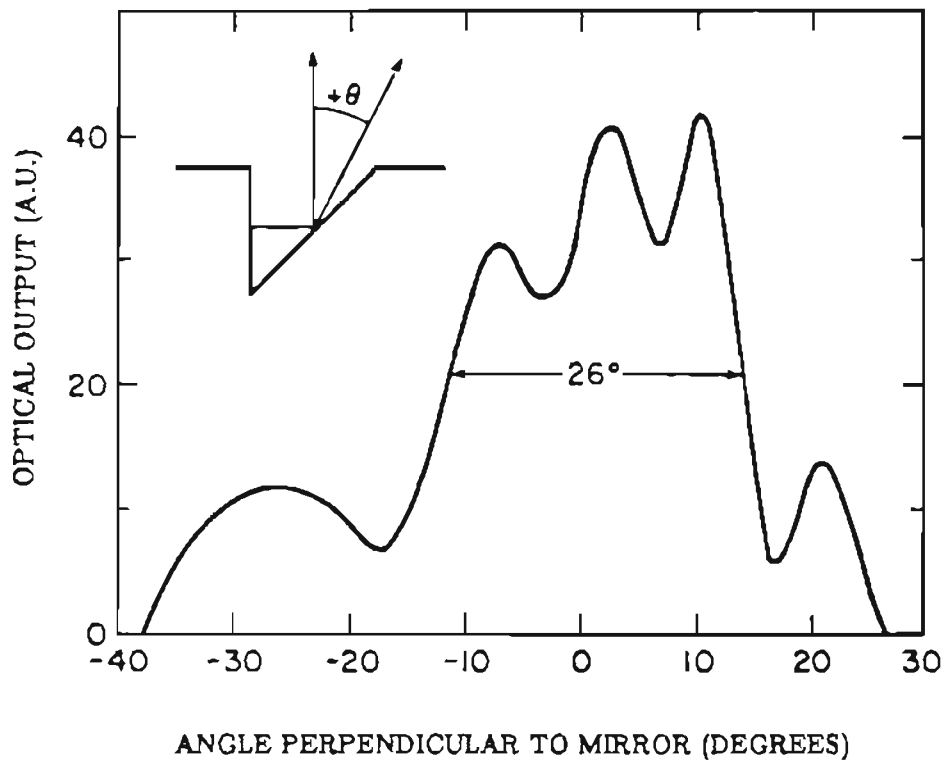


Figure 4.6a Experimentally measured farfield pattern from a surface-emitter with a 45° turning mirror.[9]

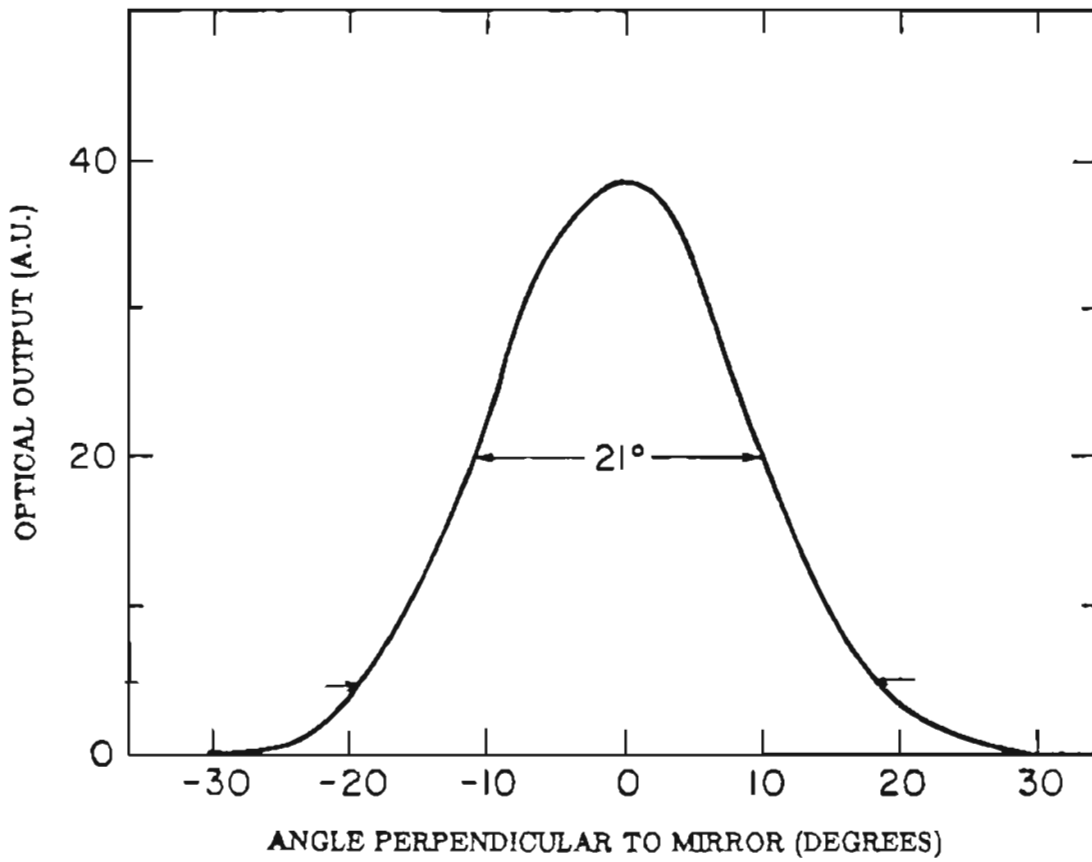


Figure 4.6b Experimentally measured farfield pattern from an edge-emitter laser of the same material as the surface-emitter with a farfield pattern illustrated in Figure 4.6a.[9]

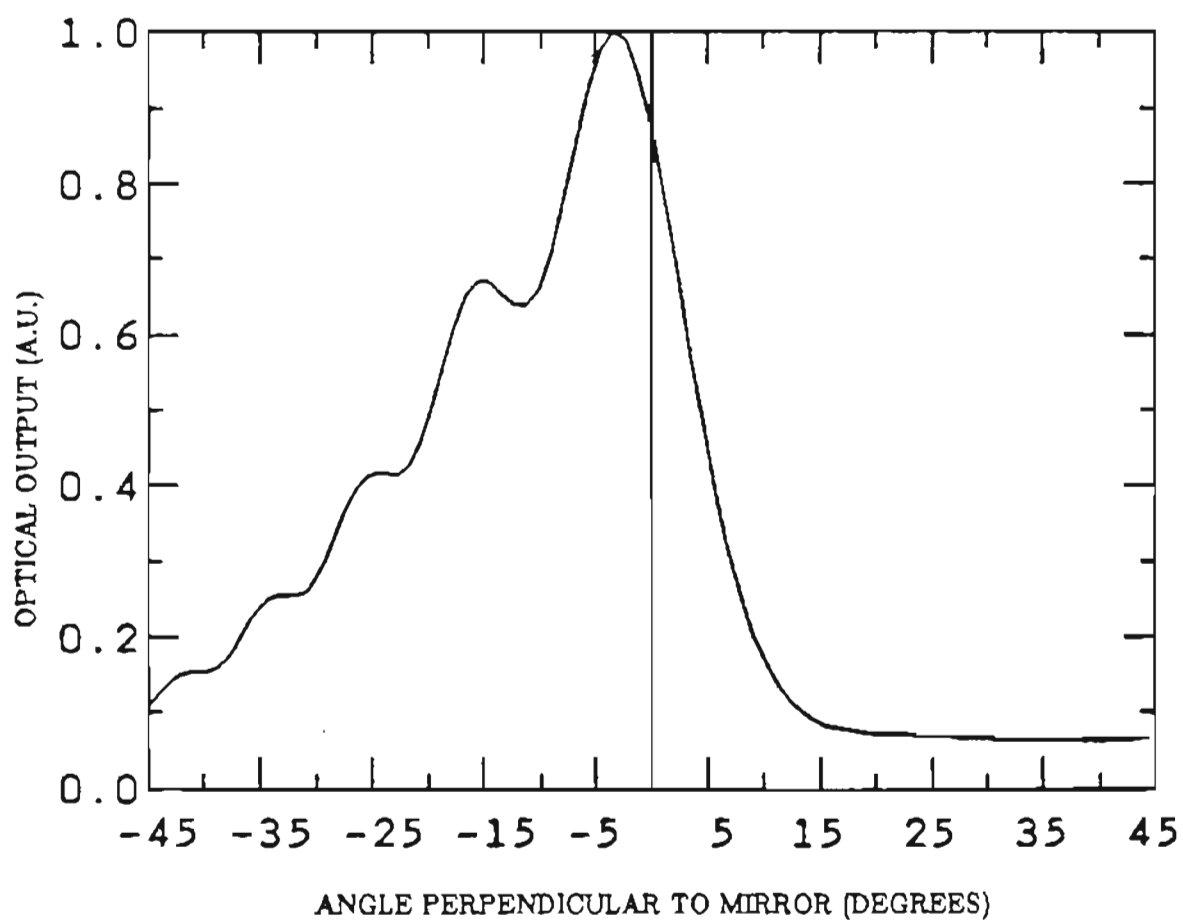


Figure 4.7a Theoretical farfield pattern for a surface-emitter with a  $45^\circ$  turning mirror due to a Gaussian of spot-size  $0.2 \mu\text{m}$  at the laser output mirror. The pattern was obtained using integral equation of Helmholtz and Kirchoff given by equation 4.12.

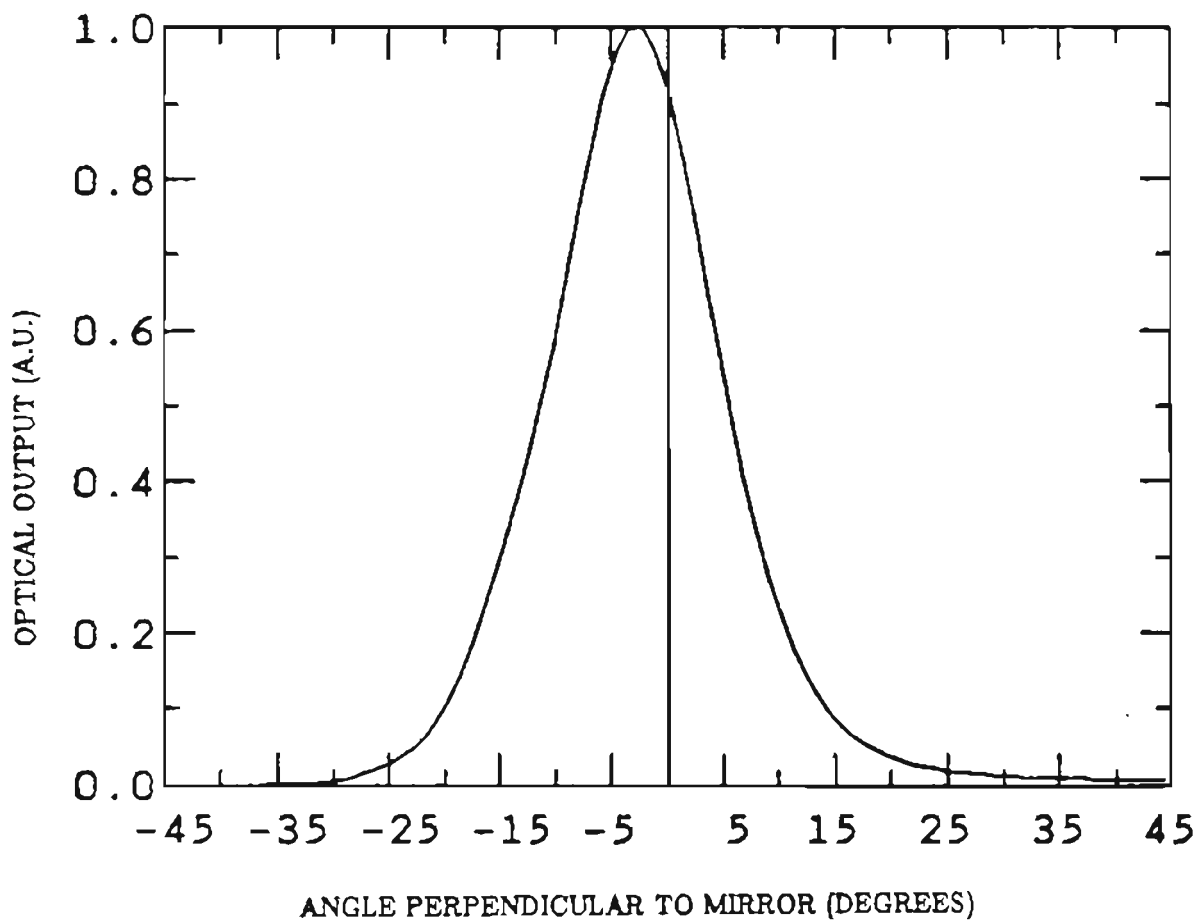


Figure 4.7b Theoretical farfield pattern for a surface-emitter with a  $45^\circ$  turning mirror due to a Gaussian of spot-size  $0.8 \mu\text{m}$  at the laser output mirror. The pattern was obtained using integral integral equation of Helmholtz and Kirchoff given by equation 4.12.

facet of the laser can be found in the paper by Davies and Walpole<sup>11</sup>, and was used in this thesis to obtain the field at the laser-air interface. Although the Davies and Walpole used  $Pb_{1-x}Sn_xTe$  system, the theory presented is valid for any other diode laser system.

#### 4.3.1 Waveguide Model For Computer Simulation

In order to obtain an exact formulation of the output coupling, it is desirable to simplify the theoretical model consistent with the accuracy. The schematic of the model is shown in Figure 4.8<sup>11</sup> It is an idealized three-layered structure terminated by free space in the plane  $z = 0$ , which is normal to the direction of propagation through the guide.  $\epsilon_1$ ,  $\epsilon_2$  and  $\epsilon$  are the dielectric constants of core, cladding and free-space respectively. The distance of any point on the right of the plane  $z = 0$  is given by  $r$  and the cladding layer is assumed to be much thicker than the active layer. The two-dimensional guide is made symmetric and free of irregularities so that no coupling can exist between modes of different parity or different polarization. Only the case where the lowest order TE mode is incident on the waveguide termination is considered. The theory is valid for guiding regions sufficiently thin so as to allow only the lowest order TE mode propagation. By restricting the thickness in this manner, we need consider mode conversion only to the continuum of unguided radiation modes rather than to other higher order modes. The dielectric constant  $\epsilon$  is treated as totally real, ie. the waveguide is treated as passive and lossless.

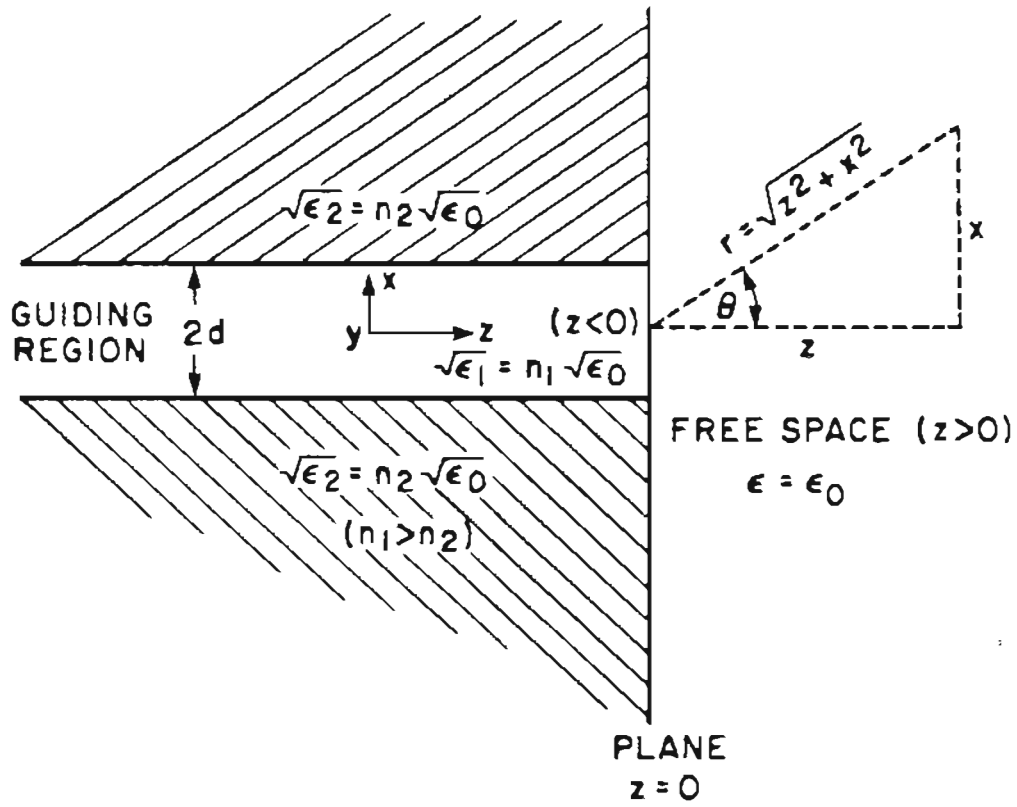


Figure 4.8 Schematic of waveguide model to calculate field at the plane  $z=0$ . [11]

#### 4.4 Theoretical Formulation

The theory discussed in this section can be found in the paper by Davies and Walpole<sup>11</sup>. Maxwell's equations for a symmetric waveguide and for a wave propagating with a time dependence  $e^{i\omega t}$  are

$$\nabla \times E(r) = -i\omega\mu_o H(r) \quad (4.13a)$$

$$\nabla \times H(r) = i\omega\epsilon(x)E(r) \quad (4.13b)$$

Combining the two equations yields

$$\nabla^2 E(r) + \mu_o\epsilon(x)\omega^2 E(r) = 0 \quad (4.14)$$

For the fundamental TE mode propagating through the guide,

$$E(r) = \hat{y}E(x,y) \quad (4.15)$$

Substituting this equation in 4.13a and 4.13b gives

$$H(r) = \frac{i}{\mu_o\omega} \left\{ -\hat{x} \frac{\partial E(x,z)}{\partial z} + \hat{z} \frac{\partial E(x,z)}{\partial x} \right\} \quad (4.16)$$

The boundary condition at the free-space interface at  $z = 0$  are

$$E(x,0^-) = E(x,0^+) \quad (4.17)$$

$$\frac{\partial E(x,0^-)}{\partial z} = \frac{\partial E(x,0^+)}{\partial z} \quad (4.18)$$

Now, the field inside the waveguide can be written as

$$E(x,z) = E_o(x)e^{-i\beta_o z} + RE_o(x)e^{i\beta_o z} + \int_0^\infty d\gamma g(\gamma)E_\gamma(x)e^{i\beta_\gamma z} \quad (4.19)$$

In the above equation, the first two terms represent the incident and the reflected fields for the bound mode,  $R$  is the complex reflection coefficient,  $g(\gamma)$  is the reflection coefficient for radiation modes and  $\gamma$  is an arbitrary wave vector in the range  $0 \leq \gamma \leq \infty$ . The third term in the equation represents reflected

waves belonging to the continuum of even TE radiation modes. The fields  $E_o(x)$  and  $E_\gamma(x)$  can be determined by using the theory of a dielectric slab waveguide described in section 4.2.1. The expressions for  $E_o(x,z)$ ,  $E_\gamma(x)$ ,  $\beta_\gamma$ ,  $\beta_o$  and  $g(\gamma)$  are given in Appendix A, A1.1. Next, the free space field for  $z$  is written as

$$E(x,z) = \int_{-\infty}^{\infty} a(\sigma) e^{-i\beta(\sigma)z} e^{-i\sigma z} d\sigma \quad (4.20)$$

where,  $E(x,z)$  is expanded as a fourier integral with coefficients  $a(\sigma)$ . Expression for  $\beta(\sigma)$  is given in Appendix A, A1.1. Now, boundary conditions can be used to solve for  $R$ ,  $g(\gamma)$ , and  $a(\sigma)$ . The boundary conditions 4.17 and 4.18 give the following two equations

$$E_o(x)(1 + R) + \int_0^{\infty} d\gamma g(\gamma) E_\gamma(x) = \int_{-\infty}^{\infty} a(\sigma) e^{-i\sigma z} d\sigma \quad (4.21)$$

$$E_o(x)\beta_o(1-R) - \int_0^{\infty} d\gamma g(\gamma)\beta_\gamma E_\gamma(x) = \int_{-\infty}^{\infty} a(\sigma) e^{-i\sigma z} \beta(\sigma) d\sigma \quad (4.22)$$

Eliminating  $a(\sigma)$  between the two equations, one has

$$E_o(x)\beta_o(1-R) - \int_0^{\infty} d\gamma g(\gamma)\beta_\gamma E_\gamma(x) = \int_{-\infty}^{\infty} d\sigma \beta(\sigma) e^{-i\sigma z} \cdot \left[ (1 + R)E_o(\sigma) + \int_0^{\infty} d\gamma g(\gamma) E_\gamma(\sigma) \right] \quad (4.23)$$

Before solving for the field at the free-space interface,  $R$  and  $g(\gamma)$  must be determined from equation 4.22. The expressions for  $E_o(\sigma)$  and  $E_\gamma(\sigma)$  which are the fourier transforms of  $E_o(x)$  and  $E_\gamma(x)$  respectively and the details of the solution to determine  $R$  and  $g(\gamma)$  are given in Appendix A, A1.2. Just the final results are presented here. The field at the interface is given by

$$E(x,0) = (1 + R)E_o(x) + \int_0^{\infty} dt \bar{g}(t) \frac{\bar{E}_t(x)}{\beta_t} \quad (4.24)$$

where  $R$  and  $\bar{g}(t)$  are given by

$$R = \frac{1 - \bar{F}_o - \int_0^{\infty} \frac{dt}{\beta_t} \bar{F}(t) \bar{g}(t)}{1 + \bar{F}_o} \quad (4.25)$$

and

$$\bar{g}(t) = -2 \frac{\bar{F}(t)}{1 + \bar{F}_o} \frac{\beta_t}{[\beta_t + \sqrt{(k_o d)^2 - t^2}]} \quad (4.26)$$

Expressions for all the symbols used in the equation above are given in Appendix A, A1.2. Finally, the expression for  $F(t)$  and  $F_o$  are given by

$$\bar{F}_o = \frac{x_o}{(\beta_o d)} \frac{x_o^4 (1 + \tan^2 x_o)^2}{x_o + \cot x_o} \frac{4}{\pi} \int_0^{\infty} \frac{dy \sqrt{(k_o d)^2 - y^2}}{(y^2 + x_o^2 \tan^2 x_o)^2} \frac{(y \sin y \cos x_o - x_o \sin x_o \cos y)^2}{(y^2 - x_o^2)^2} \quad (4.27)$$

and

$$\begin{aligned} \bar{F}(t) = & \left[ \frac{1}{\pi(\beta_o d)} \frac{x_o}{x_o + \cot x_o} \frac{1}{t^2 \cos^2 x + x^2 \sin^2 x} \right]^{\frac{1}{2}} \\ & \left\{ 2 \sqrt{(k_o d)^2 - t^2} (t \cos x \cos t + x \sin x \sin t) \right. \\ & \left. \frac{(t \sin t \cos x_o - x_o \sin x_o \cos t)}{t^2 - x_o^2} \frac{x_o^2 (1 + \tan^2 x_o)}{t^2 + x_o^2 \tan^2 x_o} \right. \\ & \left. + \frac{4t}{\pi} (x^2 - t^2) \int_0^{\infty} dy Pr \left[ \frac{1}{y^2 - t^2} \right] \right. \\ & \left. \cdot \sqrt{(k_o d)^2 - y^2} \frac{(y \sin y \cos x - x \sin x \cos y)}{y^2 - x^2} \right. \end{aligned}$$

$$\left. \frac{(y \sin y \cos x_0 - x_0 \sin x_0 \cos y)}{y^2 - x_0^2} \frac{x_0^2 (1 + \tan^2 x_0)}{y^2 + x_0^2 \tan^2 x_0} \right\} \quad (4.28)$$

where the principal value is defined as given by equation A19, Appendix A, section A1.2. Simplifications for evaluating the principal value integral in equation 4.28 are given in Appendix B, B2.1 The interface electric field obtained from equation 4.24 numerically is shown in Figure 4.9. It can be seen that the total field at the mirror has a large component in phase with the incident  $TE_0$  mode and an out of phase component. In other words, the field due to radiation mode introduces an 'x' dependent phase. If one considers a Gaussian beam at the interface, then this phase dependence is not included and therefore accurate results cannot be obtained. Hence it is inappropriate to use a Gaussian beam. Two other approaches similar to this one are given by Ikegami<sup>47</sup> and Butler and Zoroofchi<sup>57</sup>. However, Ikegami does not consider the radiation modes in the calculation of reflectivity and in the Butler paper there is only an approximate treatment of the boundary conditions.

#### 4.5 Farfield Pattern

The field on the waveguide-air interface was calculated using equation 4.24. Now, the waveguide-air interface can be considered as an aperture on which field values are known and therefore diffraction theory can be used to determine the field at the turning mirror. The starting point for aperture diffraction problems is the Kirchoff diffraction theory according to which the field at a point due to diffraction at an aperture is given by,

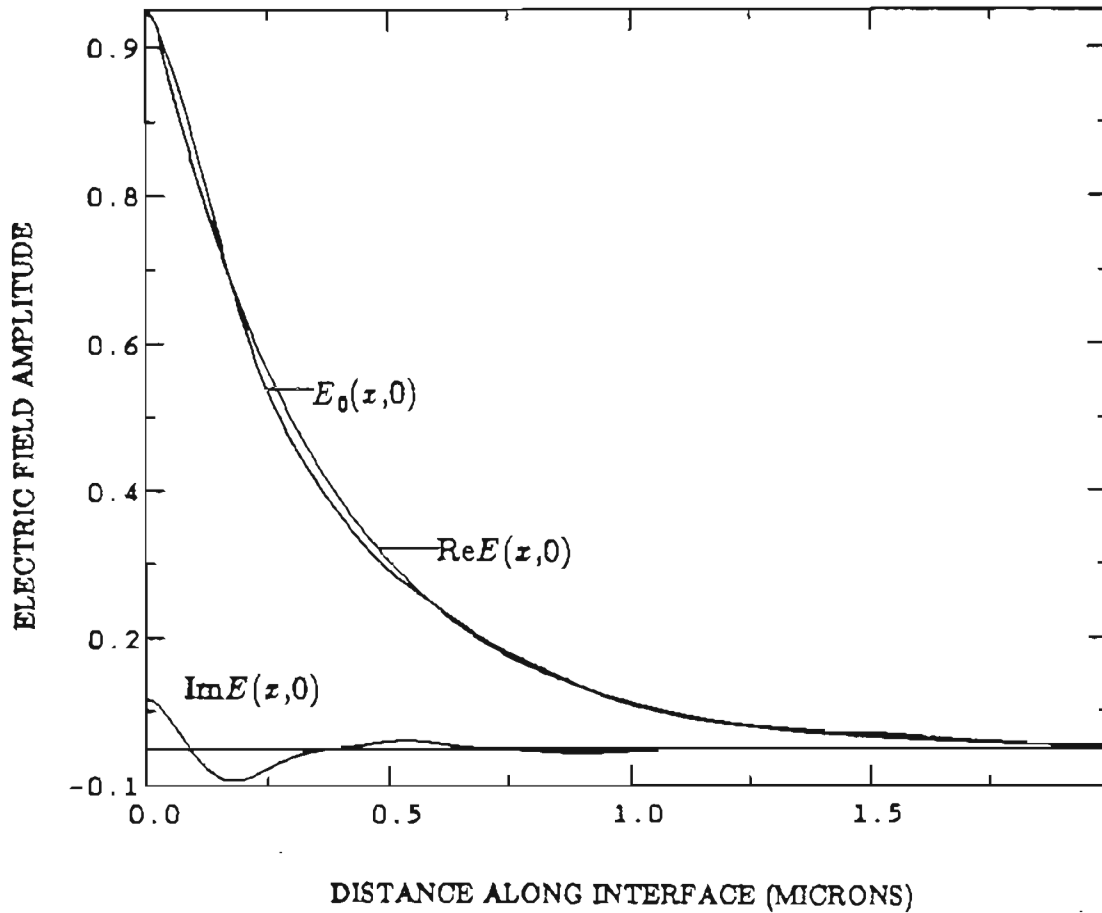


Figure 4.9 Field amplitude at the waveguide-air interface calculated using equation 4.24.  $E_0(x,0)$  is the guided wave and  $\text{Re}E(x,0)$  and  $\text{Im}E(x,0)$  represent the real and imaginary parts of the total field at the interface respectively. These include the field due to radiation modes.

$$U(x', z) = \iint_{\Sigma} \left( \frac{\partial U}{\partial n} \frac{e^{ikr}}{r} - U \frac{\partial}{\partial n} \frac{e^{ikr}}{r} dx \right) \quad (4.29)$$

where,  $\Sigma$  is the surface of the aperture and  $e^{ikr}/r$  is the three-dimensional Green's function for Helmholtz equation in three dimensional spherical coordinates. The schematic of the laser diode is shown in Figure 4.10. In the figure,  $AOC$  is the laser-air interface,  $CO'B$  is the  $45^\circ$  turning mirror,  $n$  is the normal to the interface and  $r$  is the distance of a point on the turning mirror to the interface  $AOC$ . The laser radiation first propagates in the  $Z$  direction and then in the  $X'$  direction after reflecting off the turning mirror.  $AGB$  is the opening or the aperture. The laser diode which was used to measure the farfield pattern was a ten stripe, phase locked device. But for the sake of simplicity of modeling the farfield pattern, a single emitter laser with an active region with width in the  $y$  direction much greater than the thickness was assumed. Also, the field was assumed to be distributed uniformly over the width. This assumption is valid since we are modeling the farfield pattern in a direction perpendicular and not parallel to the plane of the junction.

Therefore, with these assumptions, the surface integral in equation 4.29 reduces to a line integral over  $x$ . Hence one has to use a two-dimensional Green's function instead of three-dimensional Green's function. The two-dimensional Green's function for Helmholtz equation in cylindrical coordinates is given by Hankel function which is written as,

$$H_0^{(1)}(kr) = J_0^{(1)}(kr) + iY_0^{(1)}(kr) \quad (4.30)$$

where  $J_0^{(1)}(kr)$  and  $Y_0^{(1)}(kr)$  are Bessel functions of the first and the second kind respectively. The Hankel function represents a traveling cylindrical wave.

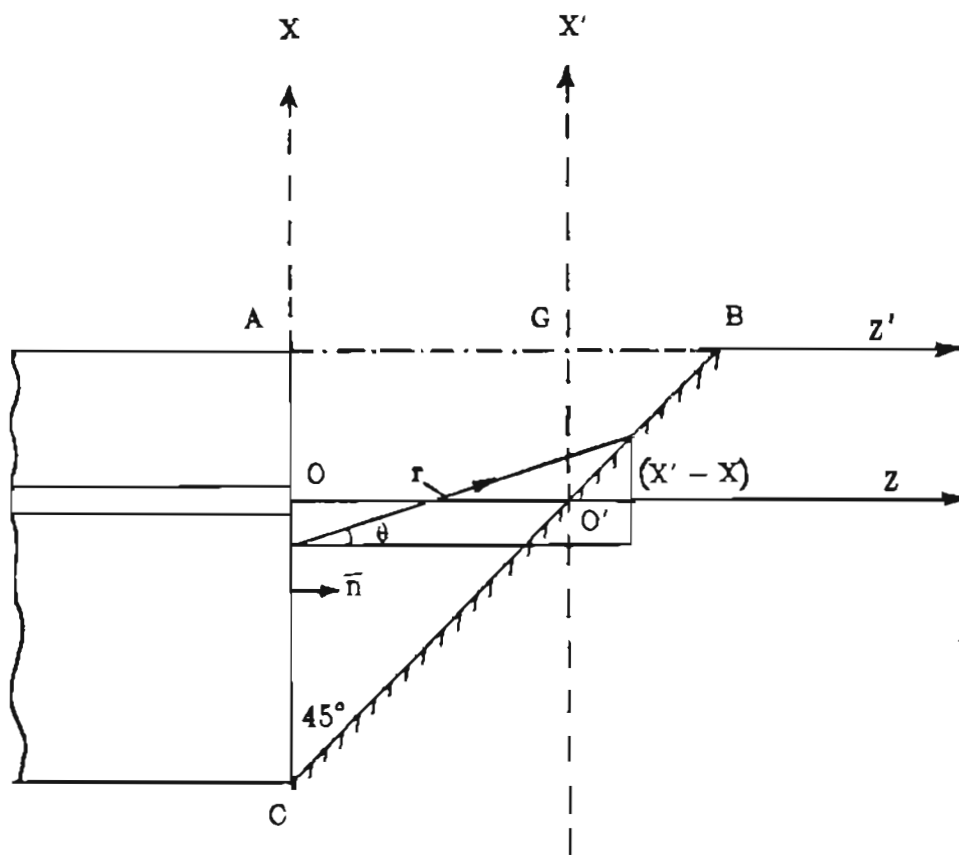


Figure 4.10 Schematic of the laser diode and 45° turning mirror used to calculate the farfield pattern from field at interface AOC

Since the the amplitude but not the derivative of the field is known at the interface, the Green's function is chosen such that it is zero on the aperture  $x_1x_2$ , where  $x_1$  and  $x_2$  represent the points on the interface  $AOC$  between which the field is nonzero. The expression for the Green's function used for modeling is given explicitly by equation B3, Appendix B, section B2.2. Therefore the field at any point on the turning mirror can be calculated by using the following formula.

$$U(x',z) = \frac{zk}{2} \int_{x_1}^{x_2} \frac{-(J_1b + aY_1)}{r} dx + i \int_{x_1}^{x_2} \frac{(J_1a - bY_1)}{r} dx \quad (4.31)$$

The details of the derivation of the equation 4.31 are given in Appendix B, B2.2. Next, equation 4.31 was used again to determine the field at aperture  $AGB$  as shown in Figure 4.10. This was done in order to avoid the shadow effect of the facet opposite to the turning mirror on the farfield pattern. The shadow effect comes about since all the points on the turning mirror do not contribute to the farfield on the left of  $AOC$ . This is because  $AOC$  blocks a part of the radiation. But if the field at the aperture  $AGB$  were calculated first, the above problem will not arise. It is important to consider this since one needs to know the angular spread from  $-40^\circ$  to  $+40^\circ$  from the vertical. The farfield at plane P was then calculated from the field at the aperture. But there is also a direct contribution from the laser facet to the farfield pattern. This represents the fraction of light radiated from oscillator mirror which does not reflect from the turning mirror. Therefore, the total field at the plane P is the sum of the farfields due to field at the facet and field at the aperture  $AGB$ . The computer programs for these simulations are given in Appendix C.

The next chapter illustrates the results obtained from the computer simulation and experiment. Cases of a straight  $45^\circ$  turning mirror and a parabolic turning mirror are considered. The straight mirror was micromachined at OGC and the farfield pattern was measured with the setup described in Chapter 5. For the parabolic mirror, the results presented by Walpole and Liao<sup>7</sup> were used for a comparison.

## 5. EXPERIMENT

This chapter begins by describing the focused ion beam micromachining technique which was used to mill turning mirrors on a ten stripe phase-locked diode laser array. The experimental setup and procedure used to measure the farfield pattern is also explained in detail. The last section of the chapter gives the specifications of the surface-emitter used for the measurement and modeling the farfield pattern.

### 5.1 Focused Ion Beam Micromachining

A fine focused ion beam generated from a liquid metal ion source has a great potential for applications such as direct implantation, ion beam lithography and microanalysis, because of its high current density, capability for very fine focusing, and the wide variety of ion species available. Focussed-Ion-Beam Micromachining (FIBM) is another interesting area which has many applications. Selective machining on submicrometer scales of many materials of technological importance, semiconductor optoelectronic materials in particular, is possible with this micromachining technique<sup>8,9,58-62</sup>.

An important factor behind designing high yield, low threshold, high modulation capability devices is making end mirrors which define the optical cavity. The method of cleaving the substrate material to form the laser facets

is not an efficient and reliable method of generating laser mirrors internal to an integrated system. Other techniques for making cavity mirrors include, wet chemical etching<sup>63,64</sup>, broad ion beam milling<sup>65,66</sup>, reactive ion etching<sup>67,68</sup>, microcleaving<sup>69</sup>, and chemical etching with subsequent mass transport<sup>70</sup>. The advantages of micromachining over these methods are,

1. machining without masks can be performed which allows one to create complex topographies on semiconductor material without multiple photolithographic processes,
2. there are more choices of materials than other methods,
3. sample observations can also be performed using the fine focused ion beam as a scanning ion microscope<sup>71</sup>.

### 5.1.1 Micromachining System

The focused ion beam system can be thought of as composed of three main parts: the ion source, the optical column, and the sample displacement table as shown in Figure 5.1<sup>8</sup>. A liquid metal ion source (LMIS) is used in the focussed ion beam system used to fabricate the turning mirrors at OGC. In these sources a reservoir of liquid metal is maintained near one end of a sharp tungsten needle. The metal wets the needle and flows down to the tip which has a radius of about 10  $\mu m$ . The tip of the needle faces an extraction aperture, some distance below it. In the presence of a high electric field the liquid at the end of the needle is pulled into a conical shape (Taylor cone) under the combination of electrostatic stress and surface tension. At the apex of the cone

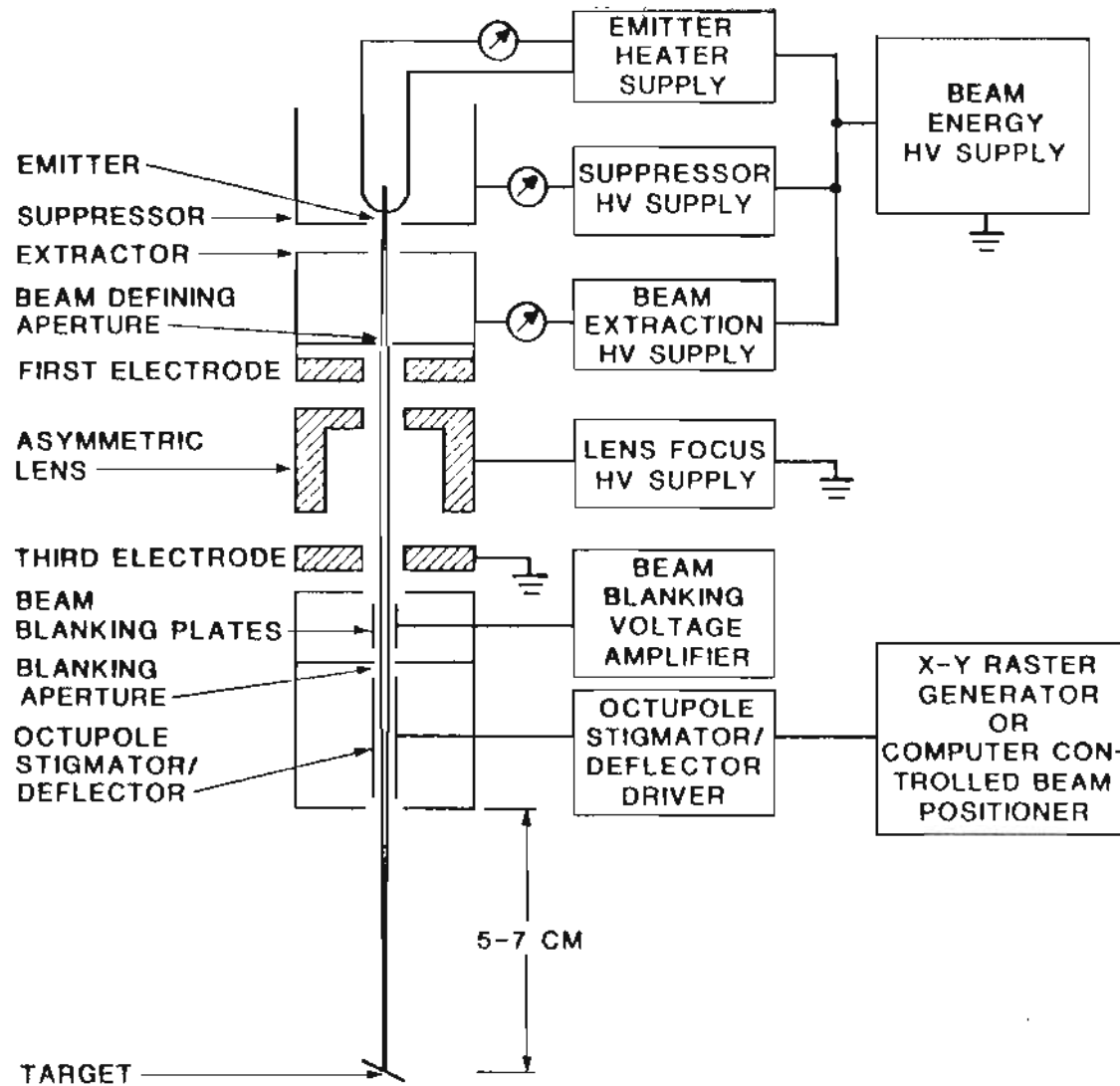


Figure 5.1 Schematic of the FIB optical column and control system. [8]

the electric field exceeds that needed to cause field evaporation of the liquid metal ions. The most commonly used liquid metal is *Ga* since it is liquid near room temperature, has a low vapour pressure and yields a long lifetime source of predominantly  $Ga^+$  ions with almost no emission of other mass and charge species. The optical column<sup>72</sup> focuses ions from the source onto the sample and is very much analogous to an optical lens which may focus a source of light in one plane onto another plane. Ion lenses are for the most part electrostatic and consist of two (or more) precisely machined axially symmetric electrodes at some high potentials. This electrostatic lens column as shown in Figure 5.1 delivers a current density of approximately  $1A/cm^2$  into a focussed spot  $250\text{ nm}$  in diameter. A focused ion beam which is to be used for beam writing over an extended area needs a beam blanker, ie. a means of turning the beam off. This is generally done by having a pair of electrodes on opposite sides of the beam and applying a voltage between them so that the beam is deflected sideways and is not capable of passing through an aperture located downstream. Under computer control the spot can be scanned over a  $1\text{ or }2\text{ mm}^2$  area with  $500\text{ nm}$  precision. This allows complete control of the ion dose to any pixel within the scanned area. A pixel actually means a picture element. Since the scanned area is viewed with a TV monitor, the scanning area is divided into the number of pixels or picture elements of the monitor. At normal incidence the etch rate in  $GaAs^8$  is approximately  $0.25\mu m^3s^{-1}$ .

### 5.1.2 Micromachining Procedure

To perform micromachining the FIB is used in the SIM mode, and the specimen stage is moved to properly position the target. The ion dose, which determines the sputter depth, is controlled by the dwell time of the beam at each point in the rastered area, and the number of times the area is rastered. Smooth surfaces are obtained by overlapping Gaussian beam spots by at least a half-width (beam radius) while rastering<sup>71</sup>. Arbitrary shapes can be produced using two different methods. For example, a V-shaped groove can be formed by rastering over a series of successively narrower rectangles on a common center or by using a deflecting voltage which varies quadratically with time in the x and y directions<sup>8,61</sup>. A sinusoidal surface can also be formed by programming the beam position to follow an inverse cosine time behaviour<sup>8,61</sup>. Redeposition of sputtered atoms on to the newly machined surface is a problem common to all ion milling techniques. For machining the end mirrors of a laser cavity, the problem can be minimized by initiating the beam scan at the cleaved facet and progressively moving the beam further into material to obtain a smooth laser facet<sup>59</sup>. The problem of redeposition is more pronounced for a slow scan than for a fast repetitive scan<sup>73</sup>.

## 5.2 Experimental Setup For Measuring Farfield Patterns

Figure 5.2 shows the relevant parameters associated with the pattern characteristics. The y axis is directed along the junction plane whereas the x axis is perpendicular to the junction plane. The figure illustrates the radiation field of the fundamental mode. The half-power beam width in the junction plane is  $\theta_{||}$  and the pattern beam width perpendicular to the junction plane is

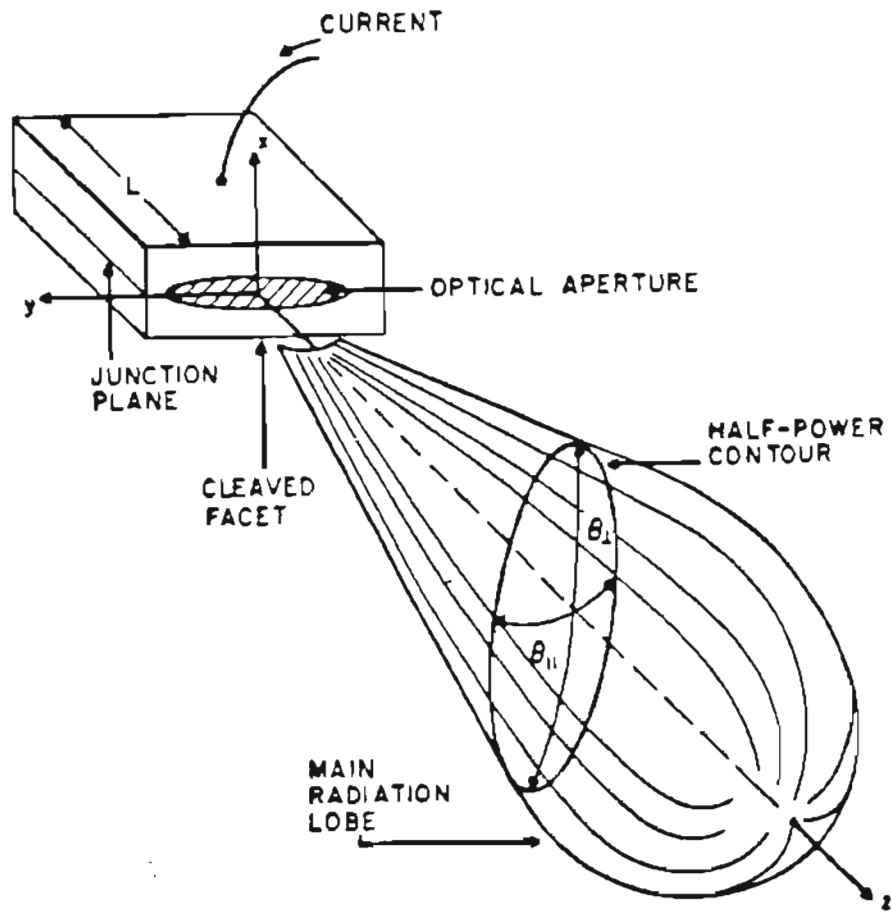


Figure 5.2 Schematic of the radiation pattern of a laser diode. [48]

$\theta_{\perp}$ . This section describes the experimental setup used for measuring  $\theta_{\parallel}$  and  $\theta_{\perp}$  for a turning mirror surface emitting laser diode. The setup used for the real time measurement of the farfield pattern of a diode laser is shown in Figure 5.3a and 5.3b. The laser mount can hold the laser in a vertical position so that the farfield pattern of an edge emitter is obtained, or in the horizontal position so that the farfield of a surface-emitter is obtained. The farfield is then imaged by a high sensitivity, high resolution CCD camera, Sony model number 57/57CE. This camera uses a  $8.8\text{mm} \times 6.6\text{mm}$  CCD solid state image sensor. No lenses were used to image the farfield. Instead light was directly collected by placing the camera very close to the laser diode. The camera could image about 70 degrees parallel to the junction and 80 degrees perpendicular to the junction. The image was then recorded with a commercial video cassette recorder (VCR). As seen in the Figure 5.3b, the VCR is connected to a ROBOT Model 650 television frame grabber for interfacing between television camera and a computer. A  $256 \times 256 \times 6$  bit deep frame store memory contained in the model 650 permits a picture to be frame grabbed from the VCR and supplied to the computer. Frame grabbed memory contents can be viewed on a television monitor.

Next, the "windows" program on the APPLE computer was used to choose a window on the farfield pattern viewed on the television screen. The program averages the optical intensity over the width of the window for each pixel in the vertical direction and stores the pixel number vs average intensity in a file. This file is then transferred to the microvax and the program 'fwhm.f' used for finding the full width at half maximum (FWHM) of  $\theta_{\perp}$ . The oscilloscope con-

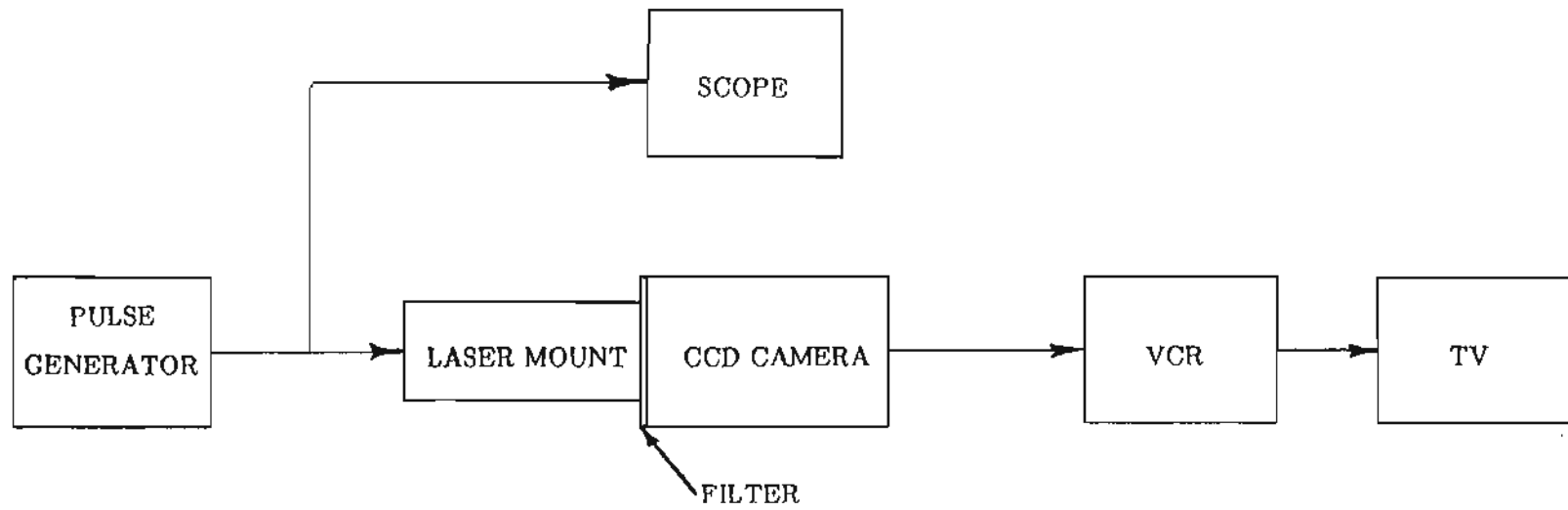


Figure 5.3a Schematic of the experimental setup to measure the farfield pattern of a laser diode.

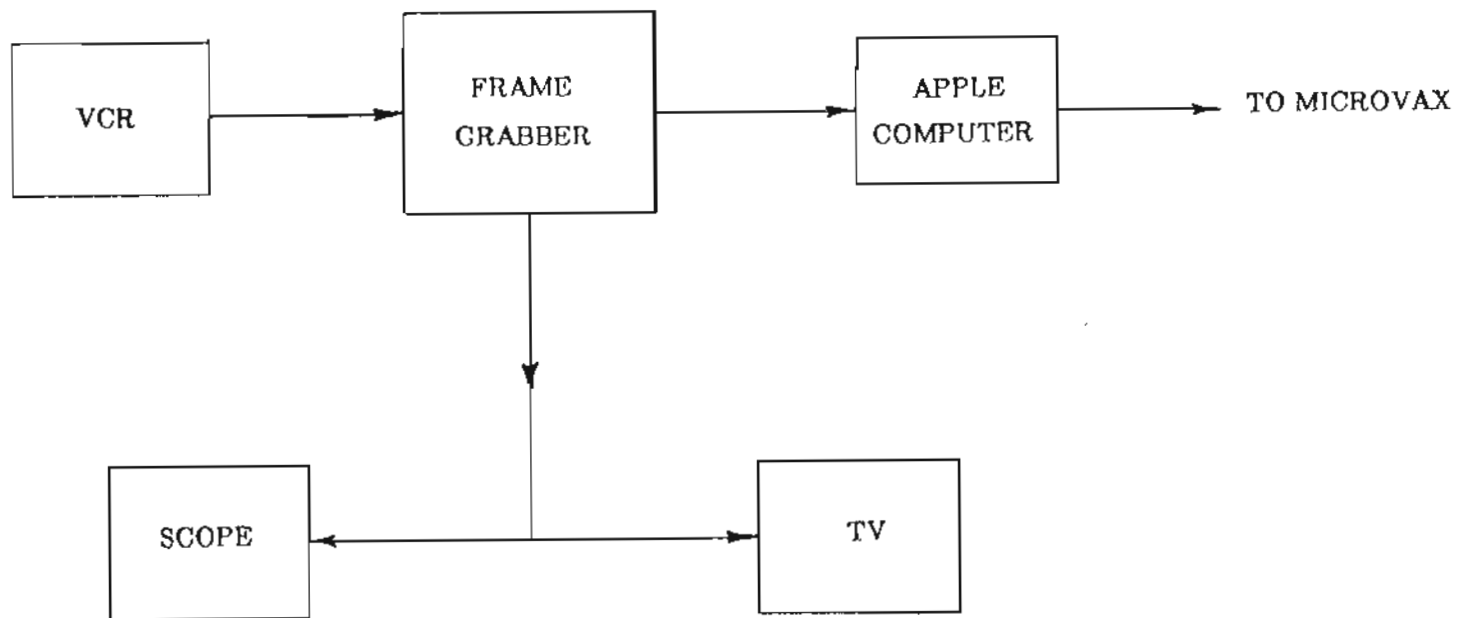


Figure 5.3b Schematic of the experimental setup to transfer the frame grabbed data to the microvax.

nected to the frame grabber was used to display the farfield parallel to the junction plane. The oscilloscope screen was calibrated to read angular spread directly. Hence, FWHM of different lobes in the farfield pattern and the separation between the lobes could be accurately measured, both in parallel and perpendicular directions to the junction plane. The results of these measurements are given in the next chapter along with the results obtained by computer simulation.

### 5.3 Specifications Of The Laser Diodes

#### a.) 45° Turning Mirror

The Y-180Z ten stripe phase-locked *GaAlAs/GaAs* laser diode, with a 45° turning mirror was micromachined with the micromachining facility available at OGC. The values of various parameters used for the computer simulation are as follows:

Thickness of active region =  $0.06\mu m$ ,

Refractive index of active region or core = 3.61,

Refractive index of cladding = 3.38,

Wavelength of light in vacuum =  $0.8\mu m$ .

The thickness of active region and the refractive indices were calculated from the data given in a paper by D. R. Scifres et al<sup>19</sup> and that in Figure 1 in a paper by H. C. Casey et al<sup>74</sup>.

#### b.) Parabolic Turning Mirror

The parabolic turning mirror was fabricated by smoothing a chemically etched

multistep structure using mass transport in a *GaInAsP/InP* system<sup>7</sup>. The refractive indices for core and cladding and the free space wavelength were determined from the *GaInAsP* composition.<sup>75</sup> The information about the composition of *GaInAsP* was given to the author by Dr. J. N. Walpole, MIT Lincoln Laboratories.

Thickness of active region or core =  $0.2\mu m$ ,

Refractive index of core = 3.49,

Refractive index of cladding = 3.19,

Free space wavelength =  $1.34\mu m$ .

The equation for the shape of the mirror was determined by measuring coordinates of points from the optical micrograph of the surface of the parabolic mirror<sup>7</sup>, and fitting a fourth order polynomial to these points. The fitted curve and the optical micrograph from the paper mentioned above is shown in Figure 5.4a and 5.4b respectively. The next chapter illustrates the farfield patterns obtained from experiment and computer simulation.

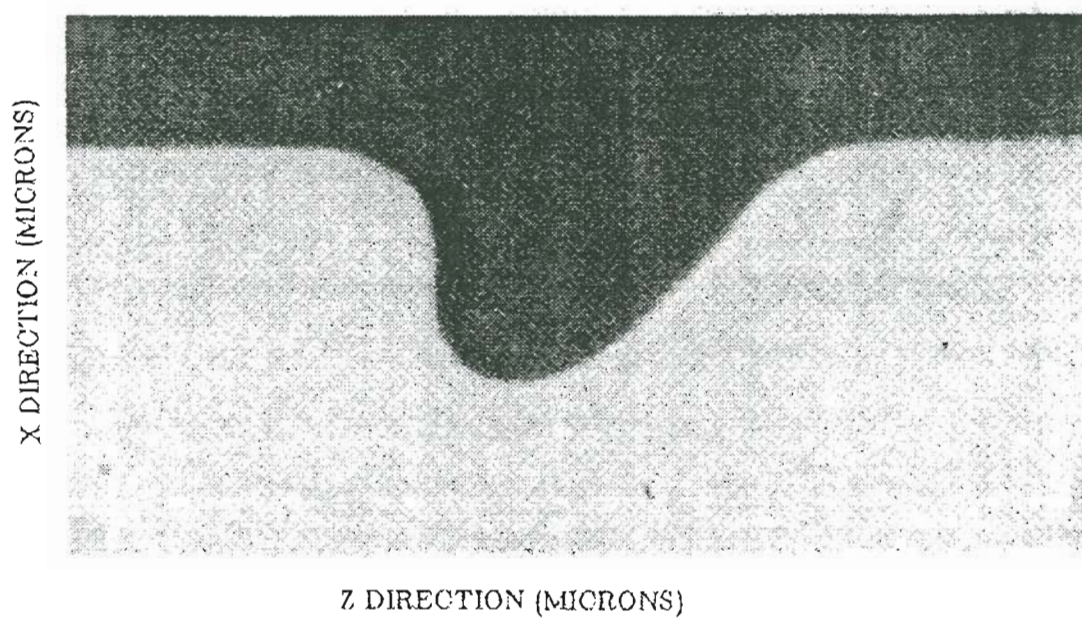


Figure 5.4a SEM picture of the parabolic turning mirror cross-section. [7]

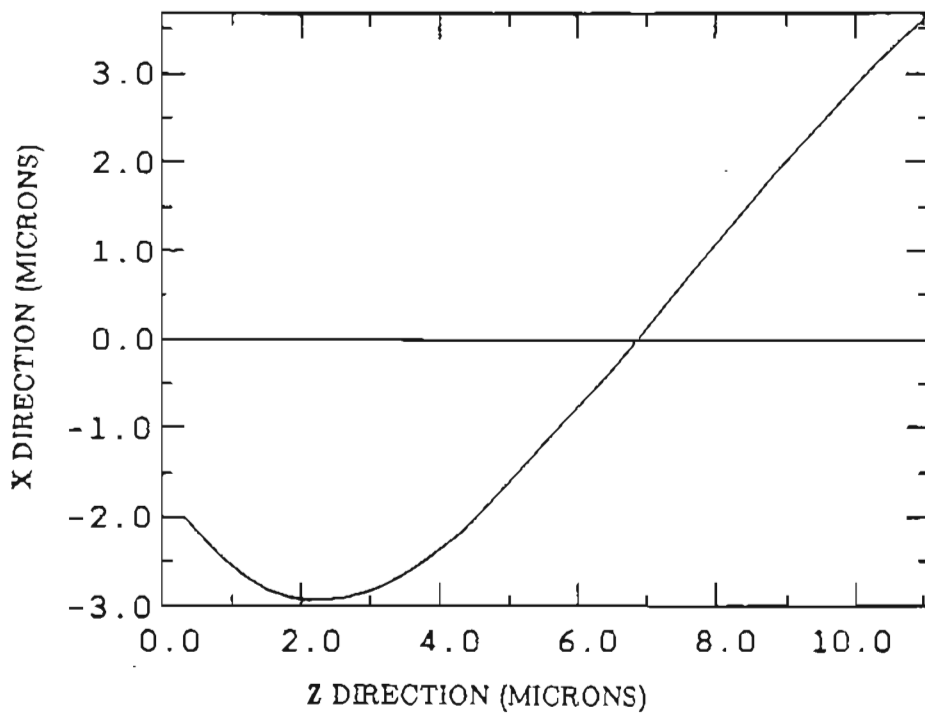


Figure 5.4b Schematic of the parabolic turning obtained by fitting a curve to points measured from the SEM picture.

## 6. RESULTS

In this chapter experimental and theoretical results will be presented. As a check for the the program 'intrfcfld.f', which calculates the field at the waveguide-air interface, the results from this program were compared with those illustrated in the paper by Davies and Walpole for a PbSnTe laser diode. The plot for the electric field at the interface is shown in Figure 6.1a and that illustrated in Davies and Walpole's paper in Figure 6.1b. It can be seen that the the results from the paper match very well with the computer simulated electric field amplitude. The modal reflection coefficient at the interface,  $R$ , was also calculated. The calculated value( = 0.69), agrees with that calculated from data given in Figure 3 in the paper. In this thesis, the farfield pattern for two surface emitters, one with a straight 45° turning mirror and the other with a parabolic turning mirror were modeled as explained in Chapter 4, section 4.5.

The computer code worked as follows: First, the field amplitude at the laser output facet was calculated using the program 'intrfcfld.f' and parameters relevant to the particular laser diode. Then the complex field amplitude obtained from 'intrfcfld.f' was used in the program '2dmirr.f' which calculated the field at the turning mirror. Since the shape of the turning mirror was incorporated in the program, it was necessary to fit an equation to the mirror. Equation 4.31 was used in the program to calculate the field at the turning mir-

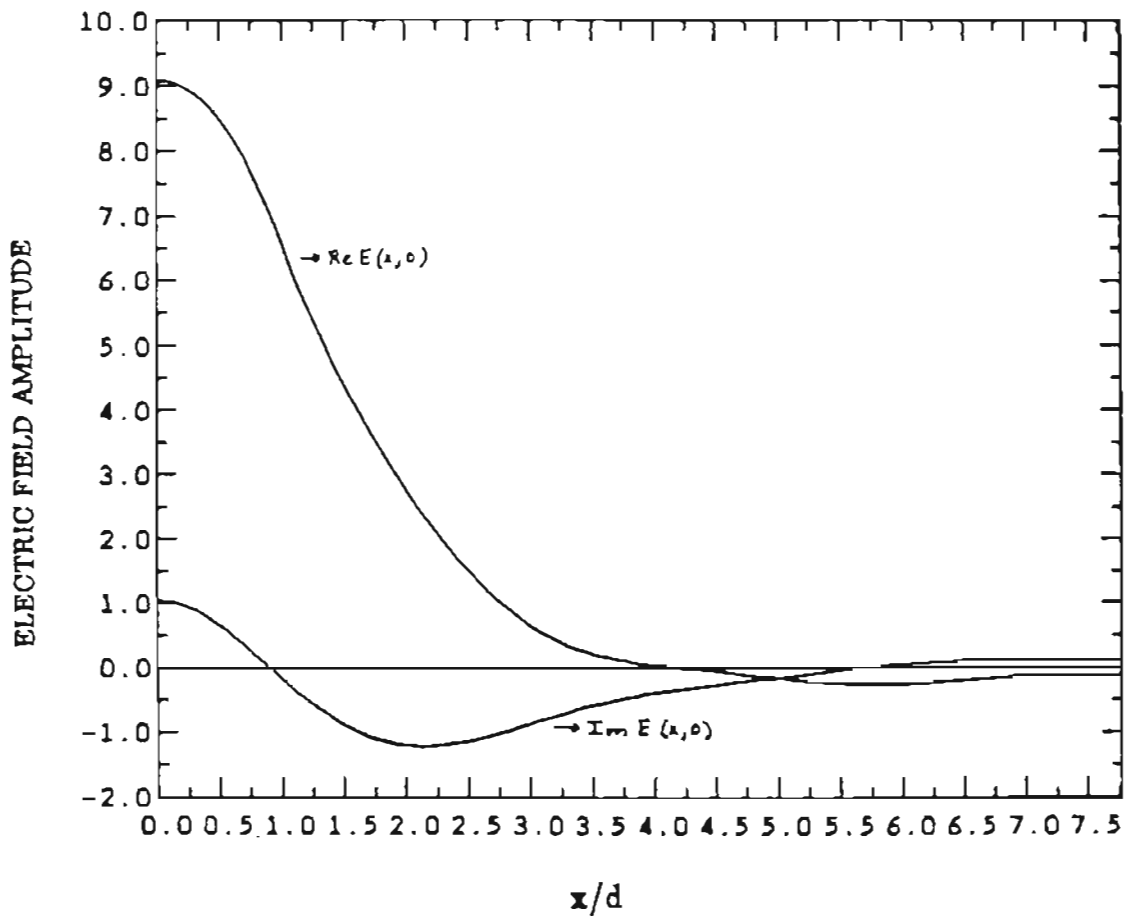


Figure 6.1a Theoretical electric field pattern at the waveguide-air interface calculated using the theory by Davies and Walpole. The parameters used are:  $n_1 = 6.71$ ,  $n_2 = 5.91$ ,  $2d = 1.26 \mu m$ , and  $\lambda = 10 \mu m$ .  $ReE(x,0)$  is the real part of the field and  $ImE(x,0)$  is the imaginary part of the field.

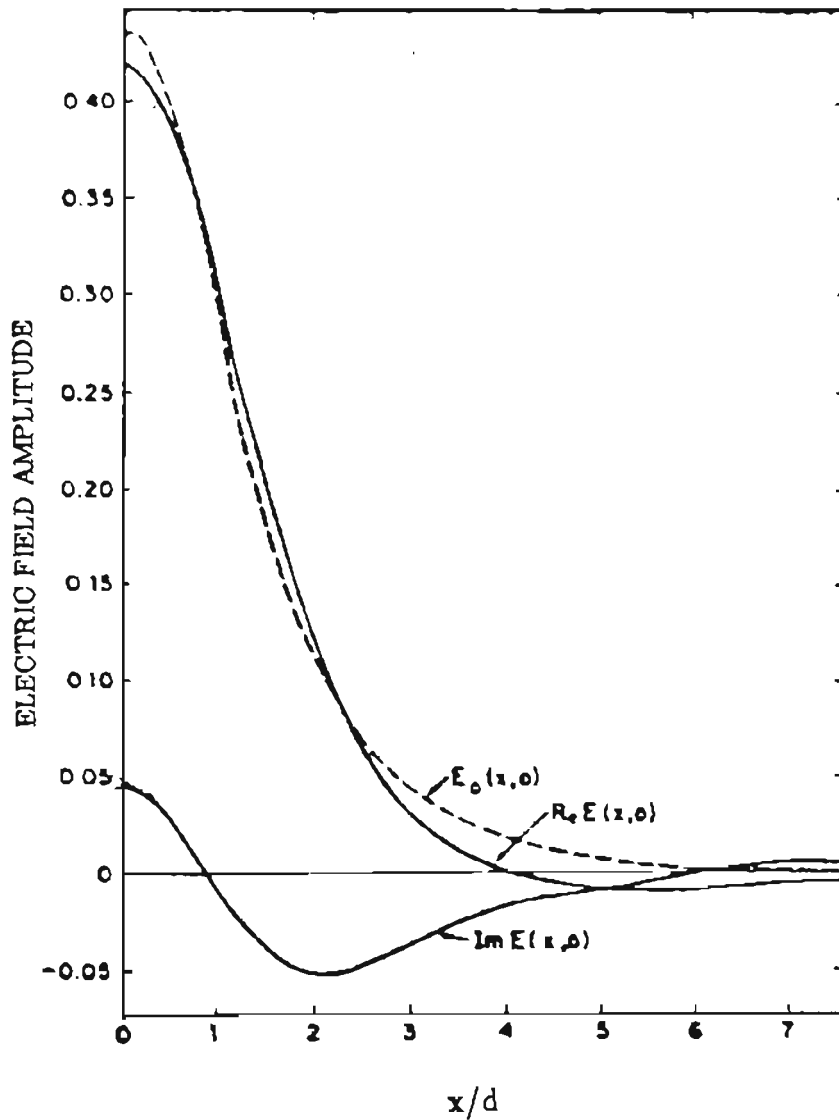


Figure 6.1b Theoretical electric field pattern at the waveguide-air interface illustrated in the paper by Davies and Walpole. The parameters used are:  $n_1 = 6.71$ ,  $n_2 = 5.91$ ,  $2d = 1.26 \mu m$ , and  $\lambda = 10 \mu m$ .  $ReE(x,0)$  is the real part of the field and  $ImE(x,0)$  is the imaginary part of the field.  $E_0(x,0)$  is the guided wave. [11]

ror. Next, equation 4.31 and the complex field amplitude from '2dmirr.f' were used in the program '2daper.f' to calculate the field at the aperture *AGB* shown in Figure 4.10. To calculate the field at the aperture due to the parabolic mirror, the parabolic mirror was divided into small sections such that each small section could be assumed to be a straight aperture and the same Green's function as discussed in Chapter 4 could be used. Hence, the program can calculate the field at the aperture due to any curved surface if the surface is divided into sections small enough that they could be considered as straight lines. Then, the program '2dffld.f' calculated the farfield at the plane P in Figure 4.10 using,

- 1.) the field at aperture *AGB* and
- 2.) the field at the laser output facet *AOC*.

Finally, the total farfield was calculated using the program 'add.f' which added the two contributions mentioned above coherently.

Experimental data for a 45° turning mirror, was measured from a surface-emitter which was micromachined at OGC and the results published by Liau and Walpole<sup>7</sup> were used as a comparison for the case of the surface-emitter with a parabolic turning mirror. The specifications for the two lasers are given in Chapter 5, section 5.3.

## **6.1 Results For A Surface-Emitter With A Parabolic Turning Mirror**

The computer simulated farfield pattern of the surface emitter with a parabolic turning mirror is shown in Figure 6.2 and those experimentally obtained

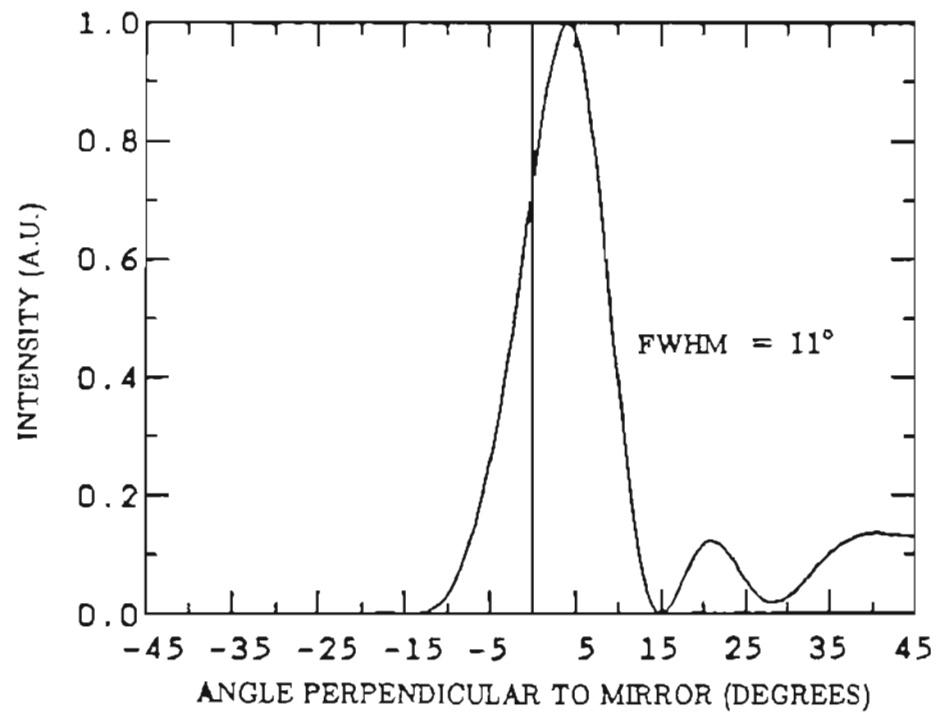


Figure 6.2 Computer simulated farfield pattern from a surface emitter with parabolic turning mirror.

by Liao and Walpole, are shown in Figures 6.3a and 6.3b. These two patterns were obtained from two wafers and are different since the shape of the turning mirror differed slightly from wafer to wafer mostly due to the variations in the thickness of the cap region. The full width at half maximum (FWHM) obtained theoretically is within 10% of the experimentally observed FWHM of  $12^\circ$ . All three farfield patterns have two lobes in the positive angle direction. The first one can be identified as the diffraction lobe. The height of the diffraction lobe relative to that of central maximum was found to be dependent on the reflectivity of the turning mirror surface. The reflectivity was assumed to be 100% in the computer program since the surface of the turning mirror was coated with gold. Reducing the reflectivity reduced the height of the diffraction lobe relative to the central lobe. In the paper by Liao and Walpole<sup>7</sup>, the lobe on the far right was attributed to the light bypassing the turning mirror. As seen in Figure 6.4, the lobe on the right of zero degrees is very small since the contribution of the light bypassing the turning mirror has not been included. This proves that the explanation for the existence of this lobe given in the paper is correct.

## 6.2 Results For A Surface-Emitter With A $45^\circ$ Turning Mirror

Figure 6.5 illustrates the modeled pattern and Figures 6.6a and 6.6b the measured farfield patterns from a surface emitter with a nominally  $45^\circ$  straight turning mirror. Since no cross-section of the turning mirror was obtained, the exact angle could not be determined. The measured patterns are from two different lasers but the laser material is the same. All three patterns show

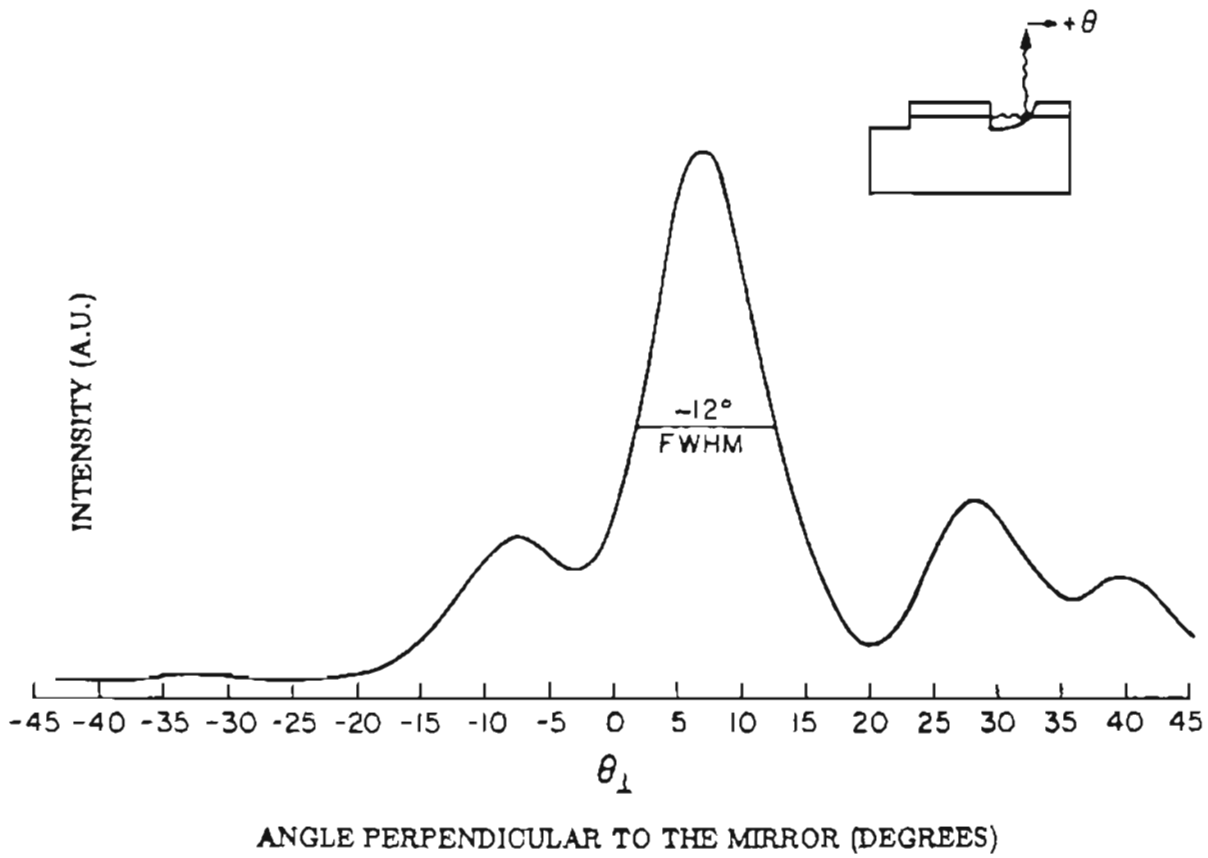


Figure 6.3a Measured farfield pattern from a surface emitter with a parabolic turning mirror (wafer 685). [courtesy Dr. Walpole]

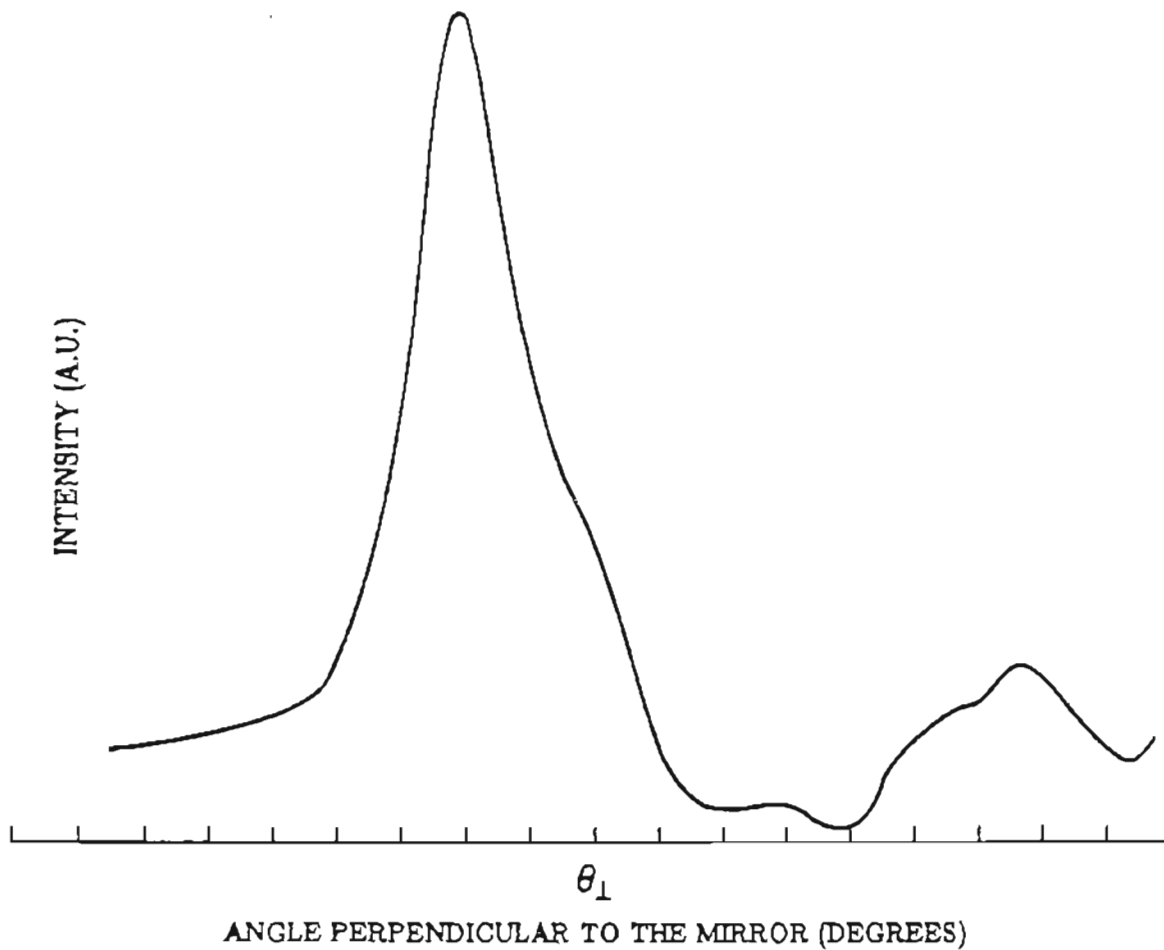


Figure 6.3b Measured farfield pattern from a surface emitter with a parabolic turning mirror (wafer 792). [courtesy Dr. Walpole]

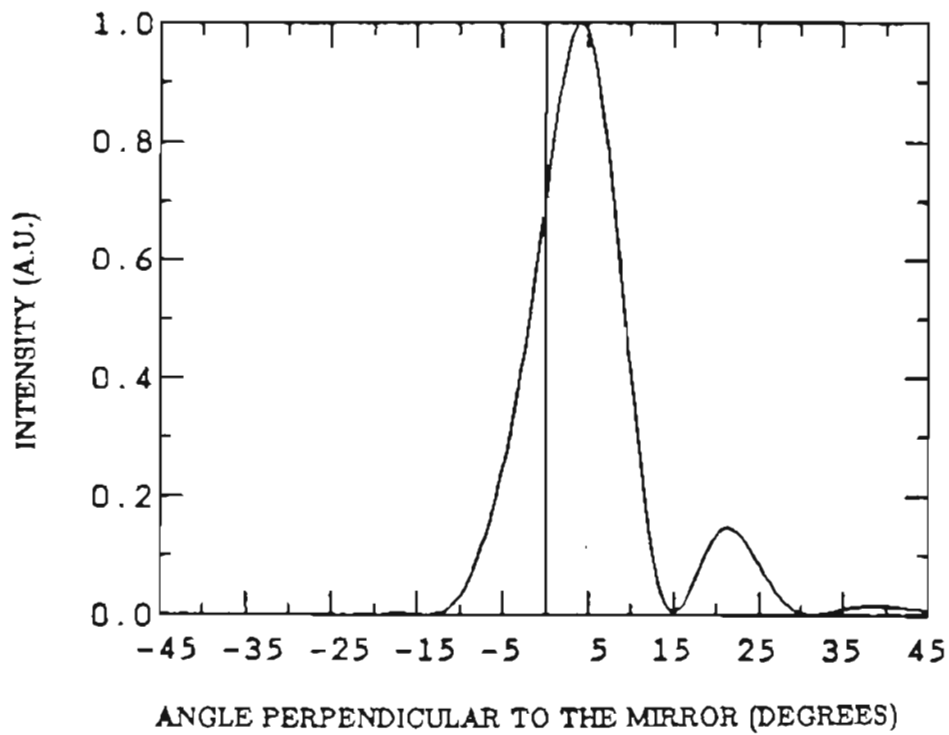


Figure 6.4 Computer simulated farfield pattern from a surface-emitter with a parabolic turning mirror. The farfield pattern does not include the contribution of the light that bypasses the turning mirror.

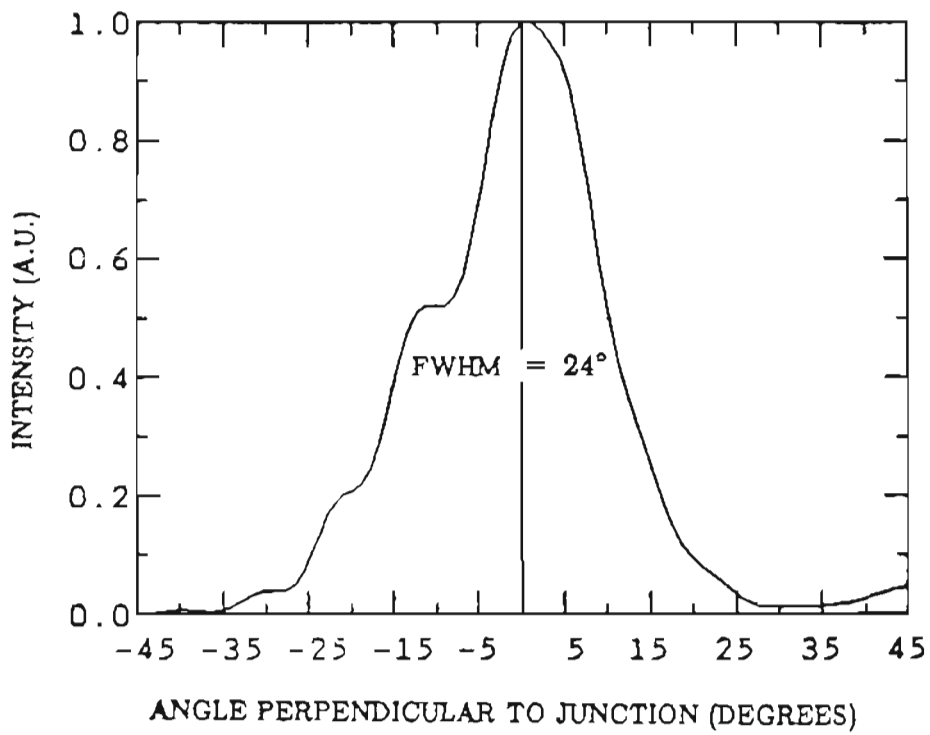


Figure 6.5 Computer simulated farfield pattern for a surface emitter with a 45° straight turning mirror.

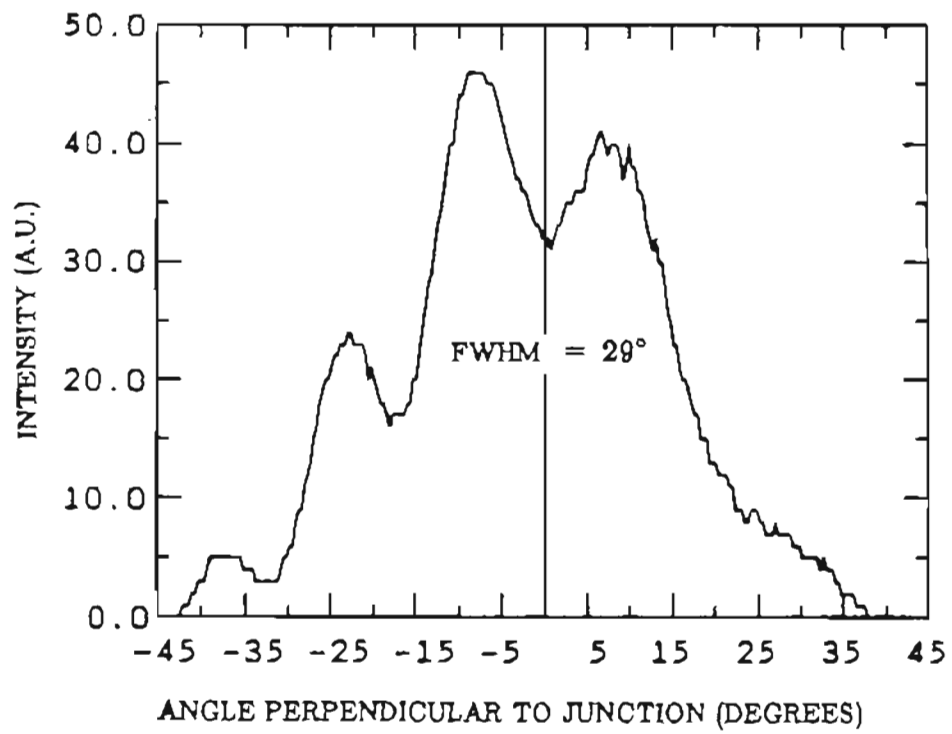


Figure 6.6a Measured farfield pattern for a surface emitter with a 45° straight turning mirror (SEPADL-20).

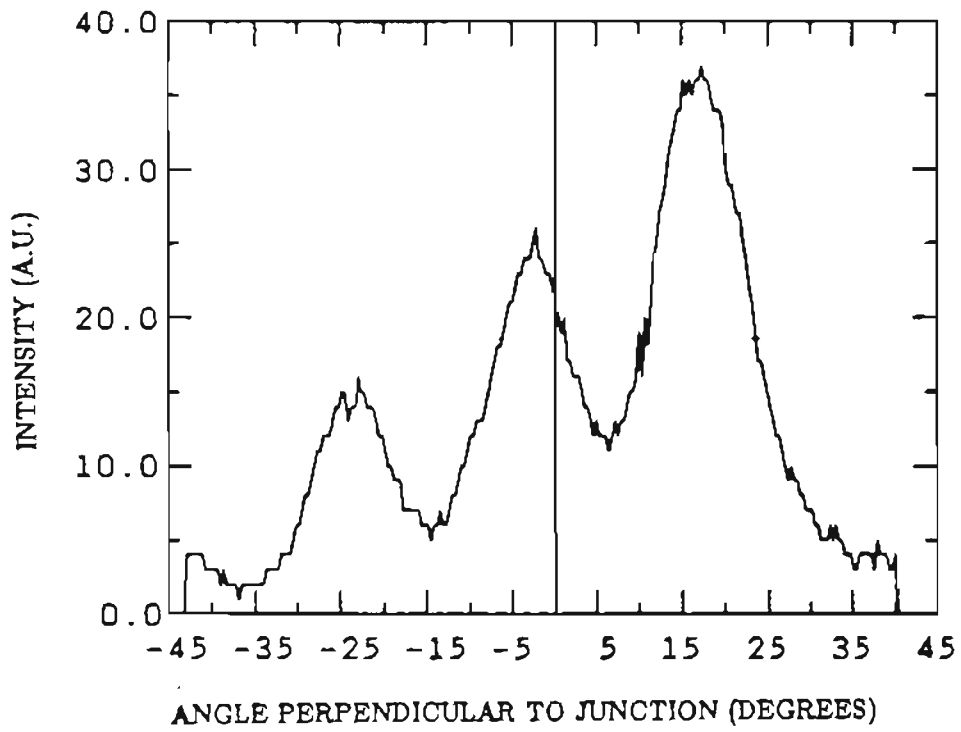


Figure 6.6b Measured farfield pattern for a surface emitter with a 45° straight turning mirror (SEPADL-22).

modulations on the left of zero degrees, which is the position of the normal to the diode epi-layers. But the modulations are much larger in the case of the measured patterns. The SEM pictures of these two turning mirrors showed rough surfaces for the turning mirrors and also some redeposited material due to micromachining. This would change the shape of the turning from ideal  $45^\circ$  straight mirror and the farfield pattern from the ideal farfield pattern seen in Figure 6.5. The FWHM in the Figures 6.6a and 6.6b is  $29^\circ$ s and in the modeled farfield pattern it is  $24^\circ$ s. This could be because the aperture width, ie. the width of *AGB* in Figure 4.10 is smaller for the micromachined mirror compared to the width considered for computer modeling. Also the field at the turning mirror is actually the interference pattern of the ten emitters instead of one emitter. A cross-section of the turning mirror would clearly show the actual shape of the turning mirror and modeling could be done more accurately. The next chapter presents conclusions.

## 7. CONCLUSIONS

In this thesis, the farfield pattern of a surface emitting diode laser with a turning mirror was modeled and compared with the experimental results. The experimental set-up designed for this work can correctly measure the farfield pattern of a surface-emitting diode laser. Two shapes of turning mirrors were considered for computer simulation. A straight  $45^\circ$  turning mirror and a parabolic turning mirror. Instead of assuming a Gaussian beam shape at the waveguide-air interface, a rigorous theoretical analysis of the boundary conditions by Davies and Walpole was used to determine field amplitude at the interface. From the results illustrated in the previous chapter, it is clear that using this rigorous treatment one can predict the ideal farfield pattern as in the case of  $45^\circ$  turning mirror, or model the farfield pattern from the turning mirror cross-section as in the case of parabolic turning mirror. The computer simulated result for the farfield pattern of a surface-emitter with a  $45^\circ$  mirror shown in Figure 6.5 has FWHM of  $24^\circ$  whereas the FWHM of a surface-emitter with a parabolic turning mirror shown in Figure 6.2 is only  $11^\circ$ . Therefore, the computer simulation results indicate clearly that a parabolic turning mirror gives a smaller beam divergence. Also, the computer code written for this thesis is quite versatile and can model the farfield patterns of several different shapes of turning mirrors by changing the shape of the mirror and other relevant parameters as explained at the beginning of Chapter 6. The theoretically obtained

farfields did not exactly match the measured farfields mainly due to the lack of availability of a good cross-section of the turning mirror.

Further improvements and additions can also be made to the present work. The nearfield, that is the field at aperture *AGB* in Figure 4.10 can be easily determined by calculating the field at aperture *AGB* due to the field at the laser output facet using the program '2dffld.f' and adding it to the field at the aperture due to the turning mirror. This result can then be compared to the measured nearfield pattern. There are also multiple reflections, ie. light reflects off the turning mirror to the laser output facet where it reflects again to contribute to the farfield pattern. Although this contribution will not be large it might give better results. The work done here is just a beginning of the final goal of modeling the farfield of a two-dimensional surface-emitting diode laser array. Hence the existing code could be extended to include interference theory to model the farfield pattern of a two-dimensional array of surface-emitting diode lasers.

## References

1. M. Sakamoto, G. L. Harnagel, D. F. Welch, C. R. Lennon, W. Streifer, H. Kung, D. R. Scifres, "Continuous-Wave 12.5W Monolithic Laser Diode Arrays," *Proc. CLEO'88*, p. 168, April 1988. WB2
2. J. C. McShea, J. C. Petheram, A. Rosenberg, "High-Power High-Efficiency 2-D Laser Diode Arrays for Pumping Solid-State Lasers," *Proc. CLEO'88*, p. 172, April 1988. WB5
3. F. Koyama, K. Tomomatsu, K. Iga, "GaAs/GaAlAs CBH Surface-Emitting Laser Grown by MOCVD and a 2-D Locked Laser Array," *Proc. CLEO'88*, p. 256, April 1988. WO5
4. N. W. Carlson, G. A. Evans, J. M. Hammer, M. Lurie, L. A. Carr, F. Z. Hawrylo, E. A. James, C. J. Kaiser, J. B. Kirk, W. F. Reichert, D. A. Truxal, "High Power Seven-Element Grating Surface-Emitting Diode Laser Array With 0.012 degree Far-Field Angle," *Appl. Phys. Lett.*, vol. 52(12), pp. 939-941, March 1988.
5. J. M. Hammer, N. W. Carlson, G. A. Evans, M. Lurie, S. L. Palfrey, C. J. Kaiser, M. G. Harvey, E. A. James, J. B. Kirk, F. R. Elia, "Phase-Locked Operation of Coupled Pairs of Grating-Surface-Emitting Diode Lasers," *Appl. Phys. Lett.*, vol. 50(11), pp. 659-661, March 1987.
6. T. H. Windhorn and W. D. Goodhue, "Monolithic GaAs/AlGaAs Diode Laser Deflector Devices for Light Emission Normal to The Surface," *Appl. Phys. Lett.*, vol. 48(24), pp. 1675-1677, June 1986.
7. Z. L. Liao and J. N. Walpole, "Surface-Emitting GaInAsP/InP Laser With Low Threshold Current and High Efficiency," *Appl. Phys. Lett.*, vol. 46(2), pp. 115-117, Jan 1985.
8. R. A. Elliott, R. K. DeFreez, J. Puretz, J. Orloff, G. A. Crow, "Focussed Ion Beam Micromachining of Diode Laser Mirrors," *Proc. of SPIE*, vol. 876, pp. 114-120, Jan. 1988.
9. J. Puretz, R. K. DeFreez, R. A. Elliott, J. Orloff, T. L. Paoli, "330mW Operation of a Surface-Emitting Phase-Locked Array of Diode Lasers," *Electron. Lett.*, vol. 23, No.3, pp. 130-131, Jan. 1987.
10. Conversation between Dr. R. K. DeFreez of the Oregon Graduate Center and Dr. J. N. Walpole of MIT Lincoln Laboratory, at the Topical Meeting on Semiconductor Lasers, on February 10-11 1987, in Albuquerque, New Mexico.
11. R. W. Davies and J. N. Walpole, "Output Coupling for Closely Confined PbSnTe Double-Heterostructure Lasers," *IEEE J. Quantum Electron.*, vol. QE-12, No.5, pp. 291-303, May 1976.
12. J. I. Pankove, *Optical Processes in Semiconductors*, Dover Publications, Inc., New York, 1975. Chapter 9,10
13. N. Holonyak Jr., R. M. Kolbas, R. D. Dupuis, P. D. Dapkus, "Quantum Well Heterostructure Lasers," *IEEE Journal of Quantum Electronics*, vol. QE-16, No.2, pp. 170-185, Feb 1980.

14. W.T. Tsang, *Semiconductors and Semimetals*, R. Dingle (Ed.) 24, Academic Press Inc., 1987. Chapter 7
15. L. C. Chiu, A. Yariv, "Quantum Well Lasers," *J. Luminescence*, vol. 30, pp. 551-561, Feb. 1985.
16. E. Zielinski, H. Schweizer, S. Hausser, R. Stuber, M. H. Pilkun, G. Weimann, "Systematics of Laser Operation in GaAs/AlGaAs Multiquantum Well Heterostructures," *IEEE J. of Quantum Electron.*, vol. QE-23, No. 6, pp. 969-976, June 1987.
17. D. R. Scifres, W. Streifer, R. D. Burnham, "High-Power Coupled-Multiple-Stripe Phase-Locked Injection Laser," *Appl. Phys. Lett.*, vol. 34(4), pp. 259-261, Feb. 1979.
18. D. R. Scifres, R. D. Burnham, and W. Streifer, "Phase Locked Semiconductor Laser Array," *Appl. Phys. Lett.*, vol. 33(12), pp. 1015-1017, Dec. 1978.
19. D. R. Scifres, R. D. Burnham, W. Striefer, "High Power Coupled Multiple Stripe Quantum Well Injection Lasers," *Appl. Phys. Lett.*, vol. 41, No. 2, pp. 118-120, July 1982.
20. D. F. Welch, D. Scifres, P. Cross, H. Kung, "High-Power (575mw) Single Lobed Emission From Phased Array Laser," *Electron. Lett.*, vol. 21, No. 14, pp. 603-604, July 1985.
21. E. Kapon, C. P. Lindsey, J. S. Smith, S. Margalit, A. Yariv, "Inverted-V Chirped Phased Arrays Of Gain-Guided GaAs/GaAlAs Diode Lasers," *Appl. Phys. Lett.*, vol. 45, pp. 1257-1259, Dec. 1984.
22. D. Botez and J. C. Connolly, "High-Power Phase Locked Arrays of Index-Guided Diode Lasers," *Appl. Phys. Lett.*, vol. 43, No. 12, pp. 1096-1098, Dec 1983.
23. D. F. Welch, W. Streifer, D. R. Scifres, "High-Power Index-Guided Lasers Emitting in a Single Transverse Mode," *Proc. CLEO'88*, p. 172, April 1988. WB4
24. D. F. Welch, P. S. Cross, D. R. Scifres, W. Striefer, R. D. Burnham, "High-Power (cw) In-Phase Locked "Y" Coupled Lasers," *Appl. Phys. Lett.*, vol. 49(24), pp. 1632-1634, Dec. 1986.
25. J. P. van der Ziel, H. Temkin, A. Logan, R. D. Dupuis, "High Power Picosecond Pulse Generation in GaAs Multiquantum Well Phase-Locked Laser Arrays Using Pulsed Current Injection," *IEEE J. of Quantum Electron.*, vol. QE-20, No. 11, pp. 1236-1242, Nov. 1984.
26. D. Scifres, R. D. Burnham, W. Streifer, M. Bernstein, "Lateral Beam Collimation Of Phased Array Semiconductor Laser," *Appl. Phys. Lett.*, vol. 41(7), pp. 614-616, October 1982.
27. J. E. Ripper and T. L. Paoli, "Optical Coupling of Adjacent Stripe-Geometry Junction Lasers," *Appl. Phys. Lett.*, vol. 17, No. 9, pp. 371-373, Nov. 1970.
28. J. K. Butler, D. E. Ackley, D. Botez, "Coupled-mode Analysis of Phased-Locked Injection Laser Arrays," *Appl. Phys. Lett.*, vol. 44, No. 3, pp. 293-

- 295, Feb. 1984.
29. E. Kapon, J. Katz, A. Yariv, "Supermode Analysis Of Phase-Locked Arrays Of Semiconductor Lasers," *Opt. Lett.*, vol. 10, pp. 125-127, April 1984.
  30. M. Ogura, S. C. Wang, J. J. Yang, "Surface-Emitting Laser Diode With Vertical GaAs/GaAlAs Quarter-Wavelength Multilayers And Lateral Buried Heterostructure," *Appl. Phys. Lett.*, vol. 51(21), pp. 1655-1657, Nov. 1987.
  31. A. Ibaraki, S. Ishikawa, S. Ohkouchi, K. Iga, "Pulsed Oscillation of GaAlAs/GaAs Surface-Emitting Injection Laser," *Electron. Lett.*, vol. 20, pp. 420-422, 1984.
  32. K. Iga, S. Ishikawa, S. Ohkouchi, T. Nishimura, "Room Temperature Pulsed Oscillation Of GaAlAs/GaAs Surface Emitting Junction Laser," *IEEE J. of Quantum Electron.*, vol. QE-21, No.6, pp. 663-668, June 1985.
  33. K. Iga, S. Kinoshita, F. Koyama, "Microcavity GaAlAs/GaAs Surface-Emitting Laser With  $I_{th} = 6\text{mA}$ ," *Electron. Lett.*, vol. 23, No.3, p. 134, Jan. 1987.
  34. J. J. Yang, M. Jansen, M. Sergeant, "Surface-Emitting GaAlAs/GaAs Laser with Etched Mirrors.," *Electron. Lett.*, vol. 22(8), pp. 438-439, April 1986.
  35. T. Yuasa, N. Hamao, M. Sugimoto, N. Takado, M. Ueno, H. Iwata, Y. Tashiro, K. Onabe, K. Asakawa, "Surface-Emitting GaAs/AlGaAs Multi-quantum Well Lasers With Optical Bistability," *Proc. CLEO'88*, p. 258, April 1988. Wo6
  36. J. N. Walpole, "R&D On Surface-Emitting Diode Lasers," *Laser Focus*, pp. 66-74, Sept. 1987.
  37. R. D. Burnham, D. R. Scifres, W. Streifer, "Single-Heterostructure Distributed Feedback GaAs-Diode Lasers," *IEEE J. Quantum Electron.*, vol. QE-11, p. 439, 1975.
  38. P. Zory, L. D. Comerford, "Grating-Coupled Double-Heterostructure AlGaAs Diode Lasers," *IEEE J. Quantum Electron.*, vol. QE-11, p. 451, 1975.
  39. G. A. Evans, J. M. Hammer, N. W. Carlson, F. R. Elia, E. A. James, J. B. Kirk, "Surface-Emitting Second Order Distributed Bragg Reflector Laser With Dynamic Wavelength Stabilization And Far-Field Angle of 0.25 Degree," *Appl. Phys. Lett.*, vol. 48, p. 314, 1986.
  40. D. F. Welch, M. Cardinal, W. Streifer, D. R. Scifres, P. S. Cross, "High-Brightness High-Efficiency Single Quantum Well Laser Diode Array," *Electron. Lett.*, vol. 23, pp. 1240-1241, 1987.
  41. J. R. Shealy, "Optimizing the Performance of AlGaAs Graded Index Separate Confining Heterostructure Quantum Well Lasers," *Appl. Phys. Lett.*, vol. 50, pp. 1634-1636, 1987.
  42. J. N. Walpole and Z. L. Liao, "Monolithic Two-Dimensional Arrays of High-Power Surface-Emitting Diode Laser," *Appl. Phys. Lett.*, vol. 48(24), pp. 1636-1638, June 1986.

43. Z. L. Liao and J. N. Walpole, "Large Monolithic Two-Dimensional Arrays of GaInAsP/InP Surface Emitting Lasers," *Appl. Phys. Lett.*, vol. 50, p. 528, 1987.
44. S. Peled, "Near and Far-Field Characterization of Diode Lasers," *Appl. Optics*, vol. 19(2), pp. 324-328, Jan 1980.
45. G. H. B. Thompson, *Physics of Semiconductor Laser Devices*, John Wiley & Sons, 1980.
46. H. Kressel and J. K. Butler, *Semiconductor Lasers and Heterojunction LEDs*, Academic Press, NY, 1977.
47. T. Ikegami, "Reflectivity of Mode at Facet and Oscillation Mode in Double-Heterostructure Injection Lasers," *IEEE J. Quantum Electron.*, vol. QE-8, No. 6, pp. 470-476, June 1972.
48. F. R. Nash, "Mode Guidance Parallel to The Junction Plane of Double-Heterostructure GaAs Lasers," *J. Appl. Phys.*, vol. 44, pp. 4496-4707, 1973.
49. G. H. B. Thompson, "A Theory for Filamentation in Semiconductor Lasers Including The Effect of Dielectric Constant on Injected Carrier Density," *Opto-Electron.*, vol. 4, pp. 257-310, 1972.
50. D. D. Cook and F. R. Nash, "Gain-Induced Guiding and Astigmatic Output Beam of GaAs Lasers," *J. Appl. Phys.*, vol. 46, pp. 1660-1672, 1975.
51. T. L. Paoli, "Waveguiding in Stripe-Geometry Junction Laser," *IEEE J. Quantum Electron.*, vol. QE-13, pp. 662-668, 1977.
52. W. Streifer, R. D. Burnham, D. R. Scifres, "Symmetrical and Asymmetrical Waveguiding in Very Narrow Conducting Stripe Laser," *IEEE J. Quantum Electron.*, vol. QE-15, No. 3, pp. 136-141, March 1979.
53. A. Yariv, *Optical Electronics*, Third edition, p. 112, Holt-Saunders, 1985. chapter 4
54. M. Born and E. Wolf, *Principles of Optics*, p. 377, Pergamon Press, New York, 1980. Sixth Edition
55. T. E. Rozzi, "Rigorous Analysis of The Step Discontinuities in a Planar Dielectric Waveguide," *IEEE Trans. Microwave Theory Tech.*, vol. MTT-26, No.10, pp. 738-746, 1978.
56. T. E. Rozzi and G. H. int' Veld, "Variational Treatment of the Diffraction at the Facet of d.h Laser and of Dielectric Millimeter Wave Antennas," *IEEE Trans. Microwave Theory Tech.*, vol. MTT-28, No.2, pp. 61-73, Feb 1980.
57. J. K. Butler and J. Zoroofchi, "Radiation Fields of GaAs-(AlGa)As Injection Lasers," *IEEE Journal Quantum Electron.*, vol. QE-10, No. 10, pp. 809-815, Oct. 1974.
58. J. Poretz, J. Orloff, L. Swanson, "An Application of Focused Ion Beams To Electron Beam Testing Of Integrated Circuits," *Proc. SPIE*, vol. 471, pp. 38-46, 1984.
59. J. Poretz, R. K DeFreez, R. A. Elliott, J. Orloff, "Focused-Ion-Beam Micromachined AlGaAs Semiconductor Laser Mirror," *Electron. Lett.*, vol.

- 22, No.13, p. 700, 19th June 1986.
60. R. K. DeFreez, J. Poretz, R. A. Elliott, J. Orloff, L. W. Swanson, *Electron. Lett.*, vol. 22, p. 919, 1986.
  61. G. Crow, J. Poretz, J. Orloff, R. K. DeFreez, R. A. Elliott, "The Use Of Vector Scanning For Producing Arbitrary Surface Contours With A Focused Ion Beam," *J. Vac. Sci. Technol. B*, 1988. To be published in Aug/Sept issue
  62. R. K. DeFreez, J. Poretz, J. Orloff, R. A. Elliott, H. Namba, E. Omura, H. Namizaki, "Operating Characteristics And Elevated Temperature Lifetests Of Focussed Ion Beam Micromachined Transverse Junction Stripe Lasers," *Appl. Phys. Lett.*, Sept. 26 1988. To be published
  63. B. I. Miller, K. Iga, "GaInAsP/InP Stripe Lasers With Etched Mirrors Fabricated By A Wet Chemical Etch," *Appl. Phys. Lett.*, vol. 37, pp. 339-341, 1980.
  64. R. R. Craig, L. W. Casperson, O. M. Staffsudd, J. J. Yang, G. A. Evans, R. A. Davidheiser, "Etched-Mirror Unstable-Resonator Semiconductor Lasers," *Electron. Lett.*, vol. 21, pp. 62-63, 1985.
  65. N. Bouadma, J. Riou, and A. Kampfer, "Low Threshold GaAs/GaAlAs BH Lasers With Ion-Beam-Etched Mirrors," *Electron. Lett.*, vol. 21, pp. 566-568, June 1985.
  66. N. Boudma, F. Brillouet, J. Riou, and L. Dugond, *Proc. 9th IEEE International Laser Conference*, Rio de Janeiro, Brazil, 1984( IEEE 1984).
  67. L. A. Coldren, K. Iga, B. I. Miller, and J. A. Rentschler, "GaInAsP/InP Stripe-Geometry Laser With Reactive-Ion Etched Facet," *Appl. Phys. Lett.*, vol. 37, pp. 681-683, Oct. 1980.
  68. M. Mannoh, T. Yusa, K. Asakawa, K. Shinozaki, M. Ishii, "Low-Threshold MBE GaAs/AlGaAs Quantum Well Lasers With Dry Etched Mirrors," *Electron. Lett.*, vol. 21, pp. 769-770, 1985.
  69. O. Wada, Y. Shigenobu, and T. Sakurai, *IEEE J. Quantum Electron.*, vol. QE-20, p. 126, 1984.
  70. Z. L. Liao, J. N. Walpole, D. Z. Tsang, "Low Threshold GaInAsP/InP Buried-Heterostructure Lasers With Chemically Etched And Mass-Transported Mirror," *Appl. Phys. Lett.*, vol. 44, pp. 945-947, 1984.
  71. L. R. Harriott, R. E. Scotti, K. D. Kummings, A. F. Ambrose , "Micromachining of Integrated Optical Structures," *Appl. Phys. Lett.*, vol. 48(25), pp. 1704-1706, 23rd June 1986.
  72. J. Orloff, L. W. Swanson, "Optical Column Design With Liquid Metal Ion Sources," *J. Vac. Sci. Technol.*, vol. 119, p. 1149, 1981.
  73. H. Yamaguchi, A. Shimase, S. Hiraichi, T. Miyauchi , "Characteristics of Silicon Removal by Fine Focused Gallium Ion Beam," *J. Vac. Sci. Technol.*, vol. B3(1), pp. 71-74, Jan/Feb 1985.
  74. H. C. Casey Jr., D. D. Sell, M. B. Panish, "Refractive Index Of AlGaAs Between 1.2 And 1.8 eV," *Appl. Phys. Lett.*, vol. 24, No. 2, pp. 63-65, Jan 1974.

75. T. P. Pearsall, *GaInAsP Alloy Semiconductors*, p. Chapter 14, page 362, John Wiley & Sons, 1982.
76. D. Marcuse, *Light Transmission Optics*, Von Nostrand Reinhold Co., New York, 1972. Chapter 8

## APPENDIX A

This appendix gives the details of the theoretical solution of the problem of determining field at the waveguide-air interface.

### A1.1 Equations For Bound and Radiation Mode Fields

As derived by Marcuse,<sup>76</sup> the expressions for  $E_0(x)$ , the incident bound mode field and  $E_\gamma(x)$ , the radiation mode field are given as follows:

$$E_0 = \left[ \frac{2\mu_0\omega}{\beta_0(d + \gamma_0^{-1})} \right]^{1/2} \begin{cases} \cos(\kappa_0 x) & |x| < d \\ \cos(\kappa_0 d) e^{d\gamma_0} e^{-|x|\gamma_0} & |x| > d \end{cases} \quad (A1)$$

Here,  $\mu_0\omega$  is a constant,  $d$  is the half thickness of the active layer and  $\kappa_0$  is the lowest order eigenvalue solution of

$$(\kappa_0 d)^2 [1 + \tan^2(\kappa_0 d)] = (k_0 d)^2 (n_1^2 - n_2^2) \quad (A2)$$

where

$$k_0 = \sqrt{\mu_0\epsilon_0\omega^2} = \frac{2\pi}{\lambda} \quad (A3)$$

is the free-space wave vector. The coefficient  $\beta_0$  and  $\gamma_0$  are then determined from

$$(\beta_0 d)^2 = (k_0 d)^2 n_1^2 - (\kappa_0 d)^2 \quad (A4)$$

$$(\gamma_0 d)^2 = \kappa_0 d \tan(\kappa_0 d) \quad (\text{A5})$$

For even parity TE radiation modes we have

$$\begin{aligned} E_\gamma(x) &= A \cos(\kappa x) \quad \text{for } |x| < d \\ &= A \left[ \cos \kappa d \cos \gamma d + \frac{\kappa}{\gamma} \sin \kappa d \sin \gamma d \right] \cos \gamma x \\ &+ A \left\{ \cos \kappa d \sin \gamma d \right. \\ &\left. - \frac{\kappa}{\gamma} \sin \kappa d \cos \gamma d \right\} \sin \gamma |x| \quad \text{for } |x| > d \end{aligned} \quad (\text{A6.1})$$

with

$$A = \left[ \frac{2\mu_0 \omega}{\pi |\beta_\gamma| \left( \cos^2 \kappa d + \frac{\kappa^2}{\gamma^2} \sin^2 \kappa d \right)} \right]^{1/2} \quad (\text{A6.2})$$

Here  $\gamma$  is an arbitrary (continuum) wave vector in the range  $0 \leq \gamma \leq \infty$ , and  $\kappa$

and  $\beta_\gamma$  are determined from

$$(\kappa d)^2 = (\gamma d)^2 + (k_0 d)^2 (n_1^2 - n_2^2) \quad (\text{A7})$$

$$(\beta_\gamma d) = \sqrt{(k_0 d)^2 n_2^2 - (\gamma d)^2} \quad (\text{A8})$$

In (A8)  $\beta_\gamma$  is imaginary in the case of evanescent modes i.e. when  $\gamma > k_0 n_2$ .

Finally,  $\beta(\sigma)$  is given by

$$\beta(\sigma) d = \sqrt{(k_0 d)^2 - (\sigma d)^2} \quad (\text{A9})$$

For  $k_0 < \sigma$ ,  $\beta(\sigma)$  is imaginary and represents evanescent waves.

## A1.2 Equations For Coefficients $R$ and $g(\gamma)$

The coefficients  $R$  and  $g(\gamma)$  are determined from equation (4.22) by multiplying (4.22) by  $E_0(x)$  or  $E_{\gamma'}(x)$ , where  $\gamma'$  is such that,

$$\int_{-\infty}^{\infty} E_{\gamma}(x)E_{\gamma'}(x)dx = 2\mu_0 \frac{\omega}{|\beta_{\gamma}|} \delta(\gamma - \gamma'). \quad (\text{A10})$$

Integrating on x and using orthonormality relations for the two fields. The result is

$$R = \frac{1 - F_0 - \int_0^{\infty} d\gamma g(\gamma)F(\gamma)}{1 + F_0} \quad (\text{A11})$$

where  $g(\gamma)$  satisfies the Fredholm integral equation given by

$$g(\gamma) = \frac{|\beta_{\gamma}|}{\beta_{\gamma}} \left[ \phi(\gamma) + \int_0^{\infty} d\gamma' K(\gamma, \gamma')g(\gamma') \right] \quad (\text{A12})$$

The quantities  $\phi(\gamma)$  and  $K(\gamma, \gamma')$  are given by

$$\phi(\gamma) = \frac{-2F(\gamma)}{1 + F_0} \quad (\text{A13})$$

and

$$K(\gamma, \gamma') = \frac{F(\gamma)F(\gamma')}{1 + F_0} - F(\gamma, \gamma') \quad (\text{A14})$$

where the  $F$ 's are given by

$$F_0 = \frac{\pi}{\mu_0 \omega} \int_{-\infty}^{\infty} d\sigma \beta(\sigma) E_0(\sigma)^2 \quad (\text{A15.1})$$

$$F(\gamma) = \frac{\pi}{\mu_0 \omega} \int_{-\infty}^{\infty} d\sigma \beta(\sigma) E_0(\sigma) E_{\gamma}(\sigma) \quad (\text{A15.2})$$

$$F(\gamma, \gamma') = \frac{\pi}{\mu_0 \omega} \int_{-\infty}^{\infty} d\sigma \beta(\sigma) E_0(\gamma) E_{\gamma'}(\sigma) \quad (\text{A15.3})$$

where  $E_0(\sigma)$  and  $E_{\gamma}(\sigma)$  are the fourier transforms of  $E_0(x)$  and  $E_{\gamma}(x)$  respectively. These are given by

$$E_0(\sigma) = \frac{1}{\pi} \left[ \frac{2\mu_0 \omega}{\beta_0(d + \gamma_0^{-1})} \right]^{1/2} \left( \frac{\gamma_0^2 + \kappa_0^2}{\gamma_0^2 + \sigma^2} \right)$$

$$\frac{(\sigma \sin \sigma d \cos \kappa_0 d - \kappa_0 \sin \kappa_0 d \cos \sigma d)}{\sigma^2 - \kappa_0^2} \quad (\text{A16})$$

and

$$\begin{aligned} E_\gamma(\sigma) = & \frac{1}{\pi} \left[ \frac{2\mu_0\omega}{\pi |\beta_\gamma| (\cos^2 \kappa d + \frac{\kappa^2}{\gamma^2} \sin^2 \kappa) d} \right]^{1/2} \\ & \cdot \left\{ \frac{\pi}{2} \delta(\sigma - \gamma) (\cos \kappa d \cos \gamma d + \frac{\kappa}{\gamma} \sin \kappa d \cos \gamma d) \right. \\ & + (\kappa^2 - \gamma^2) \frac{(\sigma \sin \sigma d \cos \kappa d - \kappa \sin \kappa d \cos \sigma d)}{\sigma^2 - \kappa^2} \\ & \left. \cdot Pr \frac{1}{\sigma^2 - \gamma^2} \right\}. \quad (\text{A17}) \end{aligned}$$

These two expressions are not singular at  $\sigma = \kappa_0$  and  $\sigma = \kappa$  since, the limit as  $\sigma$  tends to  $\kappa$  or  $\kappa_0$  is finite and is given by

$$\left[ \frac{1}{2} \left( 1 + \frac{\sin(\kappa/\kappa_0) \cos(\kappa/\kappa_0)}{\kappa/\kappa_0} \right) \right]^2 \quad (\text{A18})$$

The principal value is defined as follows

$$\begin{aligned} \lim_{L \rightarrow \infty} \int_d^L dx e^{ikx} &= ie^{ikd} \left[ Pr \left( \frac{1}{k} \right) - i\pi \delta(k) \right] \\ &= ie^{ikd} \lim_{0^- \rightarrow \infty} \frac{1}{k + i0^+} \quad (\text{A19}) \end{aligned}$$

To solve for reflectivity, one needs to determine  $g(\gamma)$  first. To solve the integral equation A11 for  $\gamma(\gamma)$ , the following transformations are made:

$$\begin{aligned} x_0 &= k_0 d & x &= \kappa d & t &= \gamma d \\ \beta_t &= \beta_\gamma d & y &= \sigma d \end{aligned} \quad (\text{A20})$$

$\beta_\gamma$  is given by equation A8. Also,  $x$  is not the same as  $x$  coordinate of field at the interface. It just represents the product of  $\kappa$  and  $d$ . Then from (A2) and (A7)

$$x_0^2 [1 + \tan^2 x_0] = (x^2 - t^2) = (\kappa_0 d)^2 (n_1^2 - n_2^2). \quad (\text{A21})$$

Further, transforming to barred quantities to isolate the square root singularity due to  $\beta_t$ , the following equations are obtained

$$F_0 = \bar{F}_0 \quad (\text{A22.1})$$

$$F(t) = \frac{d^{1/2}}{|\beta_t|^{1/2}} \bar{F}(t), \quad (\text{A22.2})$$

$$g(t) = \frac{d^{1/2} |\beta_t|^{1/2}}{\beta_t} \bar{g}(t), \quad (\text{A22.3})$$

$$E_t(x) = \frac{d^{1/2} \bar{E}_t(x)}{|\beta_t|^{1/2}} \quad (\text{A22.4})$$

With these transformations one can obtain equations (4.24), (4.25), (4.26), (4.27) and (4.28). Further details for evaluating the expression for  $\bar{g}(t)$  are given in the paper by Davies and Walpole.

## APPENDIX B

### B1.1 Simplifications for Evaluating Equation (4.28)

This appendix gives the details of the computer program called 'intrfcfld.f', which evaluates the field at waveguide-air interface. The first step was to determine  $R$ , the reflectivity at the waveguide-air interface. The principal value integral in equation 4.28 was simplified, as suggested by Dr. R. W. Davies during a discussion on the telephone, as follows

$$\begin{aligned} Pr \left[ \frac{1}{y^2 - t^2} \right] &= Pr \left[ \frac{1}{2t} \left[ \frac{1}{y - t} - \frac{1}{y + t} \right] \right] \\ &= \frac{1}{2t} Pr \left( \frac{1}{y - t} \right) - \frac{1}{2t} Pr \left( \frac{1}{y + t} \right) \end{aligned} \quad (B1)$$

Since  $y$  does not take negative values, the second term has no singularity and can be evaluated easily. The integral with the first term was evaluated by writing it as shown below.

$$Pr \left( \frac{1}{y - t} \right) = \frac{y - t}{(y - t)^2 + (\delta)^2} \quad (B2)$$

where  $\delta$  is a small quantity. The values of the definite integrals for  $R$ ,  $\bar{g}(t)$ ,  $F(t)$  and  $E(x,0)$  were calculated for  $t_1, t_2, t_3$  etc. and the final result was evaluated using the trapezoidal rule. The program was executed for smaller and smaller values of  $\delta$  so as to get better approximation of the principal value. The

other parameter which was changed was the number of intervals for numerical integration. An optimum value for  $\delta$  and  $N$  was found after a number of iterations. It was not necessary to evaluate the integrals up to infinite upper limit since the value of the integrand became negligibly small after a certain value of  $t$ . As a check for the program code written in the way explained above the parameters used by Davies and Walpole<sup>11</sup> in their paper were used to calculate the field at the waveguide-air interface using this program. The results agreed very well with those presented in the paper.

## B2.2 Calculating The Farfield Pattern

The Green's function is chosen such that it is zero on the aperture  $AOC$  and is given by,

$$G(x,0) = \frac{i}{4}(H_0(kr) - H_0(k\bar{r})) \quad (B3)$$

where  $r$  and  $\bar{r}$  are the distances from the aperture to the point at which field is being calculated and its mirror image respectively. Referring to Figure 4.10,  $r = \sqrt{(x - x')^2 + (z)^2}$ . The Hankel function  $H_0(kr)$  can also be written as,

$$H_0^{(1)}(kr) = J_0(kr) + iY_0(kr) \quad (B4)$$

where  $J_0$  and  $Y_0$  are Bessel functions of the first and second kind respectively.

Differentiating it one has,

$$\frac{\partial H_0^{(1)}(kr)}{\partial r} = -kJ_1(kr) - ikY_1(kr). \quad (B5)$$

Therefore, the derivative of Green's function is given by

$$\frac{\partial G}{\partial n} = \frac{i}{4} \left( -J_1(kr)k - iY_1(kr)k \right) \frac{\partial r}{\partial n} + \frac{i}{4} \left( J_1(k\bar{r})k + iY_1(k\bar{r})k \right) \frac{\partial r}{\partial n}$$

$$\begin{aligned}
 &= \frac{i}{4} \left( -J_1(kr) - iY_1(kr)k \right) \cos(\bar{n}, r) \\
 &+ \frac{i}{4} \left( J_1(k\bar{r})k + iY_1(k\bar{r})k \right) \cos(\bar{n}, \bar{r})
 \end{aligned} \tag{B6}$$

But, at the aperture,  $r_0 = \bar{r}$  and  $\cos(\bar{n}, r) = -\cos(\bar{n}, \bar{r})$  Therefore,

$$\frac{\partial G(x,0)}{\partial n} = -2\frac{i}{4} \left( J_1(kr) + iY_1(kr) \right) k \cos(\bar{n}, r) \tag{B7}$$

Making these substitutions in equation 4.30 one has,

$$U(x', z) = \frac{i}{2} \int_{x_1}^{x_2} U(x,0)k \left( J_1(kr) + iY_1(kr) \right) \cos(\bar{n}, r) dx \tag{B8}$$

Now, substituting  $\cos(\bar{n}, r) = z/r$  and  $U(x,0) = a + ib$  in the equation above one gets the following equation,

$$U(x', z) = \frac{zk}{2} \int_{x_1}^{x_2} \frac{-(J_1 b + aY_1)}{r} dx + i \int_{x_1}^{x_2} \frac{(J_1 a - bY_1)}{r} dx, \tag{B9}$$

which is equation 4.31. Here,  $z$  represents the perpendicular distance between the point  $(x, z)$  at which field is being calculated and the diffraction aperture. The real and imaginary parts of the field were determined by integrating the above equation using math library routine called 'd01gaf'. The computer program code is given in Appendix C.

```

c      program intrfcfld.f
c      This program calculates the electric field amplitude and
c      power reflection coefficient of a TE0 mode at the
c      waveguide-air interface of a surface-emitter.
c      The equations used in this program are from
c      the paper 'Output coupling ...', IEEE journal of Quantum
c      electronics, vol. QE-12, no. 5, May 1976, by Walpole & Davies.
c      The same program was used to calculate the field at the
c      waveguide-air interface for the case of surface-emitter with
c      parabolic turning mirror by just changing the parameters.

      double precision k0d,x0,beta0d,f1,f2,f3,f4,eps2,epsr2,gt2(900)
      double precision cotx0,pi,d,betab,beta,t,rtrp,f51,f52,n22
      double precision den1,epsrel,f7,k0n2,x,mod,rel,iml,y1,y2,gt11
      double precision w(800),x01aaf,abserr,h,lim1,lim2, re,im
      double precision reft,imft,ref0,imf0,gt1(900),reint,itrp,mod
      double precision imint,a(900),b(900),resum,imsun,rtrp,imq
      double precision r1,r2,r3,absr,ff,s1,epsrell,epsabs1
      double precision epsabs,n12,lim4,im3,im4,rep,req,pt1,pt2,imp
      double precision xp,xi,e0x,s1,betagama,kappa,et1,et2,y3,AA
      double precision rtrp1,itrp1,fldsum,ifldsum,refld(900),etx
      double precision imfld(900),emr,emi,mode,h1,y4,gama0
      double precision emr1,emil,dn1,amp,b0,lambda,mu0w,dif,modrefl
      double precision incdnt,refltd,radtn,imrefltd,imradtn,modrad
      integer ifail,inf,iw(102),kount,point,num,alpha
      external intr,intrl
      common/cl/ t,x0,k0d,x,kount,point,dif,alpha
      complex refl,bet,f6,ftl,den

c      All eqn. nos. refer to those used in the thesis.

c      mfield stores amplitude of electric field at the laser-air
c      interface.
      open(1,file="mfield")

c      file reintegral stores real part of the integral in eqn.
c      4.25
      open(9,file="reintegral")

c      reflty stores the calculated reflectivity
      open(3,file="reflty")

c      file imintegral stores imaginary part of the
c      integral in eqn. 4.25
      open(4,file="imintegral")

c      imfield stores imaginary part of the electric field at the
c      mirror vs (x/d)
      open(8,file="imfield")

c      rfield stores real part of the electric field at the
c      mirror vs (x/d)
      open(7,file="rfield")

c      file radfld stores the amplitude of radiation field given
c      by the integral in eqn. 4.24
      open(12,file="radfld")

c      file incfld stores the amplitude of the incident
c      guided wave given by the first term on the RHS of eqn. 4.24
      open(11,file="incfld")

c      file reflfld stores the amplitude of the reflected
c      guided wave given by the second term on the RHS of eqn. 4.24
      open(13,file="reflfld")

```

```

c      file reradfld stores the amplitude of real part of
c      radiation field given by the integral in eqn. 4.24
      open(14,file="reradfld")

c      file imradfld stores the amplitude of imaginary part of
c      radiation field given by the integral in eqn. 4.24
      open(15,file="imradfld")
      open(17,file="rnormfld")
      open(18,file="imnormfld")

c      pi=x01aaf(pi)
      refractive index square of core
      n12=13.0321d0

c      refractive index square of cladding
      n22=11.4244d0

c      half thickness of the active layer in microns
      d=0.03d0

c      lasing wavelength of diode laser in microns
      lambda=0.8

c      k0 is free space wave vector
      k0d=0.2356d0

c      mu0w is a constant
      mu0w=pi*dsqrt(480.0d0/lambda)

c      x0, as defined by eqn. A20 in appendix 1
      x0=0.2866d0

c      beta0d as defined by eqn.A4 in appendix 1
      beta0d=0.8008d0
      k0n2=k0d*dsqrt(n22)
c      step size for numerical integration over t using trapizoidal
c      rule for integral in eqn.4.24
      h=3.0d0/900.0d0
c      gama0 as in eqn.A5 in appendix 1
      gama0=2.815d0
      cotx0=1/dtan(x0)

c      evaluating F0 as given by eqn.4.27
      lim1=0.0
      lim2=k0d
      epsabs=0.0d0
      epsrel=1.0d-03
      eps2=0.0d0
      epsr2=1.0d-03
      inf=1
      ifail=0
      kount=1

c      this routine evaluates the real part of integral in eqn. 4.27
      call d01bdf(intr1,lim1,lim2,epsabs,epsrel,rel,absr)
      kount=2

c      this routine evaluates the imaginary of integral in eqn.
c      4.27
      call d01anf(intr1,lim2,inf,eps2,epsr2,iml
*      ,abserr,w,800,iw,102,ifail)
c      f7 calculates the term outside the integral in eqn.4.27
      f7=x0*(x0**4.)*((1.+dtan(x0)**2)**2)*4.0/(beta0d*(
*      x0+cotx0)*pi)

```

```

c      real part of F0.
      ref0=rel*f7
c      imaginary part of F0.
      imf0=iml*f7
c      b0 calculated from A4 in appendix 1
      b0=dsqrt((k0d**2)*n12-x0**2)/d
c      amp=denominator of amplitude in eqn.A1 appendix 1
      amp=dsqrt(1/(b0*(d+(1/gama0))))
c      dif represents "delta" in eqn.A2 in appendix 2
      dif=0.001d0
c      h1 is the step size for points at the interface
c      at which electric field is calculated
      h1=0.005d0
      i=1
      num=1
c      xp is distance along the facet or interface
      do 5 xp=-2,2,h1
          xi=abs(xp)
c      e0x as given by eqn.A1 in appendix 1
          if(xi.lt.d) then
              e0x=mu0w*amp*cos(x0/d*xp)
          else
              e0x=mu0w*amp*dcos(x0)*dexp(d*gama0)
              *dexp(-xi*gama0)
          endif
c      evaluating Ft as given by eqn.4.28
          do 10 t=0.0d0,3.0d0,h
              if(t.eq.0.0d0) then
                  a(i)=0
                  b(i)=0
                  etx=0
                  goto 45
              else
c      evaluating x using A20 in appendix 1
                  x=dsqrt(0.0893+(t**2))
                  al=(dcos(x)**2)+((x/t)**2)*(dsin(x)**2)
c      betagama from eqn.A8 in appendix 1
                  if(k0n2.gt.t) then
                      betagama=dsqrt(
                          (k0d**2)*n22-t**2)/d)
                  else
                      betagama=dsqrt
                          (t**2-(k0d**2)*n22)/d)
                  endif
c      AA =eqn.A6.2 in appendix 1
                  AA=(mu0w)*(1/(pi*betagama*al))**0.5
                  kappa=x/d
c      etx=eqn.A6.1 in appendix 1
                  if(xi.lt.d) then
                      etx=AA*dcos(x*xp/d)
                  else
                      et1=(dcos(x)*dcos(t)+(x*dsin(x)
                          *dsin(t)/t))*dcos(t*xp/d)
                      et2=(dcos(x)*dsin(t)-(x*dsin(x)
                          *dcos(t)/t))*dsin(t*xi/d)
                      etx=(et1+et2)*AA
                  endif
c      evaluating betab=beta**0.5 as given by eqn. 4.8 page 297
c      of the paper mentioned above
                  if(t.lt.k0n2) then
                      betab=dsqrt(dsqrt
                          ((k0d**2)*n22-t**2))
                  else
                      betab=dsqrt(dsqrt
                          (t**2-(k0d**2)*n22))
                  endif
          enddo
      enddo

```



```

c          imaginary part of 2nd integral          kount=2
                                                    inf=1
                                                    call d01bdf(intr,lim2,lim4,
*          epsabs,epsrel,iimp,absr)
*          call d01amf(intr,lim4,inf,
*          epsabs1,epsrel1,iimq,
*          abserr,w,800,iw,102,ifail)
                                                    pt2=iimp+iimq
                                                    re=rep-req
                                                    im=pt1-pt2
c          evaluating eqn. 4.26 for gt.          if(t.le.k0d) then
c          s1 evaluates square bracket in the denominator of 4.26
                                                    s1=dsqrt((k0d)**2-t**2)
                                                    den=cplx(s1,0.0)
c          f51 and f52 calculate the curly brackets in eqn. 4.28
                                                    f51=(4*t*(x**2-t**2)*re/pi)
*          +ff*s1
                                                    f52=4*t*(x**2-t**2)*im/pi
                                                    else
                                                    s1=-dsqrt(t**2-(k0d)**2)
                                                    den=cplx(0.0,s1)
                                                    f51=4*t*(x**2-t**2)*re/pi
                                                    f52=(4*t*(x**2-t**2)*im/pi)
*          +ff*s1
                                                    endif
c          real part of eqn. 4.28          reft=dsqrt(f1)*f51
c          imaginary part of eqn.4.28          imft=dsqrt(f1)*f52
                                                    beta=betab**2
                                                    if(t.lt.k0n2) then
                                                    bet=cplx(beta,0.0)
                                                    else
                                                    bet=cplx(0.0,-beta)
                                                    endif
                                                    ft1=cplx(reft,imft)
                                                    f6=-2*ft1/(bet+den)
c          gt1 is real part of eqn.4.26          den1=((1.0+ref0)**2)
*          +((imf0)**2)
*          gt1l=(real(f6)*(1+ref0)
*          +aimag(f6)*imf0)
                                                    gt1(i)=gt1l/den1
c          gt2 is the imaginary part of 4.26          gt2(i)=(aimag(f6)*(1+ref0)-
*          imf0*real(f6))/den1
c          real part of integral 4.25          reint=(reft*gt1(i)-imft*gt2(i)
*          )*((d**0.5)/betab)
c          imaginary part of integral 4.25          imint=(imft*gt1(i)+reft*gt2(i))
*          *((d**0.5)/betab)
                                                    a(i)=reint
                                                    b(i)=imint
                                                    write(9,100) t,a(i)
                                                    write(4,100) t,b(i)
                                                    format(1x,e10.4,2x,e10.4)
100          else
                                                    goto 50
                                                    endif
c          refld(i) stores the values of real part of integrand in eqn.4.24
50          refld(i)=(etx)*gt1(i)*betab/(d**0.5)
c          imfld(i) stores the values of imaginary part of integrand

```

```

c      in eqn.4.24
                                imfld(i)=(etx)*gt2(i)*betab/(d**0.5)
                                goto 55
                                endif
45      write(9,100) t,a(i)
                                write(4,100) t,b(i)
                                refl(i)=0.0d0
                                imfld(i)=0.0d0
55      i=i+1
10     continue
                                resum=0.0d0
                                imsum=0.0d0
                                fldsum=0.0d0
                                ifldsum=0.0d0
c      evaluating integral 4.25 and 4.24 using trapizoidal rule
                                rewind(9)
                                rewind(4)
                                read(9,100) (t,a(i),i=1,900)
                                read(4,100) (t,b(i),i=1,900)
                                y1=(a(1)+a(900))*h/2.0
                                y2=(b(1)+b(900))*h/2.0
                                y3=(refld(1)+refld(900))*h/2.0
                                y4=(imfld(1)+imfld(900))*h/2.0
                                do 20 i=2,899
                                    if(num.eq.1)then
                                        rtrp=a(i)*h
                                        itrp=b(i)*h
                                        resum=resum+rtrp
                                        imsum=imsum+itrp
                                    else
                                        goto 75
                                    endif
75      rtrpl=refld(i)*h
                                itrpl=imfld(i)*h
                                fldsum=fldsum+rtrpl
                                ifldsum=ifldsum+itrpl
20     continue
                                if(num.eq.1) then
                                    r1=1-ref0-(resum+y1)
                                    r2=-imf0-(imsum+y2)
                                    r3=1+ref0
c      reflectivity is calculated as given by eqn.4.25
                                refl=cmplx(r1,r2)/cmplx(r3,imf0)
                                print*,refl,'refl'
                                mod=(real(refl))**2+(aimag(refl))**2
                                write(3,*) mod,dif,'**'
                                else
                                    goto 90
                                endif
c      emr and emi are real and imaginary parts of eqn.4.24
90     incdnt=e0x
                                refltd=real(refl)*e0x
                                radtn=fldsum+y3
                                imrefltd=aimag(refl)*e0x
                                imradtn=ifldsum+y4
                                emr=incdnt+refltd+radtn
                                emi=imrefltd+imradtn
                                modrad=dsqrt(radtn**2+imradtn**2)
                                modrefl=dsqrt(refltd**2+imrefltd**2)
                                dn1=(1+real(refl))**2+(aimag(refl))**2
                                emr1=(emr*(1+real(refl))+emi*aimag(refl))/dn1
                                emi1=((1+real(refl))*emi-emr*aimag(refl))/dn1
                                mode=dsqrt(emi**2+emr**2)
                                write(1,100) xp,mode
                                write(7,100) xp,emr
                                write(8,100) xp,emi

```

```

write(11,100) xp,incdnt
write(12,100) xp,modrad
write(13,100) xp,modrefl
write(14,100) xp,radtn
write(15,100) xp,imradtn
write(17,100) xp,emr1
write(18,100) xp,emil
num=0
i=1
5   continue
end

double precision function intr(y)
*****
c   this function calculates the integrand in eqn.4.28

double precision intr,y,i1,i2,t,x0,x,k0d,t1
double precision i21,dif
integer kount,point,alpha
common/c1/ t,x0,k0d,x,kount,point,dif,alpha
if(kount.eq.1) then
    t1=dsqrt((k0d**2)-(y**2))
else
    t1=-dsqrt((y**2)-(k0d**2))
endif
if(y.ne.x0) then
    i1=t1*(y*dsin(y)*dcos(x0)-x0*
*   dsin(x0)*dcos(y))/(y**2-x0**2)
else
    i1=t1*0.5*(1+(dsin(x0)*dcos(x0)/x0))
endif
i21=(x0**2)
*   *(1+dtan(x0)**2)/(y**2+((x0**2
*   )*(dtan(x0)**2)))
if(y.ne.x) then
    i2=(y*dsin(y)*dcos(x)-x*dsin(x)*dcos(y))*i21
*   /(y**2-x**2)
else
    i2=0.5*(1+(dsin(x)*dcos(x)/x))*i21
endif
if(point.eq.1) then
    intr=i1*i2/(y+t)/(2*t)
else
    if(alpha.eq.0)then
        intr=(y-t)*i1*i2/((y-t)**2+(dif)**2)/(2*t)
    else
        intr=i1*i2/(y-t)/(2*t)
    endif
endif
return
end

double precision function intr1(y)
*****
c   This function calculates the integrand in eqn.4.26

double precision intr1,i11,i22,x0,x,k0d,y,t,t1
double precision dif
integer kount,point,alpha
common/c1/t,x0,k0d,x,kount,point,dif,alpha

if(kount.eq.1) then
    t1=dsqrt((k0d**2)-(y**2))
else

```

```
          t1=-dsqrt((y**2)-(k0d**2))
endif
i11=t1/((y**2+(x0**2)*(dtan(x0)**2))
**2)
*
if(y.ne.x0) then
*       i22=((y*dsin(y)*dcos(x0)-x0*dsin(x0)*dcos(y))
**2)/((y**2-x0**2)**2)
else
       i22=(0.5*(1+(dsin(x0)*dcos(x0)/x0))**2
endif
intr1=i11*i22
return
end
```

```
c      program 2dmirr.f
c      This program calculates the field at the 45 degree
c      straight turning mirror using equation A9, appendix 2,
c      A2.2 and the field at the facet calculated from the
c      program 'intrfcfld.f'.

      double precision x,z,xp,r,k,lambda,x0laaf,f1,f2,pi,p,q
      double precision a,b,j1,y1,t,h,h1,const,ans1,ans2,n1,n2
      double precision fil(800),fill(800),fil2(800),result

c      '2dfldmirr' stores the field amplitude at the turning mirror
      open(3,file="2dfldmirr")

c      '2drfldmirr' stores the real part of the field at the turning
c      mirror.
      open(4,file="2dfldrmirr")

c      '2dfldmirr' stores the imaginary part of the field at the
c      turning mirror
      open(7,file="2dfldimmirr")

      pi=x0laaf(pi)
c      free space wavelength
      lambda=0.8d0
      k=2.0*pi/lambda
c      step size for points on the turning mirror
      h1=6.5/250.0
c      step size for points at the facet
      h=0.005d0
      do 10 xp=-4.0,2.5,h1
          open(1,file="rfield1")
          open(2,file="imfield1")
c          equation of 45 degree straight mirror.
          z=xp+4.5
          i=1
c          'x' are coordinates of points on the facet at which
c          field values are known.
          do 20 x=-2.0,2.0,h
              r=dsqrt((x-xp)*(x-xp)+z*z)
              t=k*r
c              bessel function of first kind
              j1=dbesj1(t)
c              bessel function of the second kind
              y1=dbesy1(t)
              read(1,100) p,a
              read(2,100) q,b
c              f1 is the integrand in the first term
c              on the RHS of equation A9, Appendix 2, A2.2.
              f1=-(j1*b+a*y1)/r
c              f2 is the integrand in the second term
c              on the RHS of equationc A9, Appendix 2, A2.2.
              f2=(j1*a-b*y1)/r
              fil(i)=x
              fill(i)=f1
              fil2(i)=f2
              i=i+1
20          continue
          close(1)
          close(2)
          N=800
          ifail=0
c      Math library routine to calculate the field at the
```

```
c      turning mirror from values of f1, f2 and x.
c      calculates real part of field.
c      call d01gaf(fil,fil1,N,ans1,err,ifail)
c      calculates imaginary part of field.
c      call d01gaf(fil,fil2,N,ans2,err,ifail)
c      'z' is the perpendicular distance between point on the
c      mirror at which the field is being calculated,
c      and the facet.
c      const=z*k/(2.0)
c      result=dsqrt(ans1*ans1+ans2*ans2)*const
c      n1=ans1*const
c      n2=ans2*const
c      write(3,100) xp,result
c      write(4,100) xp,n1
c      write(7,100) xp,n2
100     format(1x,e10.4,2x,e10.4)
10     continue
      end
```

```

c      program 2daper.f
c      This program calculates the field at the aperture using
c      equation A9, appendix 2, A2.2 and field at the turning
c      mirror.

double precision zp,z,xp,r,k,lambda,x0laaf,f1,f2,pi,p,q,ai,dist
double precision a,b,j1,y1,t,h,h1,const,ans1,ans2,n1,n2,bi,err
double precision fil(250),fill(250),fil2(250),result,dist,l1,pnd

c      field amplitude at the aperture.
c      open(3,file="2dfldaper")
c      real part of the field at the aperture.
c      open(4,file="2dfldraper")
c      imaginary part of the field at the aperture.
c      open(7,file="2dfldimaper")

pi=x0laaf(pi)
c      free-space wavelength.
lambda=0.8d0
k=2.0*pi/lambda
c      step size for points on the turning mirror.
h=6.5/250.0
c      step size for points on the aperture.
hl=7.0/250.0
do 10 zp=-4.5,2.5,h1
c      real part of the field at the turning mirror.
c      open(1,file="2dfldrmirr")
c      imaginary part of the field at the turning mirror.
c      open(2,file="2dfldimmirr")
c      i=1
c      do 20 z=-4.0,2.5,h
c          r=dsqrt((((zp-2*z+2.5)**2)+((2.5-zp)**2))/2)
c          r=dsqrt((zp-z)*(zp-z)+(2.5-z)*(2.5-z))
c          t=k*r
c          bessel function of the first kind.
c          j1=dbesj1(t)
c          bessel function of the first kind.
c          y1=dbesy1(t)
c          read(1,100) p,ai
c          read(2,100) q,bi
c          0.65 is the reflectivity. Negative sign implies
c          phase change of 180 degrees on reflection
c          a=-0.65*ai
c          b=-0.65*bi
c      f1 and f2 as explained in the program 2dmirr.f.
c          f1=-(j1*b+a*y1)/r
c          f2=(j1*a-b*y1)/r
c          fil(i)=z
c          fill(i)=f1
c          fil2(i)=f2
c          i=i+1
20      continue
c      close(1)
c      close(2)
c      N=249
c      ifail=0
c      Math library routine to calculate real and imaginary
c      parts of the field at the aperture from f1,f2 and z.
c      call d0lgaf(fil,fill,N,ans1,err,ifail)
c      call d0lgaf(fil2,fill2,N,ans2,err,ifail)
c      distance along z axis from O' to the end of the
c      turning mirror in figure 4.11.
c      dist=2.5d0
c      perpendicular distance between a point 'zp' on the
c      aperture, at which field is being calculated

```

```
c          and the turning mirror.
          pnd=(dist-zp)/dsqrt(2.0d0)
          const=pnd*k/(2.0)
          result=dsqrt(ans1*ans1+ans2*ans2)*const
          n1=ans1*const
          n2=ans2*const
          write(3,100) zp,result
          write(4,100) zp,n1
          write(7,100) zp,n2
100       format(1x,e10.4,2x,e10.4)
10       continue
       end
```

```

c      Program 2dffld.f
c      This program calculates the farfield pattern using
c      equation A9 in appendix 2, A2.2 and the field at the
c      aperture AGB. The same program can calculate the field
c      due to the facet by changing names of relevant files.

double precision zp,zpp,r,k,lambdax01aaf,f1,f2,pi,p,q,err
double precision a,b,j1,y1,t,h,const,ans1,ans2,n1,n2,pnd,angle
double precision fil(250),fill(250),fil2(250),result,l
integer N

c      field intensity at the plane P.
c      open(3,file="2dffldap")
c      real part of farfield.
c      open(4,file="2drffldap")
c      imaginary part of farfield.
c      open(7,file="2dimffldap")

pi=x01aaf(pi)
c      free-space wavelength.
lambda=0.8d0
k=2.0*pi/lambda
c      step size for points at the aperture AGB.
h=7.0/250.0
c      distance of plane P from the aperture AGB.
l=6.0d03
c      coordinates of points on plane P.
zpp=-l
do 10 j=1,100
    zpp=zpp+l/50.0
c      angle measured with respect to x' axis in figure 4.11.
c      represents angle perpendicular to junction plane.
    angle=datan(zpp/l)*180/pi
c      real part of field at aperture.
    open(1,file="2dfldraper")
c      imaginary part of field at aperture.
    open(2,file="2dfldimaper")
    i=1
    do 20 zp=-4.5,2.5,h
        r=dsqrt((zpp-zp)*(zpp-zp)+(l)*(l))
        t=k*r
c      bessel function of first kind.
        j1=dbesj1(t)
c      bessel function of second kind.
        y1=dbesy1(t)
        read(1,100) p,a
        read(2,100) q,b
c      f1 and f2 have the same meaning as in '2daper.f'
        f1=-(j1*b+a*y1)/r
        f2=(j1*a-b*y1)/r
        fil(i)=zp
        fill(i)=f1
        fil2(i)=f2
        i=i+1
20    continue
    close(1)
    close(2)
    N=249
    ifail=0
c      Math library routine to calculate the real and
c      imaginary parts of the farfield pattern from
c      f1,f2 and zp.
    call d0lgaf(fil,fill,N,ans1,err,ifail)
    call d0lgaf(fil,fil2,N,ans2,err,ifail)
    const=l*k/(2.0)

```

```
intensity of the farfield pattern.  
result=(ans1*ans1+ans2*ans2)*const*const  
real part of farfield.  
n1=ans1*const  
imaginary part of farfield.  
n2=ans2*const  
write(3,100) angle,result  
write(4,100) angle,n1  
write(7,100) angle,n2  
format(1x,e10.4,2x,e10.4)  
continue  
end
```

```
c      program add.f
c      This program calculates the total farfield by adding
c      the contributions due to field at the facet and at the
c      aperture coherently.

      double precision a,b,q,p,c,d,m,n,x1,x2,x3,x01aaf,pi

c      real part of the farfield due to field at aperture AGB.
      open(1,file="2drffldap")
c      imaginary part of the farfield due to field at aperture AGB.
      open(2,file="2dimffldap")
c      real part of the farfield due to field at the facet.
      open(3,file="2drffldfct")
c      imaginary part of the farfield due to field at the facet.
      open(4,file="2dimffldfct")
c      total farfield intensity vs angle
      open(7,file="fldadd45")
      pi=x01aaf(pi)
      do 10 i=1,100
          if(i.ge.51) then
              read(1,100) a,b
              read(2,100) p,q
              read(3,100) c,d
              read(4,100) m,n
              x1=b+d
              x2=q+n
          else
              read(1,100) a,b
              read(2,100) p,q
              x1=b
              x2=q
          endif
          x3=(x1*x1+x2*x2)
          write(7,100) a,x3
          format(1x,e10.4,2x,e10.4)
100      continue
10      end
```

```
c      Program 2dmirrinp.f
c      program calculates the field at the parabolic turning
c      mirror using equation A9, Appendix 2, A2.2.

double precision x,z,xp,r,k,lambda,x0laaf,f1,f2,pi,p,q
double precision a,b,j1,y1,t,h,h1,const,ans1,ans2,n1,n2
double precision fil(800),fil1(800),fil2(800),result
double precision c0,c11,c2,c3,c4,zp

c      file stores field amplitude at the parabolic mirror.
open(3,file="2dmirrinpcur")

c      file stores real part of field amplitude
c      at the parabolic mirror.
open(4,file="2drmirrinpcur")

c      file stores imaginary part of field amplitude
c      at the parabolic mirror.
open(7,file="2dimirrinpcur")

pi=x0laaf(pi)
free space wavelength.
lambda=1.34d0
k=2.0*pi/lambda
c      step size for points on the turning mirror
h1=11.5/250.0
c      step size for points on the facet.
h=0.005d0
c      coefficients of the polynomial representing the
c      turning mirror.
c0=-3.171d0
c11=0.11307d0
c2=-0.041898d0
c3=0.021812d0
c4=-0.0012623d0
c      z coordinate of points on the turning mirror.
do 10 z=0.35,11.08,h1
c      file stores real part of field at the facet
open(1,file="rfieldinp")
c      file stores imaginary part of field at the facet
open(2,file="imfieldinp")
c      equation of the turning mirror.
xp=c0+c11*z+c2*(z**2)+c3*(z**3)+c4*(z**4)
i=1
do 20 x=-2.0,2.0,h
c      r as defined in figure 4.10
r=dsqrt((x-xp)*(x-xp)+z*z)
t=k*r
c      bessel function of the first kind
j1=dbesj1(t)
c      bessel function of the second kind
y1=dbesy1(t)
read(1,100) p,a
read(2,100) q,b
c      f1 is the integrand in the first term on the
c      RHS of eqn. A6, Appendix 2, A2.2.
f1=-(j1*b+a*y1)/r
c      f2 is the integrand in the second term on the
c      RHS of eqn. A6, Appendix 2, A2.2.
f2=(j1*a-b*y1)/r
fil(i)=x
fil1(i)=f1
fil2(i)=f2
i=i+1
20      continue
```

```
close(1)
close(2)
N=800
ifail=0
c      Math library routine to calculate the real part
c      of the field at the mirror from values of f1 and x
c      call d0lgaf(fil,fil1,N,ans1,err,ifail)
c      Math library routine to calculate the imaginary part
c      of the field at the mirror from values of f1 and x
c      call d0lgaf(fil,fil2,N,ans2,err,ifail)
const=z*k/(2.0)
c      result=dsqrt(ans1*ans1+ans2*ans2)*const
c      real part of field at mirror
n1=ans1*const
c      imaginary part of field at mirror
n2=ans2*const
write(3,100) z,result
write(4,100) z,n1
write(7,100) z,n2
100   format(1x,e10.4,2x,e10.4)
10    continue
end
```

```

c      program calculates the field at the aperture
c      using the Green's function.

double precision z,zp,xp,r,k,lambda,x01aaf,f1,f2,pi,p,q,pnd
double precision a,b,j1,y1,t,h,h1,const,ans1,ans2,n1,n2,err
double precision fil(230),fill(230),fil2(230),result
double precision c0,c11,c2,c3,c4,rez(8),imz(8),coeff(8),z2
double precision x02aaf,ht,ll,al,bl,theta,arg,tol,zn,xpn,zl
integer ifail,N,M

c      file stores field amplitude at the aperture AGB in fig. 4.10
open(3,file="2dapinpcurl")
c      file stores real part of field amplitude at aperture AGB
open(4,file="2drapinpcurl")
c      file stores imaginary part of field amplitude at aperture AGB
open(7,file="2dimapinpcurl")

pi=x01aaf(pi)
c      free space wavelength
lambda=1.34d0
k=2.0*pi/lambda
c      step size for points at the aperture AGB
h1=11.08/250.0
c      step size for points at the turning mirror
h=11.5/250.0
c      coefficients of equation of turning mirror.
c0=-3.171d0
c11=0.11307d0
c2=-0.041898d0
c3=0.021812d0
c4=-0.0012623d0
ht=3.67d0
tol=x02aaf(tol)
do 10 z1=0.0,11.08,h1
    z2=z1-7.0
c      Coefficients of 8th degree polynomial, the roots
c      of which are calculated by math routine c02aef.
    coeff(1)=-4.0*(c4**2)
    coeff(2)=-7.0*c3*c4
    coeff(3)=-3.0*(c3**2)-6.0*c2*c4
    coeff(4)=-5.0*c4*c11-5.0*c2*c3
    coeff(5)=4.0*c4*(ht-c0)-4.0*c3*c11-2.0*(c2**2)
    coeff(6)=-3.0*c2*c11+3.0*ht*c3-3.0*c3*c0
    coeff(7)=-1.0-2.0*c2*c0+2.0*ht*c2-(c11**2)
    coeff(8)=z1+ht*c11-c0*c11
    M=8
    ifail=0
    call c02aef(coeff,M,rez,imz,tol,ifail)
c      'zn' represents the point where the perpendicular
c      from a point at the aperture meets the turning mirror.
    if(imz(7).eq.0) then
        zn=rez(7)
    else
        zn=rez(5)
    endif
    xpn=c0+c11*zn+c2*(zn**2)+c3*(zn**3)+c4*(zn**4)
    arg=c11+2.0*c2*zn+3.0*c3*(zn**2)+4.0*c4*(zn**3)
    theta=datan(arg)*180/pi
c      perpendicular distance between the point on the
c      aperture at which field is being calculated and mirror.
    pnd=dsqrt((ht-xpn)*(ht-xpn)+(zn-z1)*(zn-z1))
    open(1,file="2drmirrinpcur")
    open(2,file="2dimirrinpcur")
    i=1
    do 20 zp=-6.466,4.068,h

```

```
z=zp+7.0
xp=c0+c11*z+c2*(z**2)+c3*(z**3)+c4*(z**4)
l1=(ht-xp)
r=dsqrt(l1*l1+(z1-z)*(z1-z))
t=k*r
j1=dbesj1(t)
y1=dbesy1(t)
read(1,100) p,ai
read(2,100) q,bi
c negative sign represents phase change of 180
c degrees on reflection.
a=-ai
b=-bi
c f1,f2 same as explained in '2dmirring.f'
f1=-(j1*b+a*y1)/r
f2=(j1*a-b*y1)/r
fil(i)=z
fill(i)=f1
fil2(i)=f2
i=i+1
20 continue
close(1)
close(2)
N=229
ifail=0
c math library routine to calculate the real part of
c field at aperture from values of f1 and z.
call d01gaf(fil,fill,N,ans1,err,ifail)
c math library routine to calculate the imaginary part of
c field at aperture from values of f1 and z.
call d01gaf(fil,fil2,N,ans2,err,ifail)
const=pnd*k/(2.0)
result=dsqrt(ans1*ans1+ans2*ans2)*const
c real part of fireld at aperture
n1=ans1*const
c imaginary part of fireld at aperture
n2=ans2*const
write(3,100) z2,result
write(4,100) z2,n1
write(7,100) z2,n2
100 format(1x,e10.4,2x,e10.4)
10 continue
end
```

```

c      program 2dffldinp.f
c      This program calculates the farfield pattern due to the
c      field at the aperture of the parabolic turning mirror.
c      The same program can be used to calculate the farfield
c      due to the field at the facet by changing the relevant
c      file names.

      double precision zpp,zp,r,k,lambda,x01aaf,f1,f2,pi,p,q,err
      double precision a,b,j1,y1,t,h1,const,ans1,ans2,n1,n2,l
      double precision fil(250),fill(250),fil2(250),result
      double precision angle,h,zp1

c      stores the amplitude of the farfield
      open(3,file="2dffldinpcur100")
c      stores the real part of the farfield
      open(4,file="2drffldinpcur100")
c      stores imaginary part of the farfield
      open(7,file="2dimffldinpcur100")

      pi=x01aaf(pi)
      lambda=1.34d0
      k=2.0*pi/lambda
c      step size of points at the aperture
      h1=11.08/250.0
c      distance of plane at which farfield is measured.
      l=6.0d03
      h=0.005d0
      zpp=-1
      do 10 j=1,200
         zpp=zpp+1/100.0
c         angle perpendicular to the plane of the junction.
         angle=datan(zpp/l)*180/pi
c         real part of the field at the aperture
         open(1,file="2drapinpcur1")
c         imaginary part of the field at the aperture
         open(2,file="2dimapinpcur1")
         i=1
         do 20 zp=-7.0,4.036,h1
            r=dsqrt((zpp-zp)*(zpp-zp)+(l)*(l))
            t=k*r
            j1=dbesj1(t)
            y1=dbesy1(t)
            read(1,100) p,a
            read(2,100) q,b
            f1=-(j1*b+a*y1)/(r*0.63)
            f2=(j1*a-b*y1)/(r*0.63)
            fil(i)=zp
            fill(i)=f1
            fil2(i)=f2
            i=i+1
20          continue
         close(1)
         close(2)
         N=249
         ifail=0
         call d01gaf(fil,fill,N,ans1,err,ifail)
         call d01gaf(fil,fil2,N,ans2,err,ifail)
         const=l*k/(2.0)
         result=(ans1*ans1+ans2*ans2)*const*const
         n1=ans1*const
         n2=ans2*const
         write(3,100) angle,result
         write(4,100) angle,n1
         write(7,100) angle,n2
100        format(1x,e10.4,2x,e10.4)

```

10      continue  
         end

## BIBLIOGRAPHICAL NOTE

The author was born in Maharashtra, India on August 31, 1964. She attended the Indian Institute of Technology in Bombay, India, and received the Bachelor of Technology in Engineering Physics in June 1986.

The author began her studies at the Oregon Graduate Center in September 1986 and completed the requirements for the degree of Master of Science in Electrical Engineering in August 1988.

The author has been married since 1987 to Girish Gaitonde.